Washington University in St. Louis

Washington University Open Scholarship

Arts & Sciences Electronic Theses and Dissertations

Arts & Sciences

Winter 12-15-2021

Influence of Focal Activity on Macroscale Brain Dynamics in Health and Disease

Zachary Pollack Rosenthal
Washington University in St. Louis

Follow this and additional works at: https://openscholarship.wustl.edu/art_sci_etds

Part of the Neurosciences Commons

Recommended Citation

Rosenthal, Zachary Pollack, "Influence of Focal Activity on Macroscale Brain Dynamics in Health and Disease" (2021). *Arts & Sciences Electronic Theses and Dissertations*. 2619.
https://openscholarship.wustl.edu/art_sci_etds/2619

This Dissertation is brought to you for free and open access by the Arts & Sciences at Washington University Open Scholarship. It has been accepted for inclusion in Arts & Sciences Electronic Theses and Dissertations by an authorized administrator of Washington University Open Scholarship. For more information, please contact digital@wumail.wustl.edu.

WASHINGTON UNIVERSITY IN ST. LOUIS

Division of Biology and Biomedical Sciences
Neurosciences

Dissertation Examination Committee:
Jin-Moo Lee, Chair
Adam Bauer
Joseph Culver
Nico Dosenbach
Marcus Raichle
Abraham Snyder

Influence of Focal Activity on Macroscale Brain Dynamics in Health and Disease

by
Zachary Pollack Rosenthal

A dissertation presented to
The Graduate School
of Washington University in
partial fulfillment of the
requirements for the degree
of Doctor of Philosophy

May 2022
St. Louis, Missouri

© 2022, Zachary Rosenthal

Table of Contents

List of Figures iii

Acknowledgments v

Abstract of the Dissertation vii

Chapter 1: Introduction and Perspective 1

- 1.1 Hierarchical brain network activity 1
- 1.2 Development of optical imaging in animal models 4
- 1.3 Investigating macroscale networks with optical imaging in mice 6
- 1.4 Summary of Findings 12

Chapter 2: Peripheral sensory stimulation elicits global slow waves by recruiting somatosensory cortex bilaterally 13

- 2.1 Abstract 13
- 2.2 Introduction 14
- 2.3 Results 15
- 2.4 Discussion 31
- 2.5 Materials and Methods 40

Chapter 3: Local perturbations of cortical excitability propagate differentially through large-scale functional networks 48

- 3.1 Abstract 48
- 3.2 Introduction 48
- 3.3 Results 50
- 3.4 Discussion 79
- 3.5 Materials and Methods 89

Chapter 4: Conclusions and Future Directions 106

References 111

List of Figures

Figure 1.1. Types of cross-sectional recordings of multi-scale brain dynamics……….15

Figure 2.1. Peripheral sensory stimulation elicits traveling waves with state-dependent, opposite trajectories…………………………………………………………..………30

Figure 2.S1. Space frequency SVD of spontaneous and evoked SWs. ……………..…33

Figure 2.2. Rhythmic stimulation shifts the dominant frequency of slow wave activity globally across the dorsal neocortex……………………………………………………..34

Figure 2.S2. 2 Hz power maps are consistent within individual mice…………………..35

Figure 2.3. Unilateral ablation of S1 reduces global coherence of sensory-evoked slow waves……………………………………………………………………………………..38

Figure 2.4. Unilateral ablation of S1 disrupts globally resonant evoked SWs in both hemispheres……………………………………………………………………………...41

Figure 2.S3. Control mice without stroke show no change in global 3 Hz power evoked by right paw sensory stimulation across equivalent time points…………………………42

Figure 2.S4. Spontaneous 1-1.5 Hz slow wave resonance is focally attenuated in the left hemisphere in the perilesional area..……………………….…………………………...43

Figure 3.1. Efficient and specific viral delivery of DREADDs to $\mathrm{S1_W}$ parvalbumin interneurons…………………….……………………………………………….………65

Figure 3.2. Activating $\mathrm{S1_W}$ PV-DREADDs induces local changes in activity and excitability…………………….………………………………………………….………68

Figure 3.S1. Power spectral density computed with the fast Fourier transform for oxy-Hb optical intrinsic signal and GCaMP fluorescence. ……………………….……………69

Figure 3.S2. Comparison of Fourier transform and wavelet methods for computing band-limited LFP power. ………………….…………………………………………………70

Figure 3.3. Locally disrupted $\mathrm{S1_W}$ E/I balance bidirectionally modulates spectral power locally and in remote sensorimotor areas……………………….……………………….73

Figure 3.S3. Changes in infraslow oxy-Hemoglobin dynamics during DREADD activation……………………….………………………………………….……………..74

Figure 3.S4. Representative time-series of GCaMP fluorescence (∆F') within the left $\mathrm{M1_W}$ ROI……………………….……………………………………………….………...75

Figure 3.S5. Correlation changes are specific to the whisker sensorimotor network….80

Figure 3.4. Propagation of local E/I imbalance disrupts patterns of cortical resting-state functional connectivity……..……………………………………………………………81

Figure 3.S6. ON-OFF FC changes for infraslow oxy-Hb optical intrinsic signal……..…82

Figure 3.S7. ON and OFF FC maps used to calculate ∆FC maps…………………….....83

Figure 3.S8. FC patterns change in response to local chemogenetic constructs……...84

Figure 3.5. ON-OFF Changes in $S1_w$ event-triggered average activity spread intrahemispherically to $M1_W$ but not to the contralateral hemisphere……………………88

Figure 3.S9. Dependence of delta band GCaMP FC changes on amplitude of $S1_W$ activity……………………..……………………………………………………….……………...89

Figure 3.6. PV-INs modulate $S1_W$ excitability to ascending contralateral sensory inputs, but not ipsilateral inputs……………………..……………………………………………..91

Acknowledgments

I am deeply grateful for all of the support I have received on my PhD journey. Thank you:

… to Jin-Moo, for nurturing my growth as a scientist, writer and critical thinker; for your unending enthusiasm and intellectual engagement; and for demonstrating that it is in fact possible to be a successful academic clinician, head a multi-armed translational research group, raise a happy family, and still find time for vacation.

… to my thesis committee members – Adam, Avi, Joe, Marc, and Nico – for your words of wisdom, thoughtful conversations about neuroscience, and confidence in me.

… to Andrew, for patiently teaching me most everything I know how to do in lab.

… to Leah, for showing me how to approach one's PhD with humor, resilience and poise.

… to Karen, Ping, Ryan, Eric, Asher and the rest of the Lee Lab, for your camaraderie, generosity with your expertise, and hands-on support.

… to Ryan Raut, for sharing your passion for solving the brain, and your insights on oscillations both slow and Swift.

… to my parents, Mark and Shoshannah, my brother, Seth, and my friends from all stages of life, for making me feel loved and supported so far from home.

… to Linus and Carl, for grounding me, and keeping my lap warm while I worked.

… to Bryan, for your unwavering positivity, companionship, and moral support as I learn how to fail upward as a scientist and human.

… to the AHA (20PRE34990003) and NIH (F31NS103275), for financial support.

Zach Rosenthal

Washington University in St. Louis

May 2022

ABSTRACT OF THE DISSERTATION

Influence of Focal Activity on Macroscale Brain Dynamics in Health and Disease

by

Zachary Pollack Rosenthal

Doctor of Philosophy in Biology and Biomedical Sciences

Neurosciences

Washington University in St. Louis, 2022

Professor Jin-Moo Lee, Chair

Macroscopic recordings of brain activity (e.g. fMRI, EEG) are a sensitive biomarker of the neural networks supporting neurocognitive function. However, it remains largely unclear what mechanisms mediate changes in macroscale networks after focal brain injuries like stroke, seizure, and TBI. Recently, optical neuroimaging in animal models has emerged as a powerful tool to begin addressing these questions. Using widefield imaging of cortical calcium dynamics in mice, this dissertation investigates the mechanisms by which focal disruptions in activity alter brain-wide functional dynamics. In two chapters, I demonstrate 1) that focal sensory stimulation elicits state-dependent, global slow waves propagating from primary somatosensory cortex (S1). Using a focal ischemic stroke model, I show that bilateral activation of somatosensory cortices is required for initiating global SWs, while spontaneous SWs are generated independent of S1. 2) That regional disruption of cortical excitability induces widespread changes across cortical networks, using chemogenetic manipulation of parvalbumin interneurons to model focal epileptiform activity in S1. We further show that local imbalances in

excitability propagate differentially through intra- and interhemispheric connections, and can induce plasticity in large-scale networks. These studies begin to define the mechanisms of macro-scale network disruption after focal injuries, adding to our understanding of how local cortical circuits modulate global brain networks.

Chapter 1: Introduction and Perspective

1.1 Hierarchical brain network activity

The brain is an exquisitely organized, densely connected network containing billions of diverse neurons and glia. This network is alive with electrochemical activity, spanning multiple scales of space and time. In the temporal domain, the brain generates electrical oscillations over a broad range of frequencies, from infraslow activity (<0.01 Hz) to fast gamma waves and action potentials (>100 Hz), which nest hierarchically and interact with each other across timescales (Buzsaki and Draguhn, 2004). In the spatial domain, these waves engage individual neurons as well as large ensembles of neurons distributed broadly across functional networks. By synchronizing and patterning electrical activity on local and global scales, the brain is able to temporally bind neuronal assemblies together, organize information transfer, and support higher computational function (Buzsaki and Draguhn, 2004). The central goal of modern systems neuroscience is thus to understand how information is encoded and processed within multi-scale brain network dynamics.

Ideally, one could fully characterize brain dynamics by recording the activity and connectivity of every neuron at once, however there are considerable technical obstacles to doing so (Kleinfeld et al., 2019). Instead, modern neuroscience has relied on recording spatial and temporal cross-sections of multi-scale brain activity. The available tools for extracting these cross-sections can be roughly grouped into three categories: micro-, meso-, and macroscopic recording (**Figure 1.1**), each with their own merits and shortcomings.

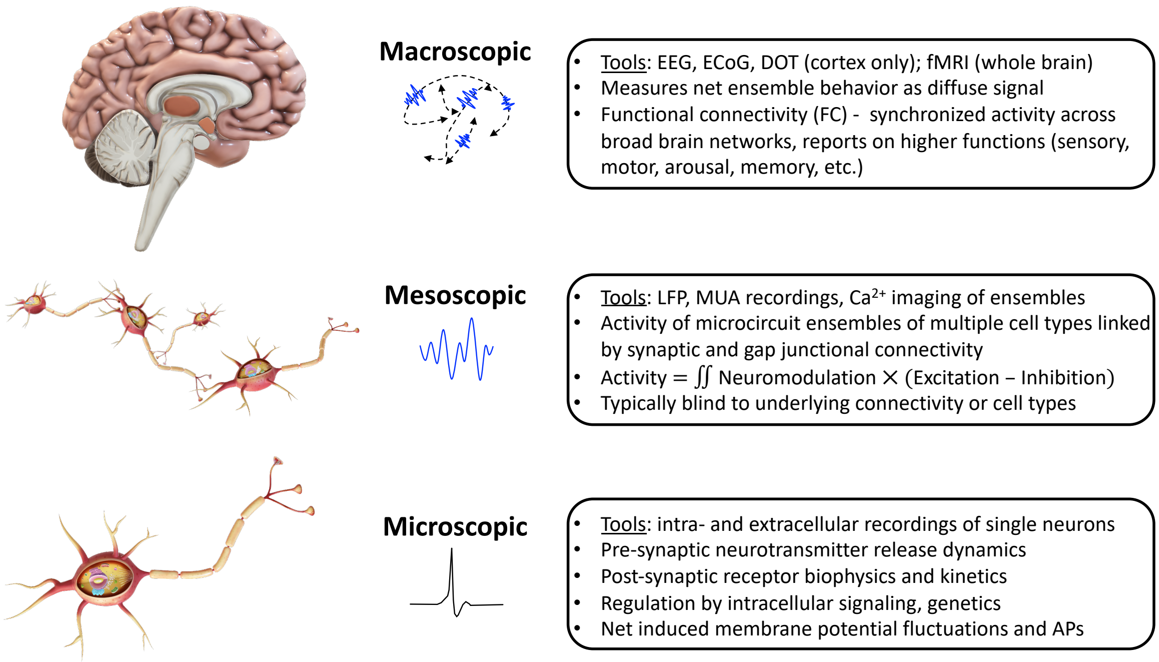
Macroscopic
Tools: EEG, ECoG, DOT (cortex only); fMRI (whole brain)
Measures net ensemble behavior as diffuse signal
Functional connectivity (FC) - synchronized activity across broad brain networks, reports on higher functions (sensory, motor, arousal, memory, etc.)
Mesoscopic
Tools: LFP, MUA recordings, Ca^{2+} imaging of ensembles
Activity of microcircuit ensembles of multiple cell types linked by synaptic and gap junctional connectivity
Activity = $\iint$ Neuromodulation × (Excitation – Inhibition)
Typically blind to underlying connectivity or cell types
Microscopic
Tools: intra- and extracellular recordings of single neurons
Pre-synaptic neurotransmitter release dynamics
Post-synaptic receptor biophysics and kinetics
Regulation by intracellular signaling, genetics
Net induced membrane potential fluctuations and APs

Figure 1.1 Types of cross-sectional recordings of multi-scale brain dynamics.

Microscopic recordings offer the most granular view of brain activity, primarily by using invasive electrophysiological probes to sample intra- and extracellular electrical potentials of individual neurons on kilohertz timescales. While future developments in probe design may permit massive sampling of individual neurons (Kleinfeld et al., 2019), this approach is inherently blind to the input and output connections of sampled neurons, as well as how those signals are integrated within each neuron’s complex subcellular electrical dynamics (Ranganathan et al., 2018, Moore et al., 2017). Meso-scale electrophysiology offers a broader perspective on the behavior of neuronal ensembles. For example, the local field potential (LFP) represents the weighted sum of the currents in nearby neurons and glia, and is an easy way to measure the net activity of local circuits with temporal precision on the millisecond timescale. Alternatively, probes can be designed to detect action potentials, using one or more electrodes to record nearby spiking of many neurons, or multi-unit activity (MUA). However, as with single cell recordings, it remains challenging to determine neuronal sources of meso-scale LFP and MUA signals, what type of neurons are activating, and perhaps most critically - with whom they are connected (Pesaran et al., 2018). There is thus great need to understand cellular and ensemble dynamics in the context of connected circuits and networks.

On the other end of spectrum, macroscale dynamics capture whole brain network dynamics and connectivity of broadly distributed neuronal ensembles. Macroscopic recordings in humans are typically non-invasive, and as we will discuss in subsequent sections, have untapped potential as a biomarker of the networks underlying neurocognitive function. However, our mechanistic insight into macroscale network behavior is limited by the available tools, as sampling large areas non-invasively comes at a cost of fine spatiotemporal resolution. For example, electroencephalography (EEG) can readily capture the net electrical activity at discrete points across the cortex, however cortical current signals are spatially diffuse, summative approximations of underlying cellular ensembles close to the brain’s surface. Functional magnetic resonance imaging (fMRI) imaging affords spatial access to activity across the whole brain, but at the cost of extremely limited temporal resolution, due to the inherently slow (<0.1 Hz) fluctuations of the blood oxygen level dependent (BOLD) signal. There is thus a need to understand the mechanisms that bridge the cellular and circuit-level activity surveyed by micro- and mesoscopic recordings with the macroscopic EEG and BOLD signals that can be recorded noninvasively in humans.

1.2 Development of optical imaging in animal models

In recent years, optical neuroimaging in animal models has emerged as a powerful tool to study the cellular and circuit underpinnings of macroscale network dynamics. In this section, I will briefly review the history of this technology and its advancement towards capturing higher fidelity cross-sections of macroscopic dynamics of the brain.

The earliest examples of optical neuroimaging measured the optical intrinsic signal (OIS), a label-free contrast based on differential light absorption by oxy- and deoxyhemoglobin. Visible light reflectance off of the brain over time thus reports on changes in cortical blood flow and oxygen consumption during neural activity, similar to the BOLD signal in fMRI, but with higher spatial resolution. This approach has been used to characterize the gross functional architecture of the cortex (Grinvald et al., 1986), the organization of V1 into orientation columns (Bonhoeffer and Grinvald, 1991), and the relationship between blood oxygen and neural activity (Devor et al., 2003). Optical imaging also offers faster temporal resolution than the BOLD fMRI signal, for example by taking advantage of techniques like multispectral illumination (Bouchard et al., 2009). However, like BOLD fMRI, OIS neuroimaging measures an indirect hemodynamic response to neural activity at infraslow (<0.1 Hz) speeds, and is thus blind to fast, underlying neural dynamics.

In the last two decades, new optical techniques have emerged to more directly report on fast neural dynamics. This was first accomplished using voltage sensitive dyes (VSDs) applied to the cortex to visualize electrical activity (Tsodyks et al., 1999). However, VSD preparations typically require craniotomies for dye delivery, and are thus largely restricted to single measurements in anesthetized animals. More recently, genetically encoded indicators have exploded in popularity (Lin and Schnitzer, 2016). These sensors improve upon VSDs because they can be targeted to subsets of neurons using specific promoter elements, and customized to report on different measures like voltage (Carandini et al., 2015, Akemann et al., 2012), neurotransmitter release (Marvin et al., 2013, Xie et al., 2016), and calcium dynamics (Chen et al., 2013, Dana et al., 2014). Critically, genetically encoded indicators are temporally stable, permitting longitudinal, non-invasive imaging in awake animals to examine physiologically relevant network dynamics.

Most optical imaging studies in the last decade have relied on the genetically encoded calcium indicator GCaMP, a fusion protein of circularly-permuted green fluorescent protein (GFP) and calmodulin (Chen et al., 2013). During action potentials, Ca^{2+} rapidly floods the cytoplasm, binding to GCaMP and inducing a conformational change that transiently restores GFP fluorescence until Ca^{2+} is cleared. GCaMP fluorescence has been shown to correlate with local electrophysiological recordings like MUA and LFP (Ma et al., 2016b, Murphy et al., 2018) and is thought to reflect supratheshold dynamics (Chen et al., 2013), and thus can act as a surrogate for electrophysiology over large spatial territories. GCaMP's popularity has been facilitated by its early availability in model organisms, for example using transgenic expression in mice (Chen et al., 2012, Dana et al., 2014), as well as delivery by viruses (Michelson et al., 2019). These models have pushed the boundaries of our mechanistic insight into macroscale network dynamics.

1.3 Investigating macroscale networks with optical imaging in mice

Macroscopic optical imaging in mice recapitulates many key features of human brain network dynamics observed with fMRI and EEG. In combination with the diverse palette of genetic manipulations, pharmacology, and injury models available in mice, optical imaging has proven a valuable experimental tool for dissecting the mechanisms underlying macroscale network dynamics in healthy and diseased brains. In this section, we will highlight some of the key translational discoveries mouse optical imaging has provided thus far.

Perhaps the most salient feature emerging from macroscopic brain recordings in humans is functional connectivity (FC) – synchronized activity across broadly distributed functional networks. FC manifests in correlated, spontaneous infraslow fluctuations in cortical electrophysiology (He et al., 2008) and BOLD signals (Fox and Raichle, 2007) within large neuroanatomical systems underlying vision, attention, memory, etc. Importantly, changes in infraslow FC patterns are sensitive to virtually every major neurological and psychiatric disease of the brain, and thus have unexplored potential as a diagnostic and prognostic tool (Fox and Greicius, 2010). In order to effectively translate macroscopic brain recordings into clinical care applications, the mechanistic basis of changes in FC must be further elucidated.

The first big step towards examining mechanisms of macroscale FC was demonstrating that OIS imaging in mouse models captures detailed resting state FC networks similar to those observed with human fMRI (White et al., 2011). Subsequently, it was shown that observed patterns in brain hemodynamics are coupled to underlying excitatory neural dynamics, using simultaneous OIS and GCaMP imaging (Ma et al., 2016b). Consistent with this finding, infraslow GCaMP dynamics exhibit similar FC patterns to those observed with hemodynamic signals, but unique FC patterns are further revealed on faster timescales detectable with calcium imaging (Vanni and Murphy, 2014, Wright et al., 2017b). While spontaneous activity was once thought to be “noise”, optical imaging has revealed that spontaneous dynamics engage the same connectivity framework as activity evoked by sensory stimulation, with spatial patterns mirroring monosynaptic structural connectivity (Mohajerani et al., 2013). Rather than being random, the correlation patterns observed as FC emerge from stereotyped spatial motifs unique to different frequency bands of activity (Vanni et al., 2017). While FC is typically examined at the macro level, optical imaging has further shown that long-distance synchronous connectivity is highly detailed even at the level of microcircuits like V1 orientation columns, demonstrated in anesthetized cats (O'Hashi et al., 2018) and both awake and anesthetized monkeys (Omer et al., 2019). Importantly, the spatial organization of FC has recently been shown to be regulated by electrical coupling of inhibitory interneurons (Kraft et al., 2020), suggesting that specific cell types may play a central role in shaping FC. The role of specific cellular and circuit actuators in shaping resting state FC remains understudied and critically important for understanding brain network physiology.

In addition to studying zero-lag connectivity measures like FC, mouse optical imaging has also been used to examine the lag structure of resting state networks. Human brain activity has been shown to consist of stereotyped sequences of spontaneous propagating activity (Mitra et al., 2015a, Raut et al., 2020). Lag analysis has revealed that propagation patterns reorganize between wake and sleep, such that communication between the cortex and subcortical structures reverses directions depending on state (Mitra et al., 2015b). Subsequent studies using electrocorticography and fMRI further showed that infraslow activity and faster delta band activity propagate in opposite directions (Mitra et al., 2016). These intriguing phenomena have recently been expanded upon using optical imaging and electrophysiology in mice. Using *Thy1-GCaMP6f* mice, it has now been shown that reciprocal propagation of delta and infraslow calcium waves occurs broadly across the cortex, that these trajectories likewise reverse depending on state, and that delta and infraslow activity travel through specific cortical layers (Mitra et al., 2018). Taken together, these findings suggest that the temporal organization of different frequencies of activity have distinct neurophysiologic and anatomic origins warranting further study.

Mouse optical imaging may also be combined with other experimental techniques to glean new insights about the anatomic origins of network connectivity. Combining OIS imaging with optogenetic stimulation of the cortex has revealed distinct patterns of effective connectivity elicited by focal cortical activation that correlate with local axonal projection connectivity (Bauer et al., 2018). In addition, optogenetics and optical imaging have been used to explore questions about neurovascular coupling to help interpret BOLD fMRI, for example by showing that hemodynamic responses driven by interhemispheric circuits vary depending on post-synaptic excitation/inhibition balance (Iordanova et al., 2018). Perturbational approaches like optogenetics are an especially valuable tool for revealing the structural basis of functional connectivity, by directly querying how activation of specific circuits affects broader networks (Snyder and Bauer, 2019). The role of specific circuits in macroscale networks may also be probed by combining recording techniques. For example, using simultaneous electrophysiology and optical imaging, it has been shown that motifs of correlated cortical activity are coupled to spiking in the thalamus (Xiao et al., 2017), suggesting that cortical FC may be driven in part by subcortical structures, consistent with subcortical stimulation experiments done in rodent fMRI (Chan et al., 2017, Wang et al., 2019).

Because genetically encoded sensors permit non-invasive imaging in awake animals, optical imaging has also become a powerful tool for understanding the relationship between behavior and macroscale network dynamics. This was first demonstrated using VSD imaging in awake mice to capture cortical sensorimotor dynamics during whisking behavior (Ferezou et al., 2007), which subsequently showed that cortical dynamics may vary during learned, goal-directed responses to whisker stimulation (Kyriakatos et al., 2017). Since then, optical imaging has been used to study more refined questions about distinct cortical dynamics during arousal, sensory detection, movement, and choice. For example, it has been shown that spontaneous, bilaterally synchronous cortical dynamics play a role in shaping response to stimuli, but not perceptual behavior, providing potential clues on the functional role of resting state FC (Shimaoka et al., 2019). More recently, using multiple imaging modalities and statistical modeling, it was revealed that uninstructed facial movements dominate global cortical networks during task behavior, suggesting that much of what is considered “noise” in macroscale dynamics may reflect subtle changes in movement behavior (Musall et al., 2019). These findings provide exciting context for large-scale electrophysiology studies showing that spontaneous activity in individual neurons across the brain are dominated by facial movement (Stringer et al., 2019), and that movement engages neurons non-selectively across the brain, while sensory response and choice are restricted to specific regions (Steinmetz et al., 2019). Much remains to be discovered about the functional purpose of encoding behavior on a global scale, and how distributed encoding manifests in broad network synchrony observed with macroscopic brain recording.

Lastly, optical imaging has facilitated exciting translational insights into brain network physiology during development as well as various disease states. OIS imaging has demonstrated that early visual experience during the visual critical period shapes FC in both visual systems and the cortex overall, via mechanisms dependent on Arc, a key regulator of synaptic plasticity (Kraft et al., 2017). Widefield imaging in transgenic GCaMP mice has further shown that neural activity in postnatal mice does not evoke functional hyperemia as in the adult brain, and that neural dynamics and hemodynamic responses evolve early in development as cortical connectivity is established (Kozberg et al., 2016). In combination with disease models, optical imaging has also proven valuable for interpreting connectivity changes observed in human patients with fMRI. For example, optical imaging in mice has led to key insights on network changes due to inflammatory white matter injury (Guevara et al., 2017), autism (Connor et al., 2016), peripheral nerve injury (Ashby et al., 2019), optic neuritis (Wright et al., 2017a), glioma (Orukari et al., 2020) and stroke (Bauer et al., 2014, Quattromani et al., 2018, Hakon et al., 2018, Kraft et al., 2018). One particularly robust mechanistic study demonstrated that mice with mutation of *Mdga2*, an autism related gene, exhibit elevated intrahemispheric FC with VSD imaging, in tandem with increased formation of excitatory synapses, elevated excitatory synaptic transmission, and autism-relevant behavioral phenotypes – effectively linking macroscale network hyperconnectivity with putative mechanistic underpinnings (Connor et al., 2016). In another study, mouse OIS imaging, histology, and behavioral assays were combined to demonstrate that plastic expansion of cortical territories after stroke (i.e. remapping, a phenomenon likewise observed in human stroke recovery) can be enhanced by sensory deprivation in neighboring cortical territories (Kraft et al., 2018). Furthermore, using genetically manipulated mice, this study revealed that sensory deprivation enhances remapping and local synapse formation via Arc-dependent mechanisms, and that this large-scale plasticity in cortical networks enhances behavioral recovery after ischemic injury (Kraft et al., 2018). Thus, disease models of network disruption and plasticity offer a valuable foundation for testing causal mechanisms between injury and disruptions in macroscale dynamics, as well as the ability of therapeutic interventions to restore healthy patterns of network connectivity.

1.4 Summary of Findings

This dissertation aims to bridge mechanisms of focal activity disruption with broader changes in macroscale networks. I take advantage of optical imaging of excitatory neuronal calcium fluctuations in mice to study how local sensorimotor dynamics and global brain activity are affected by focal activity disruption using two injury models: stroke (Chapter 2), and seizure (Chapter 3). In Chapter 2, I demonstrate that global slow waves evoked by sensory stimulation depend on bilateral interaction of somatosensory cortices, and that focal ischemic stroke in S1 can disrupt global slow wave dynamics elicited in either hemisphere. In Chapter 3, I show that focal, chemogenetically-induced imbalance in excitability in S1 propagates through specific functional connections to generate widespread disruptions in global networks. This work helps to lay the foundation for understanding global network dysfunction observed in human fMRI and EEG, and suggests that local changes in activity may be an important therapeutic target for restoring multiscale brain dynamics.

Chapter 2: Peripheral sensory stimulation elicits global slow waves by recruiting somatosensory cortex bilaterally

2.1 Abstract

Slow waves (SWs) are globally propagating low-frequency (0.5 - 4 Hz) oscillations that are prominent during sleep and anesthesia. SWs are essential to neural plasticity and memory. However, much remains unknown about the mechanisms coordinating SW propagation at the macroscale, in particular, the relative contributions of specific cortical and subcortical structures. Here, we test the hypothesis that global SWs evoked by peripheral sensory stimulation require bilateral interaction between primary somatosensory cortices (S1). We monitored cortical dynamics in awake and ketamine/xylazine anesthetized mice using widefield optical imaging with fluorescent calcium indicator GCaMP6f. We observed that somatosensory stimulation elicits broad traveling waves across the cortex with state-dependent trajectories. Under anesthesia, rhythmic stimuli elicit resonant SW activity originating in S1 that spreads globally across the cortex. Furthermore, unilateral sensory stimulation in mice with photoablative lesions of S1 revealed that both hemispheres participate in evoking global SWs. In contrast, spontaneous global SWs are robust to S1 ablation. Thus, specific cortical modules and their interhemispheric connections are required for SW initiation in response to peripheral stimulation. These results demonstrate the existence of mechanisms by which focal injury may disrupt macroscale brain dynamics.

2.2 Introduction

Slow waves (SWs) are the predominant cortical rhythm during non-rapid eye movement (NREM) sleep and anesthesia (Steriade et al., 1993b, Destexhe et al., 1999). Since they were first characterized three decades ago, SWs have been linked to a variety of brain functions, including memory consolidation (Marshall et al., 2006, Hoffman et al., 2007, Ngo et al., 2013, Binder et al., 2014), homeostatic synaptic plasticity (Tononi and Cirelli, 2014), and grouping of higher frequency events (Staresina et al., 2015, Neske, 2015, Oyanedel et al., 2020). Macroscopic tools such as EEG have revealed the large-scale structure of global SWs, which propagate with stereotypical front-to-back topography through the entire cortex approximately once per second (~1 Hz) (Massimini et al., 2004). Local electrophysiology has demonstrated that virtually every cortical neuron participates in this traveling wave, exhibiting phase-locked oscillations between depolarization (up-state) and hyperpolarization (down-state) (Volgushev et al., 2006, Luczak et al., 2007). During low arousal states, these global SWs occur spontaneously, though they can also be evoked by peripheral sensory stimulation, as well as direct electromagnetic and optogenetic stimulation of the cortex (Massimini et al., 2007, Riedner et al., 2011, Stroh et al., 2013, Mohajerani et al., 2013, Greenberg et al., 2018). However, much remains unknown about the large-scale circuit interactions required for SW generation and propagation.

Here, we investigate the role of primary somatosensory cortex and its interhemispheric connectivity in the initiation and global propagation of somatosensory-evoked SWs. To this end, we performed widefield optical imaging of cortical dynamics in awake and anesthetized mice expressing fluorescent calcium indicator GCaMP6f in pyramidal neurons. This mesoscopic view affords significant advantages over conventional approaches for recording SWs (EEG or local electrophysiology). In particular, high spatial resolution optical imaging across the whole dorsal neocortex allows for a more precise characterization of globally coherent waves of neural activity. We demonstrate that rhythmic sensory stimulation elicits broad waves with distinct, state-dependent trajectories of propagation. Further, we show that the imposed rhythm of stimulation induces resonant activity focally in sensorimotor areas in awake animals, and globally across the cortex in anesthetized animals. Finally, we use a photothrombotic stroke model to show that peripherally-evoked global slow waves depend on both ipsilateral and contralateral S1. Unilateral ablation of S1 disrupts global SWs evoked by peripheral stimulation of either hemisphere, but spares spontaneous SWs outside of the perilesional area. These findings point to a necessary role for primary somatosensory cortices and their homotopic connectivity in coordinating stimulation-evoked global SWs, and suggest potential mechanisms by which focal cortical injuries may influence global brain dynamics.

2.3 Results

Peripheral sensory stimulation elicits traveling waves with state-dependent, opposite trajectories

Plexiglass cranial windows were installed in *n*=10 *Thy1-GCaMP6f* mice to permit widefield optical imaging of cortical calcium dynamics through the intact skull, as previously described (Wright et al., 2017b). Imaging was performed during 5 minutes of right whisker stimulation (**Figure 2.1A**), using computer triggered air puffs in 10-second blocks (5s of puffs at 2 Hz, followed by 5s of rest). Mice were then anesthetized with ketamine/xylazine and the same stimulation protocol was repeated. Evoked responses were block-averaged for awake (*n*=10 mice, 600 blocks) and anesthetized (*n*=9 mice, 540 blocks) conditions (**Supplement Video 1**). **Figure 2.1B** shows the group-averaged response to a single puff in each condition.

In awake animals, right whisker stimulation elicits activity focally in left S1 whisker barrel cortex ($S1_W$), followed by a traveling wave spreading rostrally from $S1_W$ up to whisker motor cortex, consistent with prior reports employing voltage sensitive dye imaging in awake mice in a single hemisphere (Ferezou et al., 2007, Mohajerani et al., 2013). By expanding the field of view to include both hemispheres, we further demonstrate that this broad rostral wave is mirrored in the contralateral sensorimotor cortex in awake animals (**Figure 2.1B**). Under ketamine/xylazine anesthesia, whisker stimulation elicits a similar sensorimotor activation, which is quickly subsumed by a global slow wave propagating caudally from motor cortex to visual cortex. Block-average time series reveal that activity reverberates for several seconds after stimulation ceases in anesthetized, but not awake animals (**Figure 2.1C, Supplement Video 1**). This suggests that spontaneous global slow waves are consistently phase-reset by preceding stimulation.

We next characterized the spatiotemporal structure of cortical activity by examining dominant patterns of global coherence. We applied spatial singular value decomposition (SVD) to the frequency domain representation (i.e., space-frequency SVD (Prechtl et al., 1997)) of the group-averaged responses, yielding a set of orthogonal spatial modes containing global magnitude and phase information at each frequency (see Methods). Consistent with the patterns observed in **Figure 2.1B**, opposing wave trajectories in wake and anesthesia are evident from the phase maps of the dominant spatial mode at 2 Hz in each condition (**Figure 2.1D**). Notably, the state-dependent, reciprocal directionality of stimulus-evoked waves mirrors what we have previously reported in spontaneous activity during wake and anesthesia (Mitra et al., 2018).

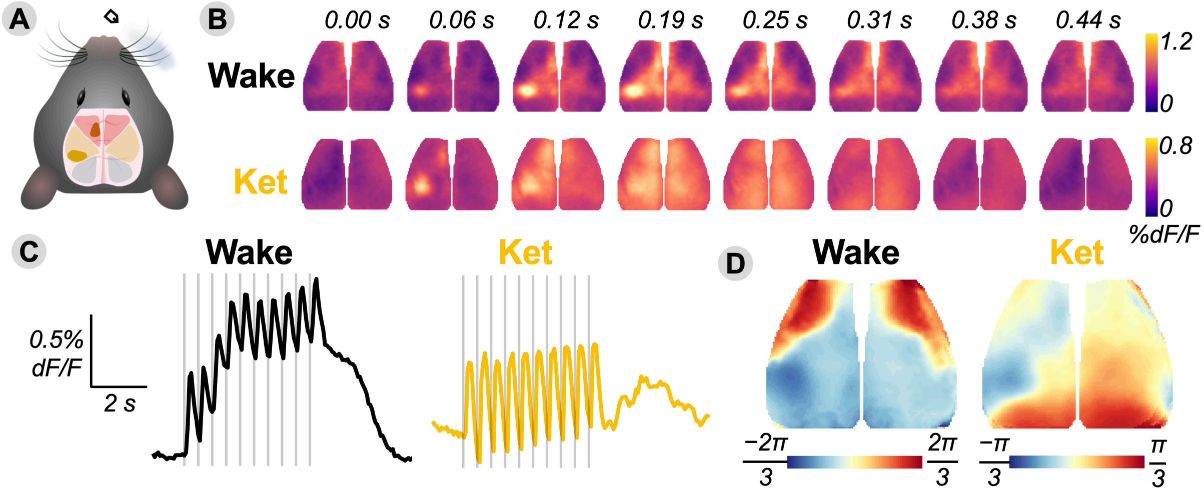

Figure 2.1. Peripheral sensory stimulation elicits traveling waves with state-dependent, opposite trajectories. (**A**) Diagram of cortical field of view spanning frontal/motor (red) somatosensory (yellow) and visual (blue). Right whisker stimulation elicits activity in left whisker barrel cortex ($S1_W$, solid yellow) and left motor cortex ($M1_W$, solid red). (**B**) Still frames depicting group-average response to a single right whisker deflection during wake (*n*=10 mice, 600 blocks) and ketamine/xylazine anesthesia (*n*=9 mice, 540 blocks). Frames come from corresponding Supplemental Video 1. (**C**) Group-average

time series of global GCaMP activity. Vertical lines indicate individual puff stimuli. (**D**) Phase maps of the dominant spatial mode of 2 Hz coherence, derived from space-frequency singular value decomposition of group-average blocks. Early portions of global waves exhibit negative phase values, late portions exhibit positive values (units are in radians).

Rhythmic stimulation shifts the resonant frequency of slow wave activity globally across the dorsal neocortex

The emergence of broadly propagating, stimulation-evoked SWs suggests that rhythmic sensory input may induce resonant activity globally across the cortex under anesthesia. To investigate this further, we asked whether stimulation shifts the dominant frequency of cortical activity, and to what extent stimulation-evoked activity is globally coherent.

We first examined spectral power in whole runs of alternating 5s blocks of with stimulation ON or OFF, to capture both spontaneous and evoked activity. As in local field potential recordings (Pesaran et al., 2018), spontaneous resting state GCaMP dynamics exhibit a 1/f power spectrum. Under ketamine anesthesia, a prominent spectral peak emerges at 1-1.5 Hz that corresponds to spontaneous front-to-back SWs (Wright et al., 2017b, Mitra et al., 2018). Here, we likewise observe that spontaneous global SWs occur under anesthesia with front-to-back topography during interstimulus OFF periods (see ketamine phase maps in **Figure 2.S1A)**. Importantly, by stimulating at a frequency faster than the endogenous SW frequency, we are able to dissociate unique properties of spontaneous SWs originating in frontal cortex (1-1.5 Hz, **2.S1A**) from evoked SWs originating in S1 (2 Hz, **2.1C/2.S1B**). In order to determine whether the dominant frequency of global SW activity changes during ON periods of rhythmic stimulation, we computed the global average brain signal within each mouse and generated power spectrograms using a short time Fourier transform (STFT). We observed that under ketamine/xylazine anesthesia, global dynamics alternate between primarily 1-1.5 Hz oscillations during 5s stim-OFF periods (corresponding to spontaneous SWs) and 2 Hz oscillations during 5s stim-ON periods (corresponding to the imposed stimulation rhythm) (**Figure 2.2A)**. Averaging STFT spectra across ON and OFF blocks in anesthetized animals, we observed a significant ON-OFF increase in global power specifically at 2 Hz (adjusted $^{**}P = 0.0017$, **Figure 2.2B**). Power of spontaneous 1-1.5 Hz SWs also appeared to decrease, although this change was not statistically significant ($^{NS}P = 0.59$). Thus, the dominant frequency of SW resonance shifts from 1-1.5 Hz to 2 Hz during rhythmic stimulation. In contrast, in the awake state where SWs are absent, 2 Hz global power resonates more weakly across the whole run (**Figure 2.2A**) and in block-average spectra (**Figure 2.2B**, $^{*}P = 0.035$).

Next, we examined whether stimulation-evoked resonance spreads more globally under anesthesia. First, we computed pixelwise power spectra over a block-average time series and observed that, under anesthesia, the evoked 2 Hz power is indeed globally distributed across the whole cortex (**Figure 2.2C**), while in awake animals, 2 Hz power is largely restricted to whisker barrel cortex and motor cortex. Similarly, the magnitude topography of the dominant spatial mode derived from space-frequency SVD shows more global effects under anesthesia (**Figure 2.S1B**). The state-specific spatial spread of evoked 2 Hz power is highly consistent across individual mice (**Figure 2.S2A,B**). To quantify this phenomenon further, we calculated global coherence of evoked (2 Hz) and spontaneous (1-1.5 Hz) SWs as the fractional power of the leading spatial mode obtained from space-frequency SVD (Mitra and Pesaran, 1999b, Prechtl et al., 1997). Indeed, global coherence of evoked 2 Hz waves is significantly greater under ketamine anesthesia than during wake ($^{**}P = 0.0028$, **Figure 2.2D**). As expected with the emergence of spontaneous global SWs, 1-1.5 Hz activity is more broadly distributed (**Figure 2.S1A)** and more globally coherent under ketamine anesthesia than in the awake state ($^{***}P = 0.0005$).

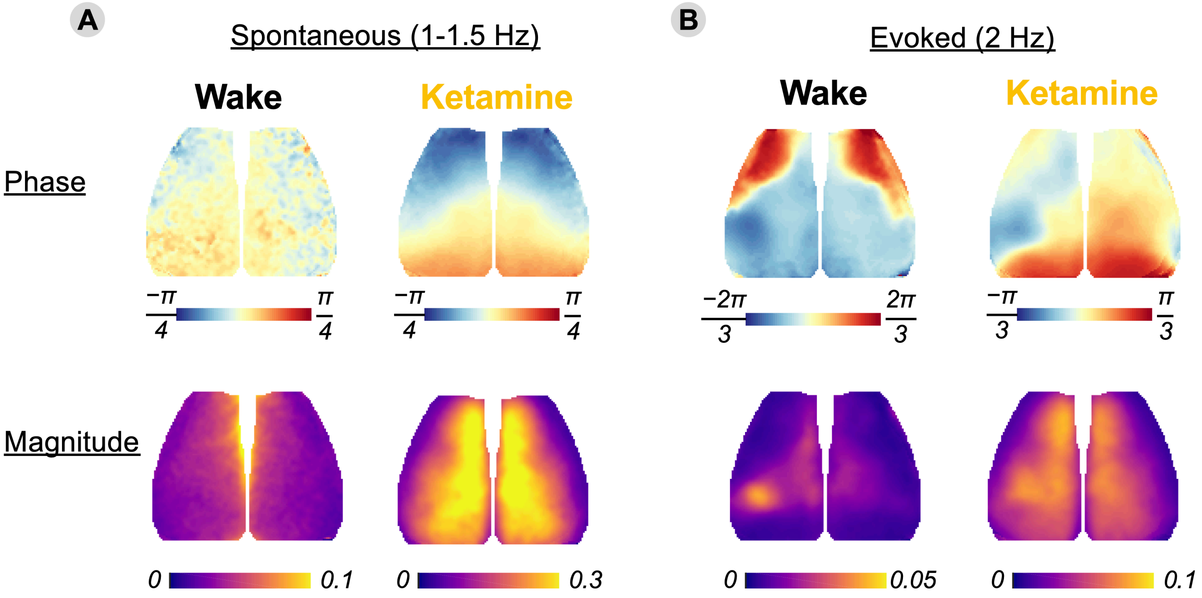
A
Spontaneous (1-1.5 Hz)
B
Evoked (2 Hz)
Wake
Ketamine
Wake
Ketamine
Phase
−π/4
π/4
−π/4
π/4
−2π/3
2π/3
−π/3
π/3
Magnitude
0
0.1
0
0.3
0
0.05
0
0.1

Figure 2.S1. Space frequency SVD of spontaneous and evoked SWs. (**A,B**) Phase (in radians) and magnitude (arbitrary units) of the dominant spatial mode of 1-1.5 Hz spontaneous (**A**) and evoked (**B**) activity averaged across mice under wake and ketamine anesthetized states.

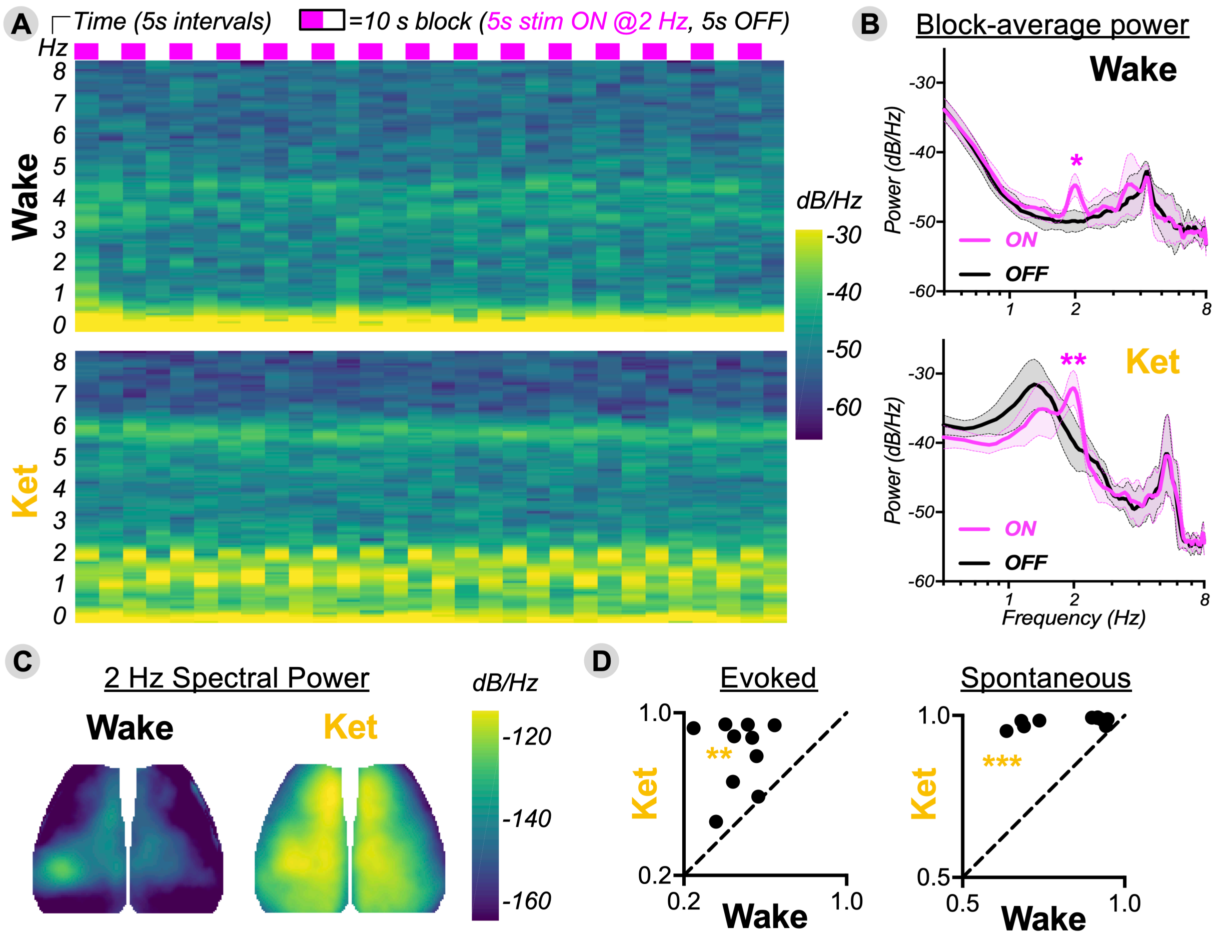

Figure 2.2. Rhythmic stimulation shifts the dominant frequency of slow wave activity globally across the dorsal neocortex. (**A**) Group-average spectrograms of global GCaMP power (0-8 Hz, y-axis) over the course of consecutive 10-second blocks consisting of 5s stim ON and 5s stim OFF (time in 5-second bins, x-axis). (**B**) Average power spectra for all stim-ON (magenta) and stim-OFF (black) periods. Differences are statistically tested by two-way ANOVA with Sidak's multiple comparison test. Note, spectral peaks at ~4 Hz (wake) and ~5.5 Hz (ketamine) correspond to heartrate. Spectra are not normalized by total power. (**C**) Cortical maps depicting spatial distribution of 2 Hz power, computed from the group-average block. See Supplemental Figure 2.S2A,B for 2 Hz power maps within individual mice. (**D**) Global coherence of evoked (2 Hz) and spontaneous (1-1.5 Hz) activity, comparing wake versus ketamine. Global coherence is calculated within individual mice as the fractional power of the leading spatial mode obtained from space-frequency SVD (Mitra and Pesaran, 1999b, Prechtl et al., 1997). Statistical significance determined by paired t-test.

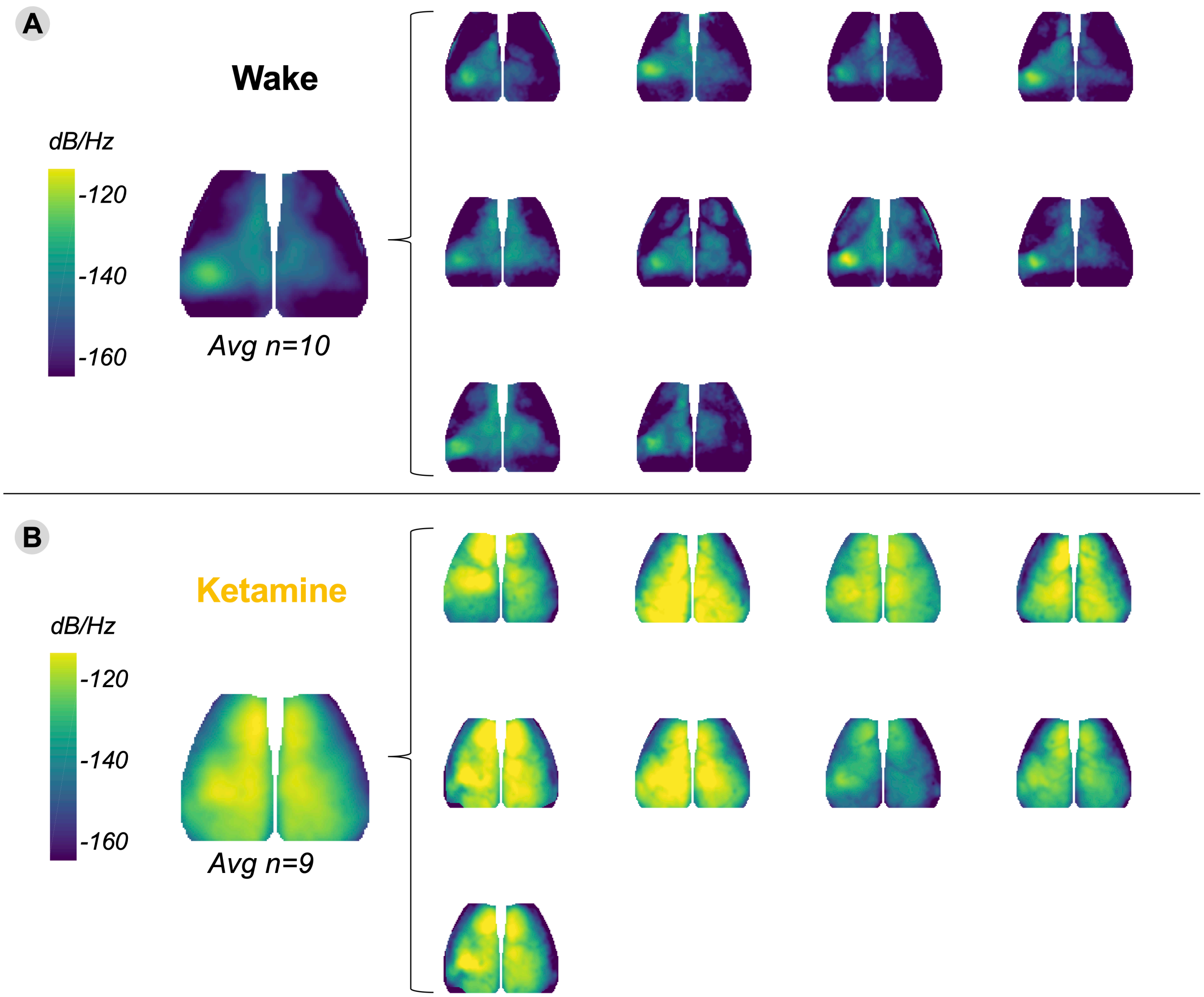
A
Wake
dB/Hz
-120
-140
-160
Avg n=10
B
Ketamine
dB/Hz
-120
-140
-160
Avg n=9

Figure 2.S2. 2 Hz power maps are consistent within individual mice for wake (**A**) and ketamine (**B**). See average of individuals in Figure 2.2C.

Unilateral ablation of S1 reduces the global coherence of sensory-evoked slow waves

Having demonstrated that sensory stimulation elicits globally resonant SWs originating from S1, we next sought to assess the necessity of S1 for initiating these waves. To this end, we analyzed a previously collected dataset in which responses to 3 Hz forepaw stimulation under ketamine/xylazine anesthesia were examined before (“pre”) and one week following (“post”) unilateral laser photoablation of forepaw sensory cortex ($S1_{FP}$) (Rosenthal, 2017). These infarcts have well-circumscribed margins and are confined within left hemisphere $S1_{FP}$ cortex (**Figure 2.3A**), with an estimated volume of 1.94±0.33 mm^3. Imaging was performed during 5 minutes of stimulation of right or left forepaw under anesthesia, using mild cutaneous electrical shock in 20 second blocks (5s of shocks at 3 Hz, followed by 15s of rest). Data represent an average of *n*=12 mice, 180 blocks total per paw at each timepoint.

At baseline, 3 Hz electrical stimulation of right or left forepaw elicits contralateral $S1_{FP}$ and motor activation followed by a global front-to-back SW (**Figure 2.3B, Supplemental Videos 2 and 3**), similar to responses following whisker stimulation (**Figure 2.1**). One week after left $S1_{FP}$ stroke, right forepaw stimulation on average evokes a weaker left $S1_{FP}$ response due to local tissue death (visible as a dark circular void in **Figure 2.3B**). Evoked activity is also dramatically attenuated outside of the infarct, including weaker secondary activation of ipsilateral motor cortex and contralateral sensorimotor cortex, and reduced amplitude of the ensuing global front-to-back SW.

Stimulating the left forepaw after stroke still elicits a strong response in right $S1_{FP}$ and motor cortex in the contralesional hemisphere; however, surprisingly, the subsequent global SW component is again weakened (**Figure 2.3B**). While the dominant spatial modes exhibit similar propagation patterns pre- and post-stroke (**Figure 2.3C,D**), global coherence of evoked SWs was significantly reduced after stroke for both ipsilesional (right paw $^{*}P = 0.03$, **Figure 2.3E**) and contralesional (left paw $^{*}P = 0.02$, **Figure 2.3F**) stimulation. Importantly, these changes are specific to sensory-evoked SWs – in contrast, global coherence of spontaneous SWs was strong and not significantly altered from pre-stroke baseline during OFF periods of right paw ($^{NS}P = 0.15$, **Figure 2.3E**) and left paw ($^{NS}P = 0.85$, **Figure 2.3F**) stimulation runs. Thus, unilateral ablation of S1 reduces global coherence of sensory-evoked SWs, but not spontaneous SWs.

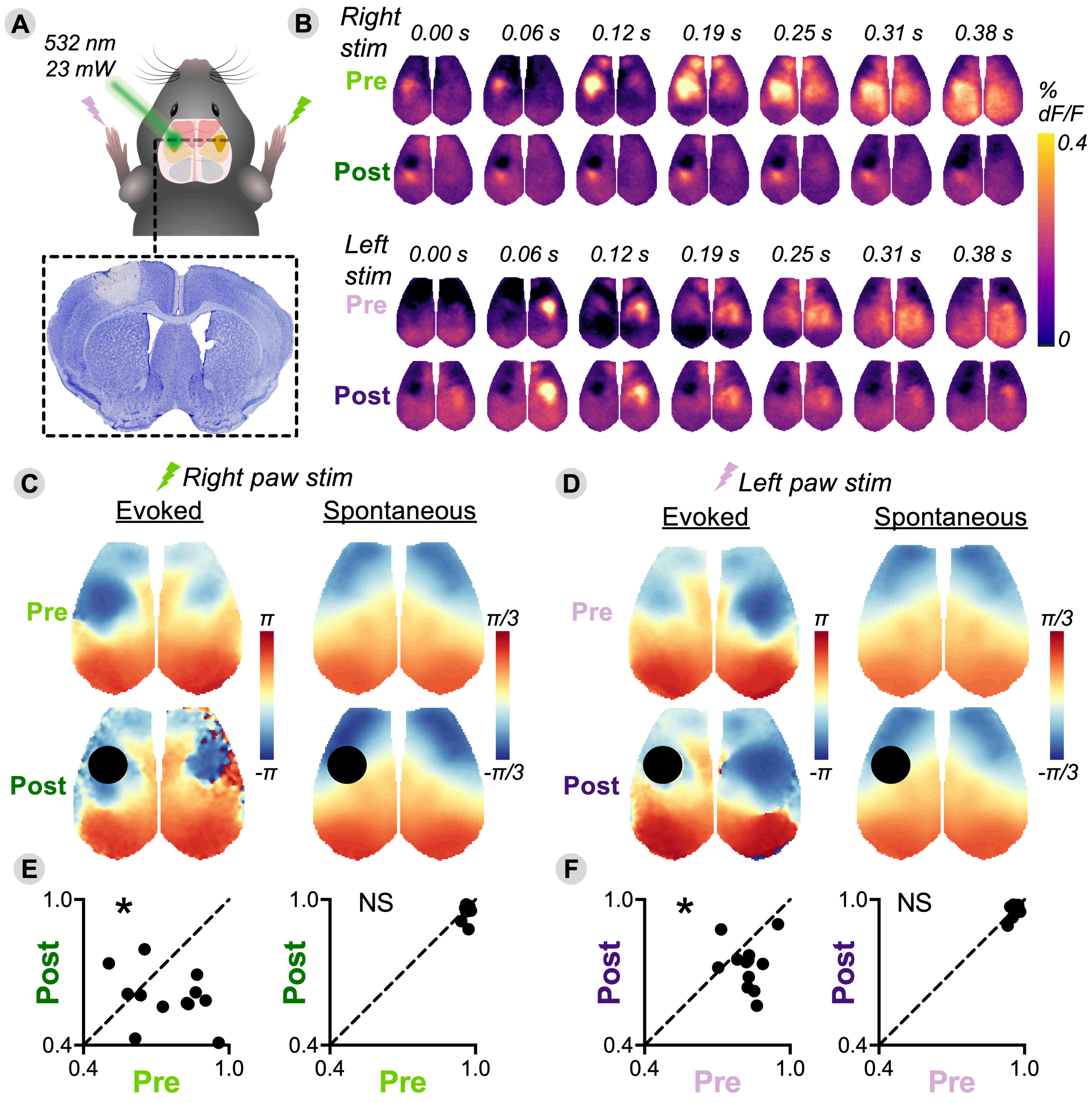

Figure 2.3. Unilateral ablation of S1 reduces global coherence of sensory-evoked slow waves. (**A**) Diagram depicting photothrombosis of left forepaw somatosensory cortex ($S1_{FP}$, plotted bilaterally in solid yellow) along with a Nissl-stained cross-section through the middle of the infarct used to calculate infarct volume. Cell death is isolated within $S1_{FP}$ cortex. (**B**) Still frames depicting group-average response to right paw stimulation pre- (light green) and post-stroke (dark green), as well as left paw stimulation pre- (pale purple) and post-stroke (dark purple). Data represent an average of *n*=12 mice, 180 blocks total per paw at each timepoint. Frames come from corresponding Supplemental Videos 2 (right paw stimulation) and 3 (left paw stimulation). (C-D) Dominant spatial mode phase maps of evoked (3 Hz) and spontaneous (1-1.5 Hz) slow waves derived

from space-frequency SVD of group-average blocks of right paw stimulation (**C**) and left paw stimulation (**D**). Early portions of global waves exhibit negative phase values, late portions exhibit positive values (units are in radians). (**E-F**) Global coherence of evoked and spontaneous SWs during runs of right (**E**) or left (**F**) paw stimulation, comparing pre- and post-stroke within individual mice with a paired t-test. Quantification of global coherence excluded the infarct (masked in black) so as to capture changes in surviving cortex.

Unilateral ablation of S1 disrupts globally resonant evoked SWs in both hemispheres

Next, we tested whether the spatial distribution of SW resonance is altered following unilateral stroke in $S1_{FP}$. As in **Figure 2.2C**, we mapped 3 Hz evoked SW power over a group-averaged epoch of stimulation to the right (**Figure 2.4A**) or left forepaw (**Figure 2.4C**), pre- and post-stroke. We then subtracted these maps to assess the relative change in 3 Hz evoked SW power and quantified total power change in the left (excluding the infarct) and right hemispheres (**Figure 2.4B,D**). Compared to baseline, right paw stimulation after stroke resulted in a significantly weaker increase in power at the stimulation frequency (3 Hz) in both hemispheres (**Figure 2.4A,B**, $^{**}P = 0.0094$ in left hemisphere, $^{**}P = 0.0075$ in right). Left paw stimulation provided more informative responses: 3 Hz power in right (contralesional) $S1_{FP}$ was largely similar to baseline (**Figure 2.4C**), but was significantly reduced in the left hemisphere. Of note, SW power was weaker in the right hemisphere outside of $S1_{FP}$, though not significantly in right hemisphere overall (**Figure 2.4D**, $^{**}P = 0.0091$ in left hemisphere, $^{NS}P = 0.16$ in right).

Importantly, in control animals without stroke, there was no significant change in 3 Hz SW power during right paw stimulation at similar timepoints 1 week apart (**Figure 2.S3**, $^{NS}P = 0.76$ in left hemisphere, $^{NS}P = 0.069$ in right). In addition, we examined spontaneous SW (1-1.5 Hz) power during stim-OFF epochs, extracted from whole runs without block averaging. We found that spontaneous SWs exhibit less power perilesionally, but not globally (**Figure 2.S4**). Thus, unilateral ablation of S1 reduces resonance of sensory-evoked SWs originating from S1 in either hemisphere, but not that of spontaneous SWs.

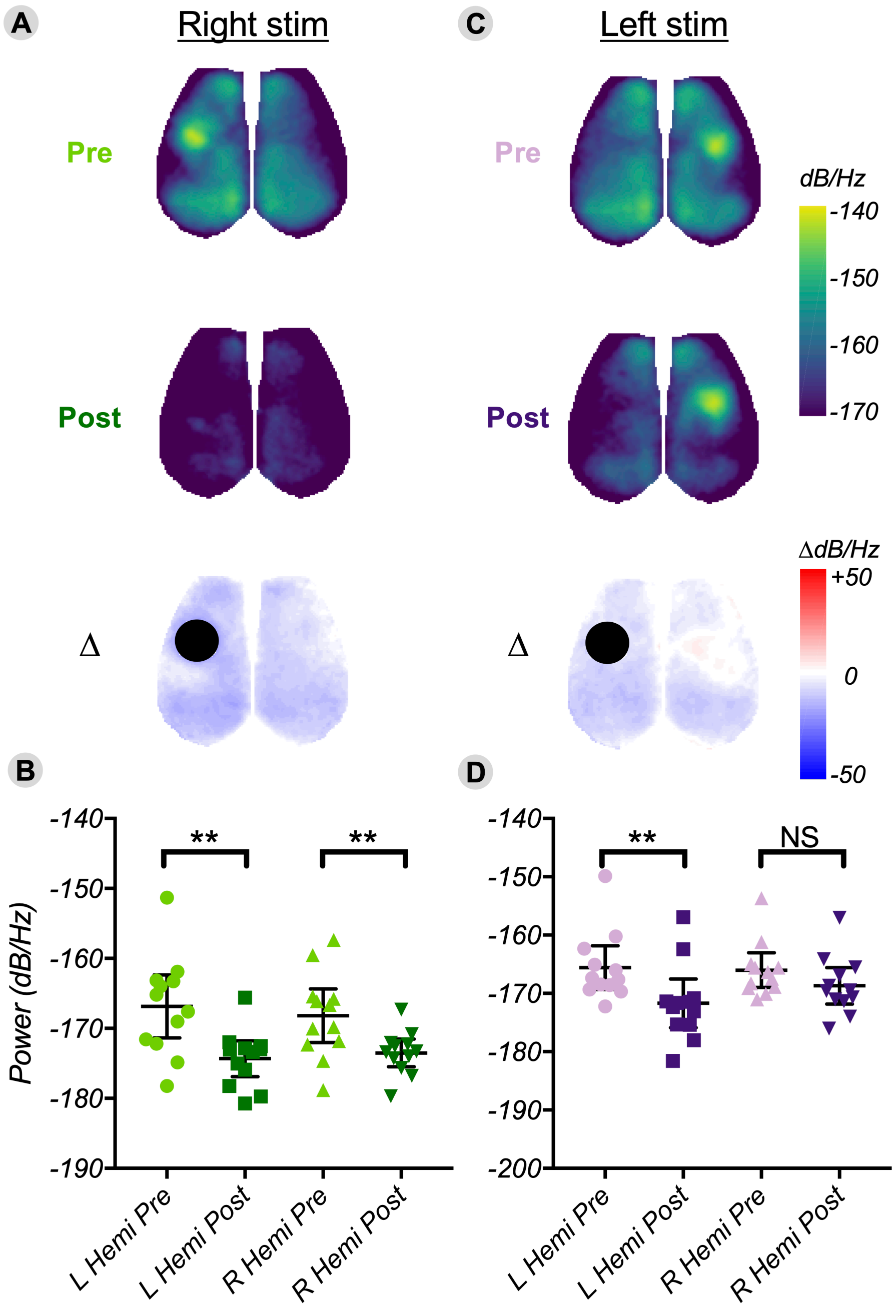

Figure 2.4. Unilateral ablation of S1 disrupts globally resonant evoked SWs in both hemispheres. (**A,C**) Cortical maps of 3 Hz evoked SW power, computed from group-average blocks, pre- and post-stroke (and Δ between them), for right (**A**) and left (**C**) paw stimulation. (**B,D**) Quantification of 3 Hz power change averaged within left and right hemispheres for right (**B**) and left (**D**) paw stimulation. Two-way ANOVA with Sidak's multiple comparison test was used to confirm significant differences. Quantification in **B** and **D** excludes the infarct so as to capture changes in surviving cortex.

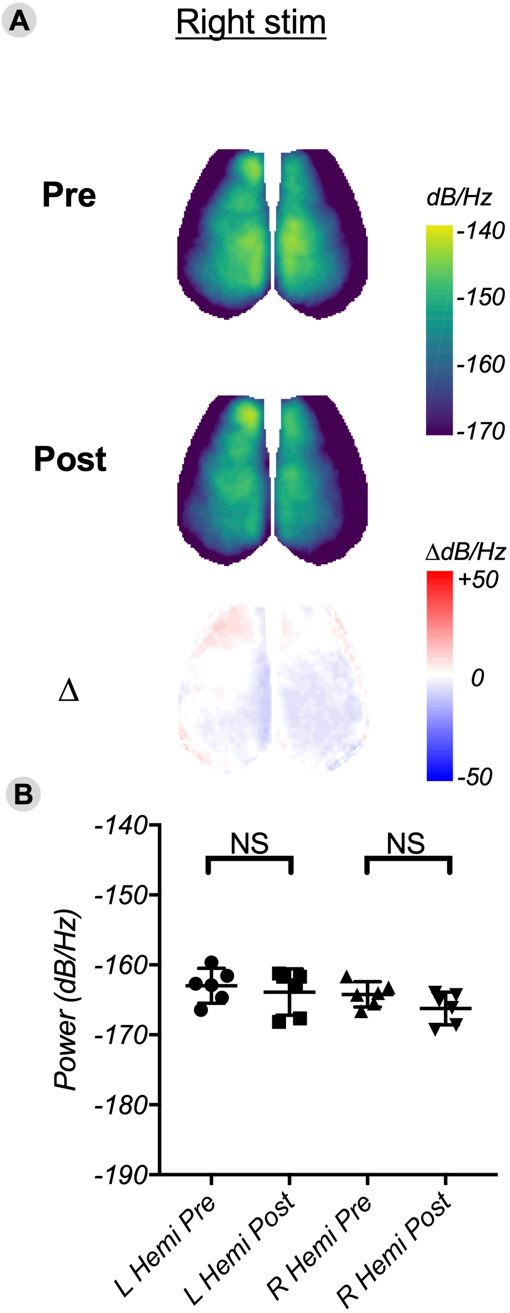

Figure 2.S3. Control mice without stroke show no change in global 3 Hz power evoked by right paw sensory stimulation across equivalent time points. Compare to Figure 2.4. (**A**) Cortical maps depicting 3 Hz evoked SW power, computed from group-average blocks at time points 1 week apart (and Δ between them). (**B**) Quantification of 3 Hz power change averaged within left and right hemispheres. Statistically significant differences are determined by two-way ANOVA with Sidak's multiple comparison test.

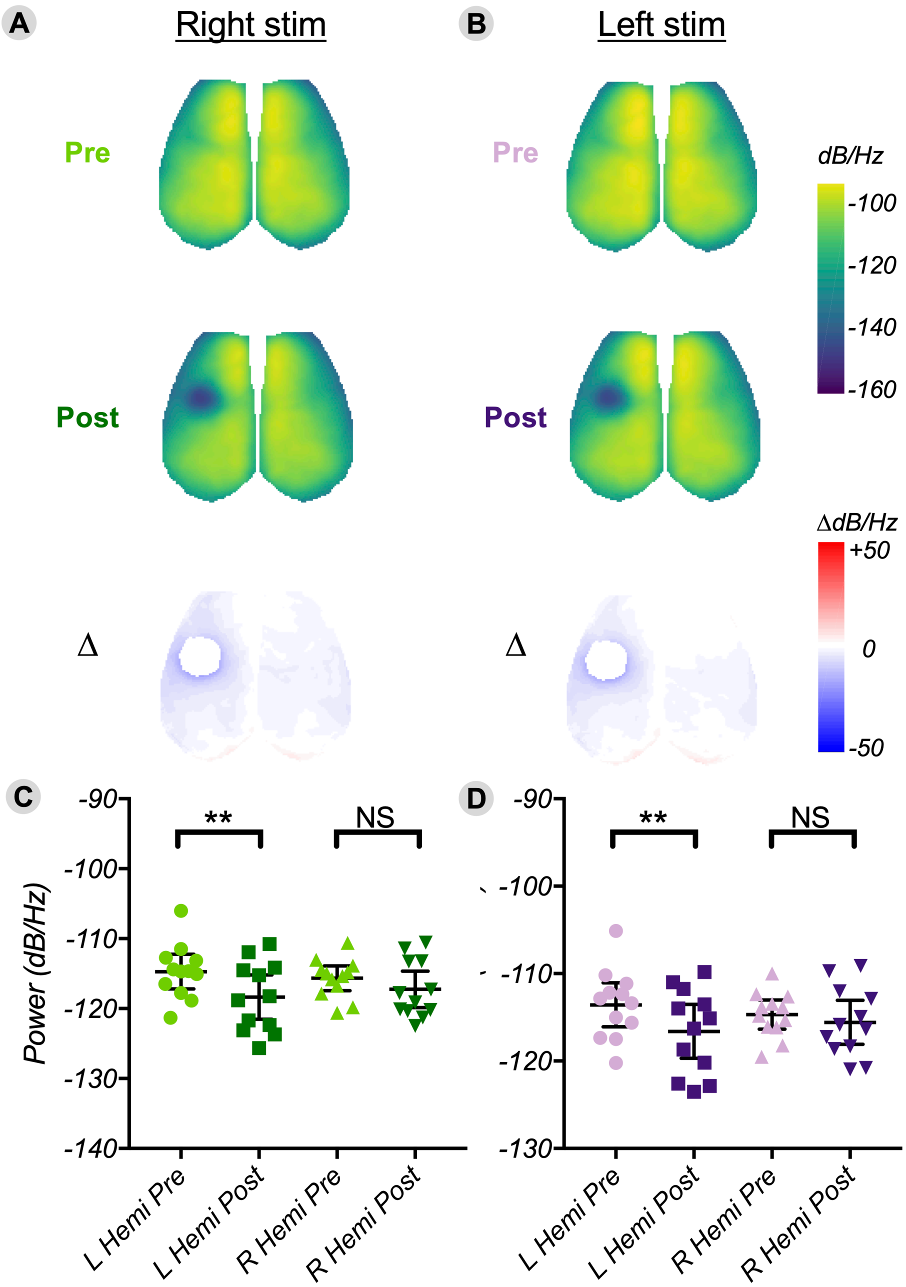

Figure 2.S4. Spontaneous 1-1.5 Hz slow wave resonance is focally attenuated in the left hemisphere in the perilesional area. (**A-B**) Cortical maps depicting spontaneous SW power (1-1.5 Hz) from whole un-averaged runs, pre- and post-stroke (and Δ between them). Spontaneous activity was extracted from OFF epochs during right (**A**) and left (**B**) paw stimulation runs. (**C-D**) Quantification of spontaneous SW power change averaged within left and right hemispheres from right (**C**) and left (**D**) paw stimulation runs. Differences are statistically tested by two-way ANOVA with Sidak's multiple comparison test. During OFF epochs from right paw stimulation, left hemisphere

spontaneous SW power is significantly decreased after stroke ($^{**}P = 0.0036$), primarily in the perilesional area, while right hemisphere SW power is unchanged ($^{NS}P = 0.20$). During OFF epochs from left paw stimulation, left hemisphere spontaneous SW power is significantly lower ($^{**}P = 0.0044$), again observed primarily in the perilesional area, while right hemisphere SW power is unchanged ($^{NS}P = 0.45$).

2.4 Discussion

Slow waves are global, traveling oscillations, a fact that has been demonstrated at the microscopic level of individual neurons (Volgushev et al., 2006, Luczak et al., 2007), within and between mesoscopic cortical territories (Petersen et al., 2003, Stroh et al., 2013, Omer et al., 2019), and macroscopically across the whole cortex in both humans and mice (Massimini et al., 2004, Mohajerani et al., 2010). Over the last three decades, research on anatomic circuitry underlying SWs has largely focused on untangling the contributions of cortex versus the thalamus (Neske, 2015). These investigations have primarily relied on local electrophysiological recordings. As a result, broader questions about how these circuits contribute to global propagation within large-scale cortical networks have received less attention. Here, we investigate how specific cortical modules contribute to global propagation. In particular, we ask, how does primary somatosensory cortex contribute to sensory-evoked global SWs?

Our results suggest that global slow waves in response to unilateral somatosensory stimulation depend on bilateral primary somatosensory cortices. Specifically, we observe that 1) somatosensory stimulation induces traveling waves originating from S1 with state-dependent trajectories; 2) under anesthesia, rhythmic stimulation evokes resonant slow waves across the whole cortex at the imposed stimulation frequency; 3) unilateral lesioning of S1 disrupts global SWs triggered by sensory stimulation of both ipsilesional and contralesional cortices; 4) in contrast, ablation of S1 leaves spontaneous global SWs unchanged outside of the perilesional area. To the best of our knowledge, this study is the first to demonstrate the necessity of a specific region of cortex in triggering slow waves. Taken together, these findings suggest that peripheral stimulation engages homotopically-connected somatosensory cortices to initiate globally resonant slow waves.

What role does S1 play in peripherally evoked versus spontaneous SWs?

Our understanding of the circuitry supporting SWs is informed by the observation that SWs arise spontaneously, but are also triggered by both peripheral and direct cortical stimulation. Spontaneous SWs have been shown to originate primarily in prefrontal-orbitofrontal regions, and propagate as front-to-back waves (Massimini et al., 2004). However, spontaneous SWs also exhibit complex local distributions in humans (Murphy et al., 2009, Nir et al., 2011) and mice (Mohajerani et al., 2010). Stimulation approaches have proven useful for dissecting the circuitry underlying observed patterns of cortical SWs. For example, transcranial magnetic stimulation (TMS) during sleep induces SWs originating underneath the stimulating coil; this approach has revealed that sensorimotor regions elicit the most robust and reliable slow waves (Massimini et al., 2007). Indeed, sensory cortex may be uniquely positioned to transmit local activity changes into global networks (Gollo et al., 2017, Rosenthal et al., 2020) Consistent with this finding, peripheral sensory stimulation in sleeping humans evokes activity with stereotypical topography: early responses in the sensory cortex specific to the stimulated modality, followed by a non-specific global anterior-posterior slow wave (Riedner et al., 2011). This dual response could be due to either parallel activation of specific and nonspecific sensory pathways, or alternatively, initial activation of primary sensory areas expanding globally through cortico-cortical connections (Riedner et al., 2011, Bellesi et al., 2014). Disambiguating these possibilities is challenging with scalp EEG owing to limited spatial resolution and reliance on inverse source modeling (Riedner et al., 2011). Here, using widefield optical imaging of pyramidal calcium dynamics in mice, we provide evidence supporting a model in which global recruitment depends on local S1 responses. Specifically, we corroborate that sensory stimulation elicits an early, modality-specific response in S1, which can be observed propagating contiguously towards frontal cortex, followed by a front-to-back slow wave (**Figure 2.1**). Ablating S1 eliminates both the local and global components of this two-part wave (**Figures 2.3,4)**, indicating that primary sensory cortex activation is necessary to initiate subsequent global waves. Future studies should investigate the role of direct and indirect connectivity between sensory and frontal cortices in triggering anterior-posterior waves. In contrast to evoked SWs, we observe that spontaneous global SWs remain globally coherent (**Figure 2.3**) and that their resonance remains intact outside of the perilesional area (**Figure 2.S4**), indicating that the circuits required for generating spontaneous SWs are not specifically dependent on S1.

Bilateral recruitment of S1 for SWs evoked by unilateral stimulation

We further show that global SW propagation engages interhemispheric connectivity. Somatosensory stimulation under ketamine/xylazine anesthesia elicits SWs bilaterally, and unilaterally lesioning S1 disrupts global SW generation in response to stimulating either hemisphere (**Figure 2.3,4**). This finding suggests that interhemispheric interaction between homotopic somatosensory cortices mediates global SW generation in response to stimulation. These effects may be conveyed by direct callosal and/or indirect subcortical interhemispheric connections. A recent study in sleeping humans showed that severing the corpus callosum disrupts the interhemispheric spread of spontaneous SWs without changing the total amount of cortical SW activity (Avvenuti et al., 2020). Thus, while callosal connectivity is necessary to synchronize activation of the two hemispheres, it does not appear to be necessary to trigger spontaneous SWs in either one separately. Likewise, SWs are bilaterally symmetric in wild-type mice, but not in acallosal mice (Mohajerani et al., 2010). In this context, our findings corroborate that interhemispheric connectivity plays a central role in synchronizing SWs bilaterally, very likely via the corpus callosum.

State-dependence of propagating low-frequency activity

We have previously shown that spontaneous global waves in the infraslow (<0.1 Hz) and delta band (1-4 Hz) exhibit stereotypical, opposing trajectories that flip between wake and anesthesia (Mitra et al., 2018). Here, we extend those findings by showing that stimulation-evoked globally propagating delta band activity likewise exhibits predominantly posterior-to-anterior waves in awake animals, and flip to predominantly anterior-to-posterior slow waves under anesthesia. Previous reports comparing evoked responses during wake and anesthesia have not addressed this phenomenon. One experiment using voltage sensitive dye (VSD) imaging in mice reported that sensory stimulation elicits complex, spatially broad traveling waves that terminate in parietal association areas, with no differences between wake and isoflurane anesthetized states (Mohajerani et al., 2013). Differences between these and our results may stem from the choice of anesthetic agent. Ketamine elicits more robust slow waves than isoflurane (Hablitz et al., 2019). Furthermore, isoflurane has been shown to weaken interhemispheric functional connectivity and spatial segregation of brain networks, and virtually abolishes corticothalamic synchrony (Bukhari et al., 2018). Previous studies have used isoflurane during craniotomy preps immediately prior to “awake” VSD imaging. Thus, differences between wake and anesthesia may be masked by residual effects of isoflurane. Another VSD study observed that whisker stimulation elicits spatially broad activations from S1 to M1 in both awake and urethane anesthetized animals (Ferezou et al., 2007). Consistent with our findings, supplementary videos show that evoked global waves exhibit state-dependent changes in spatial trajectory (Ferezou et al., 2007). Future investigations may further our understanding of the state-dependence of sensory-evoked global waves in naturally sleeping animals, though this remains practically challenging.

Potential contributions of subcortical hubs

Our lesion experiment results imply a role for S1 and its intracortical connectivity in eliciting slow waves. Alternatively, it is possible that the loss of global propagation is influenced by secondary injury to corticothalamic connectivity (Aswendt et al., 2020). The role of the thalamus in cortical SWs has been historically controversial. Early studies suggested that SWs are intrinsically cortical in origin, since slow oscillations persist in isolated cortical preparations and propagate via recurrent intracortical excitatory connections (Sanchez-Vives and McCormick, 2000, Timofeev et al., 2000). Moreover, disconnecting intracortical linkages with lidocaine or transection disrupts long-range SW propagation (Amzica and Steriade, 1995). Other studies report that cortical SWs survive extensive thalamic lesioning (Steriade et al., 1993a) and that spontaneous cortical SW activity in brain slices is neither sustained nor influenced by activity in thalamic inputs (MacLean et al., 2005), implying that the thalamus is not necessary for generating cortical SWs. Nevertheless, intact connectivity between the thalamus and cortex likely influences the expression of cortical SWs, given that inhibiting the thalamus in naturally sleeping animals virtually abolishes cortical neuron slow oscillations (Doi et al., 2007), while thalamic activation in rats entrains and frequency tunes cortical SWs during both natural NREM sleep and anesthesia (David et al., 2013). In addition, sensory and higher-order thalamic nuclei activate sequentially during different phases of the cortical slow oscillation (Sheroziya and Timofeev, 2014). Thus, current consensus is that the cortex can intrinsically generate slow wave activity, but this activity is modulated by corticothalamic connectivity *in vivo* (Neske, 2015). In fact, several subcortical nuclei contribute to SWs in the intact brain, including the basal forebrain (Xu et al., 2015, Oishi et al., 2017), brainstem nuclei (Neske, 2015, Anaclet et al., 2014, Zhang et al., 2019), and the claustrum (Narikiyo et al., 2020). Given these complex, parallel mechanisms for rhythm generation in the cortex, further investigation will be required to determine whether focal cortical injury disrupts global SWs via loss of intracortical connectivity, subcortical connectivity, or both.

Stimulation induces changes in subsequent spontaneous SWs

Much has been learned about SW behavior from studying the interaction between ongoing intrinsic activity and afferent sensory signals (see reviews by Ferezou and Deneux, 2017, Neske, 2015). In general, up-states inhibit sensory evoked responses while down-states amplify them (Petersen et al., 2003, Civillico and Contreras, 2012). This interaction may serve to gate cortical response to sensory inputs (Luczak et al., 2013). Likewise, evoked activity elicits changes in subsequent spontaneous activity. Rhythmic sensory stimulation resets the phase of spontaneous neuronal oscillations so that inputs arrive at an optimal high excitability phase (Lakatos et al., 2007). In awake animals, rhythmic entrainment of spontaneous oscillations enhances attention to anticipated stimuli (Lakatos et al., 2008). However, entrainment of sensory stimuli also occurs during slow wave sleep and anesthesia. Here, we observe phase resetting of spontaneous global SWs during ketamine/xylazine anesthesia (**Figure 2.1**, **Supplemental Videos 1-3**), evident in phase-locked reverberations during the post-stimulation period that survive averaging across over 500 blocks. This result is consistent with prior demonstrations of entrainment and phase-resetting of slow oscillations by rhythmic breathing/olfactory stimulation (Fontanini et al., 2003), forepaw stimulation (Chen et al., 2020a), whisker stimulation (Hartings et al., 2003, Ewert et al., 2008), auditory stimulation (He, 2003, Gao et al., 2009), and direct optogenetic stimulation of motor cortex (Kuki et al., 2013, Beltramo et al., 2013). Building off of these electrophysiologic studies, fast optical imaging techniques have revealed that stimulation-like spatial activations replay during the post-stimulation period, for example within V1 after visual stimuli (Han et al., 2008) and broadly across the cortex after bilateral electric field stimulation (Greenberg et al., 2018). We further confirm that reverberation can occur at the scale of global SWs phase-reset by preceding sensory stimulation.

These findings beg the question – what is the function of global SWs? The last decade has seen exciting discoveries about slow waves (Bellesi et al., 2014), which can potentiate cortical responses (Megevand et al., 2009), induce plasticity in spiking dynamics (Hishinuma et al., 2019), prolong sleep (Bayer et al., 2011), generate pulsations in CSF flow (Hablitz et al., 2019, Fultz et al., 2019), and perhaps most strikingly – enhance memory consolidation (Marshall et al., 2006, Kirov et al., 2009, Ngo et al., 2013, Binder et al., 2014, Ladenbauer et al., 2016). Thus, the interaction of sensory activity and internal slow waves has important implications for brain function that warrant further study.

Translational implications of SW disruption after stroke

Another significant gap in our understanding of slow waves lies in how they are disrupted by injuries, such as stroke. Here, we observe that stroke in S1 can disrupt somatosensory-evoked global slow waves, as well as attenuate local spontaneous SW activity in the perilesional area. Photothrombosis produces highly focal, circumscribed lesions that provide insight into the effects of cortical death on SWs. However, this model does not recapitulate the graded ischemic injury observed in the penumbra of natural strokes. In the setting of a true ischemic penumbra, EEG studies in humans have demonstrated that SW sleep activity is increased around infarcts (Poryazova et al., 2015), in tandem with the emergence of pathological peri-infarct SWs during wakefulness (Sarasso et al., 2020). Thus, stroke may disrupt SWs by divergent mechanisms, both due to death of circuits generating SWs, as well as dysfunction in surviving neurons in the peri-infarct zone. These observations carry important implications for large-scale functional connectivity. Stroke has been shown to disrupt global functional connectivity (FC) in both humans, (Baldassarre et al., 2016, Carter et al., 2012, Grefkes and Fink, 2011, Dijkhuizen et al., 2014) and rodents (van Meer et al., 2010, Lim et al., 2014, Bauer et al., 2014). Similar mechanisms may underlie SW dysfunction and large-scale FC changes (Neske, 2015, Buzsaki and Draguhn, 2004). Just as recovery of FC is predictive of stroke recovery, recovery of SW dynamics during rehabilitative therapy has likewise been shown to predict functional recovery (Sarasso et al., 2014). The present findings invite further investigation of the circuit mechanisms of SW physiology and dysfunction, and suggest potential uses of SWs as a biomarker of brain network integrity.

2.5 Materials and Methods

Mouse model

All procedures described below were approved by the Washington University Animal Studies Committee in compliance with AAALAC guidelines. Mice were raised in standard cages in a double barrier mouse facility with a 12hr-12hr light/dark cycle and *ad libitum* access to food and water. All experiments used 10-12 week old males hemizygous for *Thy1-GCaMP6f* (JAX 024276) on a C57BL/6J background. Mice of this strain express GCaMP in pyramidal neurons, permitting wide-field cortical imaging of excitatory calcium dynamics, which correlates well with multi-unit activity (Dana et al., 2014, Murphy et al., 2018, Ma et al., 2016b). Prior to experiments, pups were genotyped by PCR to confirm presence of the *Thy1-GCaMP6f* transgene, using the forward primer 5'-CATCAGTGCAGCAGAGCTTC-3' and reverse primer 5'-CAGCGTATCCACATAGCGTA-3'.

Cranial windowing

Mice received buprenorphine analgesia (SQ, 0.03 mg/kg) and were anesthetized with isoflurane (3% induction, 1.5% maintenance). Body temperature was maintained via thermostatic heating pad. Mice were secured in a stereotactic frame. The scalp was shaved, sterilized with isopropyl alcohol and betadine scrub, locally anesthetized with lidocaine, and then incised at midline and retracted. A custom Plexiglas window with pre-tapped screw holes for head fixation was attached to the skull using dental cement (C&B-Metabond, Parkell Inc., Edgewood, NY), completely containing the surgical opening.

Photothrombosis

Protocol was performed as previously described (Kraft et al., 2018), and is established to deliver focal, well-circumscribed, highly reproducible lesions (Maxwell and Dyck, 2005). Briefly, mice (*n*=12) were injected with Rose Bengal (6.7 mg/kg, IP), and a green DPSS laser (532nm, 23 mW) collimated to a 1mm spot was stereotactically centered on the Paxinos coordinates of forepaw sensory cortex (-2.2 mm in X, +0.05 mm in Y versus bregma) for 10 min (Franklin and Paxinos, 2012). Cessation of blood flow was confirmed via laser Doppler.

Infarct volume histology

A separate cohort of three animals were sacrificed three days after photothrombosis. Mice were deeply anesthetized with FatalPlus^{TM} (Vortech Pharmaceuticals, Dearborn, MI, USA) and transcardially perfused with heparinized PBS. The brains were removed and fixed in 4% paraformaldehyde for 24 h and transferred to 30% sucrose in PBS. After brains were saturated, they were snap-frozen on dry ice and coronally sectioned (50 μm) on a sliding microtome. Sections were stored in 0.2 M PBS, 30% sucrose, and 30% ethylene glycol at −20°C. For each brain, 3 sections (spaced 300 μm apart, spanning the infarct) were stained the cresyl violet. A blinded experimenter traced infarct sizes in ImageJ to measure infarct area, which was then multiplied by distance between sections to estimate infarct volume.

Optical imaging system

Widefield imaging of cortical calcium dynamics was performed as previously described (Wright et al., 2017b). Briefly, sequential illumination was provided by four LEDs: the 454nm (blue) LED was used for GCaMP excitation, while the 523nm (green), 595nm (yellow), and 640nm (red) were used for hyperspectral oximetric imaging. The 523nm LED was also used as an emission reference to remove any confound of hemoglobin in the fluorescence signal using a previously validated method (Ma et al., 2016a). The acquisition framerate was set to 16 Hz per channel for whisker imaging studies, and 16.81 Hz per channel for forepaw stroke experiments. For image detection, we used a cooled, frame-transfer EMCCD camera (iXon 897, Andor) with an 85mm f/1.4 camera lens and 67 Hz framerate (Rokinon). The field-of-view was approximately 1 cm^2, covering most of the dorsal convexity of the cerebral cortex. The resulting pixels were approximately 78μm x 78μm.

Optical imaging recordings

Mice were acclimated to head-fixation while secured in a comfortable black felt hammock until they resumed normal resting behavior (whisking, grooming, relaxed posture). Mice were imaged while awake and/or while anesthetized via intraperitoneal injection with a cocktail of ketamine (86.9 mg/kg) and xylazine (13.4 mg/kg). Animals were allowed 10 minutes for anesthetic induction, with the plane of anesthesia measured by respiratory rate and loss of responsiveness to toe pinch. After induction, body temperature was maintained by a thermostatic heating pad with feedback via rectal probe (TCAT-2LV; HP-4M, Physitemp). Whisker stimulation recordings were performed in 10-minute epochs, with stimulation delivered using computer-triggered 40

PSI air puffs (Picospritzer, Parker Hannifin, Cleveland, OH) in a block design (5s of 2 Hz, 0.1s puffs; 5s rest; 60 blocks/10 min. total per mouse, *n=10* mice for awake, *n=9* mice for anesthesia). One recording of whisker stimulation under ketamine was omitted due to a file saving error. For stroke imaging experiments, imaging sessions were conducted at baseline, and then 1 week after photothrombosis. At each imaging session, forepaw stimulation was delivered by transcutaneous electrical stimulation using microvascular clips (Roboz) in a block design (5s rest; 5s of 3 Hz, 1.0 mA, 0.3 ms electrical pulses; 10s rest; 15 blocks/5 minutes per mouse x *n=12* mice). Control studies were performed in a separate age-matched cohort cohort of *n*=6 male mice without strokes.

Optical imaging signal processing

A binary brain mask was manually drawn in MATLAB for each recording session in each mouse. All subsequent analyses were performed on pixels labeled as brain. Image sequences from each mouse (as well as the brain mask for each mouse) were affine-transformed to Paxinos atlas space using the positions of bregma and lambda (Franklin and Paxinos, 2012), and then spatially and temporally detrended as previously described (Wright et al., 2017b). The GCaMP6 fluorescence signal (%dF/F) was corrected for varying concentrations of absorptive hemoglobin using 523nm LED reflectance.

Optical imaging ROIs

Regions of interest (ROIs) for whisker barrel cortex ($S1_W$) and forepaw sensory cortex ($S1_{FP}$) were determined based on functional stimulus mapping from an independent cohort of 21 twelve-week-old *Thy1-GCaMP6f* mice using the same stimulation paradigms as described above. Blocks were averaged within each mouse and then the peak frames for each of 10 air puffs/10 s block or 15 shocks/20 s block were averaged into one mean maximal amplitude frame per mouse. Mean maximal amplitude frames were averaged across mice, and then an evoked response ROI was defined by any pixels whose mean maximal amplitude during stimulus was >75% of the maximum pixel intensity within the brain. ROIs generated from this approach were used in subsequent analyses for averaging within functional territories. ROI locations are co-registered to experimental data using affine-transformation to Paxinos atlas space. An infarct ROI was defined in this cohort using resting state awake functional connectivity data, defining the infarct pixels by their loss of homotopic FC as previously described (Rosenthal, 2017).

Space-frequency SVD

Frequency-specific propagation structure and global coherence were characterized via singular value decomposition (SVD) of optical imaging data in the frequency domain. Performing SVD on multitaper spectral estimates provides a computationally efficient strategy to spectrally smooth and decompose time series data (Prechtl et al., 1997, Mitra and Pesaran, 1999a). Thus, K Slepian tapers of bandwidth W were applied to pixelwise Fourier transforms. The resulting space-frequency matrix was decomposed into K spatially orthogonal complex modes at each frequency f, each with coherence magnitude and phase information. A single dominant mode was observed in each condition; hence, analyses were restricted to the first component.

SVD was applied to full runs for spontaneous activity (time-bandwidth product $TW = 12$, $K = 22$ tapers; results were robust to different parameter choices) or block-averages for evoked activity ($TW = 3$, $K = 5$ tapers) (spontaneous and evoked were not directly compared), and the dominant spatial mode was averaged across runs. Note that complex singular vectors are unique up to a complex sign (i.e., a unit phase factor). Thus, dominant spatial modes were phase-aligned by rotation in the complex plane according to a reference phase value (here, the global circular mean phase of the mode) prior to averaging across runs.

Following SVD, a measure of global coherence $C(f)$ is provided by the fractional power of the first mode:

$$C(f) = \frac{{\lambda_1}^2(f)}{\sum_{k=1}^{K} {\lambda_k}^2(f)} \tag{E1}$$

Post-stroke global coherence calculations excluded the infarct so as to capture changes in surviving cortex. Space-frequency SVD was implemented in MATLAB and incorporated software routines from the freely available Chronux package (Bokil et al., 2010). Changes in global coherence between states were statistically tested within individual mice by paired two-tailed t-test, with significance set at *P* < α=0.05.

Power spectral analysis

Global power spectrograms (Figure 2.3A) were generated by computing the global average %dF/F signal across all brain mask pixels within each mouse/run, and then performing a short time Fourier transform (STFT) using a 5 second window with 0 overlap to capture the spectral signature of each individual 5 second ON or OFF period within each block. Spectrograms were computed within individual mice and then averaged across mice. Power spectra (Figure 2.3B) were computed by averaging across all ON or OFF windows from spectrograms in Figure 2.3A. Note spectra were not normalized to total power, allowing comparison of changes to absolute rather than relative band-limited power across conditions. Frequency-specific changes between the ON and OFF spectra in Figure 2.3B were analyzed by two-way ANOVA with Sidak's multiple comparison test (comparing across frequency bins), with significance set at an adjusted *P*-value < α=0.05. Block-averaged power maps (Figure 2.3C, 2.5A-C) were generated by averaging the %dF/F signal across all blocks within each mouse/run, and then computing power at each pixel using Welch's method. Power maps were averaged within each hemisphere for each mouse, and pre- vs. post-stroke changes were statistically tested by repeated measures one-way ANOVA with Sidak's multiple comparison test (comparing within individual mice across time points), with significance set at an adjusted *P*-value < α=0.05. All power values were converted from arbitrary units into decibels/Hz using the equation:

$$Power\left(\frac{dB}{Hz}\right) = 10\log_{10}\left(Power\ (a.u.)\right) \tag{E2}$$

Experimental design and statistical analysis

Histograms and spectra are plotted as group mean ± 95% confidence interval error bars. Individual data points represent individual mice. Sample size and specific time points were selected on the basis of previous studies examining network connectivity changes in mice (Kraft et al., 2018, Brier et al., 2019, Rosenthal et al., 2020). Prism 8 software was used to perform statistical testing. Tests used for each analysis are underlined above. Data were verified to be normally distributed prior to statistical testing using the D'Agostino & Pearson normality test. Throughout, significance of *P* values is depicted as $^{*}P < 0.05$, $^{**}P < 0.01$, $^{***}P < 0.001$, and $^{****}P < 0.0001$.

Chapter 3: Local perturbations of cortical excitability propagate differentially through large-scale functional networks

3.1 Abstract

Electrophysiological recordings have established that GABAergic interneurons regulate excitability, plasticity, and computational function within local neural circuits. Importantly, GABAergic inhibition is focally disrupted around sites of brain injury. However, it remains unclear whether focal imbalances in inhibition/excitation lead to widespread changes in brain activity. Here, we test the hypothesis that focal perturbations in excitability disrupt large-scale brain network dynamics. We used viral chemogenetics in mice to reversibly manipulate parvalbumin interneuron (PV-IN) activity levels in whisker barrel somatosensory cortex. We then assessed how this imbalance affects cortical network activity in awake mice using wide-field optical neuroimaging of pyramidal neuron GCaMP dynamics as well as LFP recordings. We report 1) that local changes in excitability can cause remote, network-wide effects, 2) that these effects propagate differentially through intra- and interhemispheric connections, and 3) that chemogenetic constructs can induce plasticity in cortical excitability and functional connectivity. These findings may help to explain how focal activity changes following injury lead to widespread network dysfunction.

3.2 Introduction

GABAergic interneurons play a vital role in maintaining excitatory/inhibitory (E/I) balance at multiple spatial scales (Bhatia et al., 2019). Such balance homeostatically stabilizes local circuit activity (Maffei et al., 2006, Barral and Reyes, 2016), governs plasticity during developmental critical periods (Hensch, 2005), and shapes behavior (Yizhar et al., 2011). However, most studies of E/I balance have examined neural activity with micro-scale techniques such as electrophysiology and 2-photon imaging. These spatially-restricted approaches may overlook larger-scale effects on widely distributed brain networks. Macro-level techniques such as fMRI and EEG have revealed that, within large-scale functional networks (e.g., motor, visual, default mode), interconnected brain loci exhibit synchronized activity, a phenomenon widely known as functional connectivity (FC) (Fox and Raichle, 2007). Computational models predict that E/I balance is a key contributor to the organization of FC networks (Deco et al., 2014). In accordance with this prediction, stroke, focal seizures, and traumatic brain injury (TBI) all disrupt regional E/I balance (Carmichael, 2012, Farrell et al., 2019, Mishra et al., 2014) as well as brain-wide FC patterns (Englot et al., 2016, Caeyenberghs et al., 2017, Silasi and Murphy, 2014), leading to network dysfunction thought to underlie chronic neurocognitive impairment. However, it remains to be empirically determined whether focal E/I imbalance plays a causal role in disrupting large-scale network activity, independent of injury.

The rodent whisker sensorimotor network is a well-characterized large-scale cortical network in mice, both structurally and functionally, making it an ideal model to examine the effects of focal E/I manipulation on systems-scale dynamics. This network exhibits strong monosynaptic projections and intrahemispheric FC between $S1_W$ and the whisker motor cortex ($M1_W$), as well as strong interhemispheric FC between motor cortices, but weaker connectivity between somatosensory cortices (Ferezou et al., 2007, Bauer et al., 2018, Sreenivasan et al., 2016). Recent work emphasizes a prominent role of inhibitory connectivity, in particular parvalbumin interneurons (PV-INs), in gating dynamics within this circuit (Pala and Petersen, 2018, Sachidhanandam et al., 2016). PV-INs are the most prevalent GABAergic cell-type, provide fast feedforward inhibition onto pyramidal neuron soma and, as we will expand upon in the Discussion, are critical for regulating local E/I gain control, making them ideal targets for E/I manipulation.

Here, we used virally-delivered DREADDs (Designer Receptors Exclusively Activated by Designer Drugs) to reversibly and focally manipulate activity in PV-INs within the mouse whisker barrel somatosensory cortex ($S1_W$). We sought to determine how this perturbation of local E/I balance influences large-scale cortical dynamics by monitoring cortical activity in awake mice using concurrent widefield optical neuroimaging (GCaMP calcium dynamics in pyramidal neurons) and oxy-hemoglobin hemodynamics (oxy-Hb optical intrinsic signal), as well as local field potential (LFP) recordings in separate experiments. Our results reveal that perturbations in PV-IN activity in $S1_W$ produce local E/I imbalance that propagates differentially through intra- and interhemispheric connections of the whisker sensorimotor network. These findings may allow insight into how brain networks respond to local changes in activity after injury, as well as how large-scale network dysfunction might be counteracted with targeted neuromodulatory therapy.

3.3 Results

Efficient and specific viral delivery of DREADDs to $S1_W$ parvalbumin interneurons

We crossed the *Thy1-GCaMP6f* strain of mice (which permit fluorescence neuroimaging of pyramidal neuron calcium dynamics through the intact skull (Wright et al., 2017b) with the *PV-Cre* strain (to enable PV-specific expression of floxed viral constructs). Offspring were divided into three groups, each receiving stereotactic injection in the left whisker barrel primary somatosensory cortex ($S1_W$) with a Cre-inducible chemogenetic viral construct: (1) hM3Dq, to increase PV (↑PV) inhibitory activity and decrease excitability, (2) hM4Di, to decrease PV (↓PV) inhibition and increase excitability, or (3) mCherry only, as a Control (**Figure 3.1A**). hM3Dq and hM4Di are Designer Receptors Exclusively Activated by Designer Drugs (DREADDs), engineered muscarinic channels that are activated by the synthetic drug, clozapine-N-oxide (CNO). The effects of DREADDs on activity in PV-INs have been extensively characterized in prior studies (Kuhlman et al., 2013, Chandrasekar et al., 2019, Williams and Holtmaat, 2019, Liu et al., 2017, Sun et al., 2016, Funk et al., 2017, Stedehouder et al., 2018, Calin et al., 2018).

We histologically validated the delivery of DREADD constructs in each group (*n*=5 mice/group), and found that expression of viral constructs was well-circumscribed within the Paxinos atlas boundaries of $S1_W$ (**Figure 3.1B**), with no detectable expression in the rest of the cortex. Gross spread of viral transduction was similar between groups in both medial-lateral width (Control: 1.52±0.16 mm, ↑PV: 1.91±0.15 mm, ↓PV: 1.77±0.09, corrected $^{NS}P=0.28$), and mean coronal cross-sectional area (Control: 1.33±0.27 mm^2, ↑PV: 1.92±0.26 mm^2, ↓PV: 1.56±0.12 mm^2, $^{NS}P=0.27$). In addition, mCherry fluorescence in putative PV-INs was distributed in all cortical layers, and did not colocalize with *Thy1*-GCaMP fluorescence in pyramidal neurons (**Figure 3.1C**). Lastly, we compared colocalization of mCherry fluorescence versus immunostaining with an anti-parvalbumin antibody. All three virus groups exhibited high transduction efficiency of PV-INs on average, computed within individual mice as the fraction of all PV-immunostaining cells that expresses mCherry (**Figure 3.1D**, Control: 91.0±3.2%, ↑PV: 93.7±2.2%, ↓PV: 89.7±3.0%, corrected ^{NS}P=0.55), as well as high specificity, computed as the fraction of all mCherry-expressing cells that immunostains for PV (**Figure 3.1E**, Control: 79.2±0.2%, ↑PV: 78.4±2.2%, ↓PV: 80.1±2.9%, corrected ^{NS}P=0.88).

Mice were allowed 8 weeks of recovery after viral injection, after which cranial windows were installed over the skull for wide-field neuroimaging in one set of mice, while $S1_W$ craniotomy ports were installed for LFP recordings in a separate cohort. Mice were then habituated to handling and head-fixation. All subsequent brain recordings were performed in awake animals.

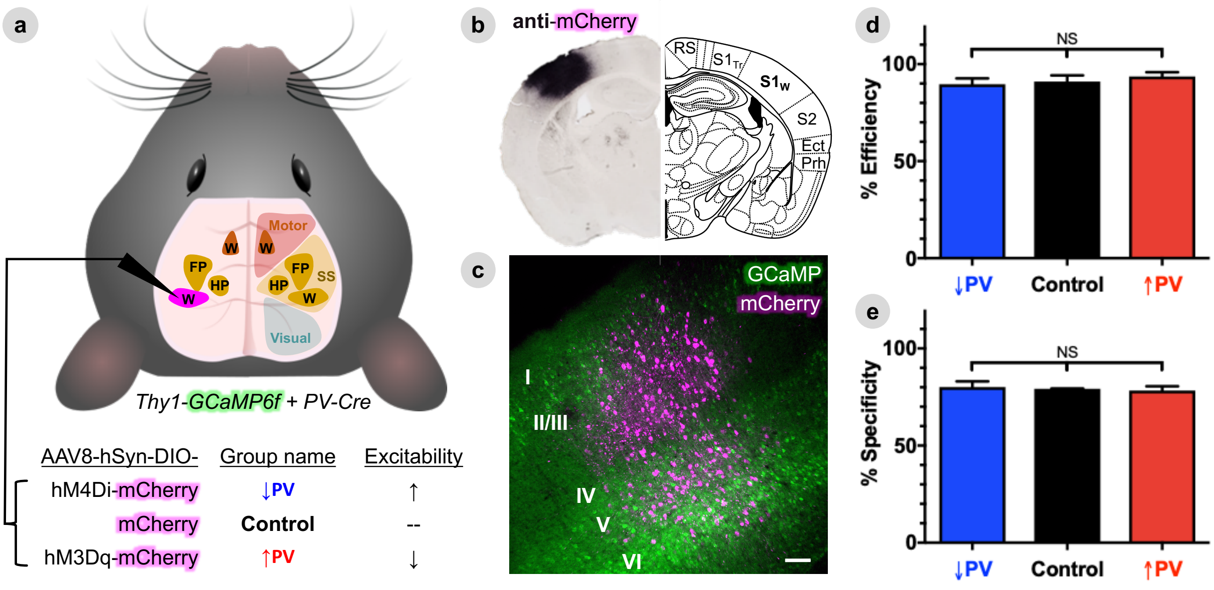

Figure 3.1. Efficient and specific viral delivery of DREADDs to $S1_W$ parvalbumin interneurons. (**A**), Experimental schematic depicting the brain field of view for widefield fluorescence imaging, with empirically determined functional territories for whisker (W)

forepaw (FP) and hindpaw (HP) plotted within motor and somatosensory (SS) areas (see Methods for ROI determination). Mice were a cross between the *Thy1-GCaMP6f* line, to permit imaging of calcium dynamics in cortical pyramidal neurons, and the *PV-Cre* line, to permit targeting of floxed (DIO) viral constructs to PV-INs. PV-INs in the left whisker barrel primary somatosensory cortex ($S1_W$, magenta) were transduced with one of three different AAV8 vectors for each of the three experimental groups. (**B**), Representative diaminobenzidine (DAB) staining of an antibody against the mCherry tag used in AAV8 constructs (left), illustrating focal and well-circumscribed viral transduction of $S1_W$ compared to predicted anatomy from the Paxinos atlas (right). RS = retrosplenial cortex, $S1_{Tr}$ = trunk primary S1, S2 = secondary somatosensory cortex, Ect = entorhinal cortex, Prh = perirhinal cortex. (**C**), Representative confocal projection image merging mCherry fluorescence (magenta) in putative PV-INs in $S1_W$ with a background of GCaMP6f fluorescence (green) in pyramidal neurons. Scale bar, 100 µm. (**D**), Average efficiency of viral transduction, calculated within individual mice as the percentage of all PV-immunoreactive cells that also co-labels with mCherry. (**E**), Average specificity of viral transduction, calculated within individual mice as the percentage of all mCherry-labeled cells that also immunostains for PV. Data are represented as mean ± SEM for each group (*n*=5 animals per group), with significance calculated by 1-way ANOVA with Tukey's multiple comparison test.

Activating $S1_W$ PV-DREADDs induces local changes in activity and excitability

To test whether chemogenetic modulation of PV-INs alters local activity, we measured calcium dynamics (GCaMP $\Delta F'$) averaged within $S1_W$ versus LFP recordings averaged over all cortical layers. GCaMP imaging was performed in one cohort with chronic cranial windows over the intact skull (↑PV *n*=12, ↓PV *n*=12, Control *n*=11), while LFP recordings were performed in a separate cohort with an open-skull head fixation (↑PV *n*=5, ↓PV *n*=6, Control *n*=5). GCaMP fluorescence is strongly correlated with multi-unit activity (Murphy et al., 2018, Ma et al., 2016b). Thus, GCaMP and LFP offer complementary perspectives on both supra- and sub-threshold neural ensemble dynamics. Representative time-series from individual mice for both signals are shown in **Figure 3.2A,B** at baseline (OFF, black), and 30 minutes after IP injection of 1 mg/kg CNO (ON, magenta). This time window for recording was chosen on the basis of DREADD effects peaking between 30-60 minutes after CNO delivery (discussed later in **Figure 3.6D**). No qualitative ON-OFF differences were observed in LFP or GCaMP time-series for either Control or ↑PV mice. However, in the ↓PV group, S1$_W$ disinhibition manifested as paroxysmal hyperexcitability, superimposed on lower amplitude fluctuations. Bursts of hyperexcitability were observed as high amplitude up-peaks in GCaMP fluorescence (**Figure 3.2A**), or down-peaks in LFP (**3.2B**).

To assess the spectral frequency content of activity changes, we generated group-averaged power spectra over 10-minute-long ON and OFF epochs (shown for GCaMP, LFP, and oxy-Hb in **Figure 3.S1A-D**), and then calculated the ON-OFF power change in decibels using equation E1 (**3.S1E**). DREADD activation in the ↓PV group broadly increased S1$_W$ spectral power in hemoglobin, GCaMP, and LFP signals. ↑PV and Control mice showed no apparent change. To quantify the distribution of band-limited power changes, we compared the short time Fourier transform (**Figure 3.S1C, S2A**) and Morse continuous wavelet transform methods for power analysis of full-band LFP data (**3.S1D, S2B**). The Fourier method offers improved frequency resolution, while the wavelet method provides stronger temporal resolution and is better suited for the analysis of paroxysmal, non-stationary time series. Both methods demonstrated qualitatively similar results; the Fourier transform was used for computing power spectral density in subsequent analyses. Power increases in the ↓PV group were observed in all frequency bands, achieving significance for activity <25 Hz (**3.S2A**). No significant ON-OFF changes were observed in any band for ↑PV or Control mice.

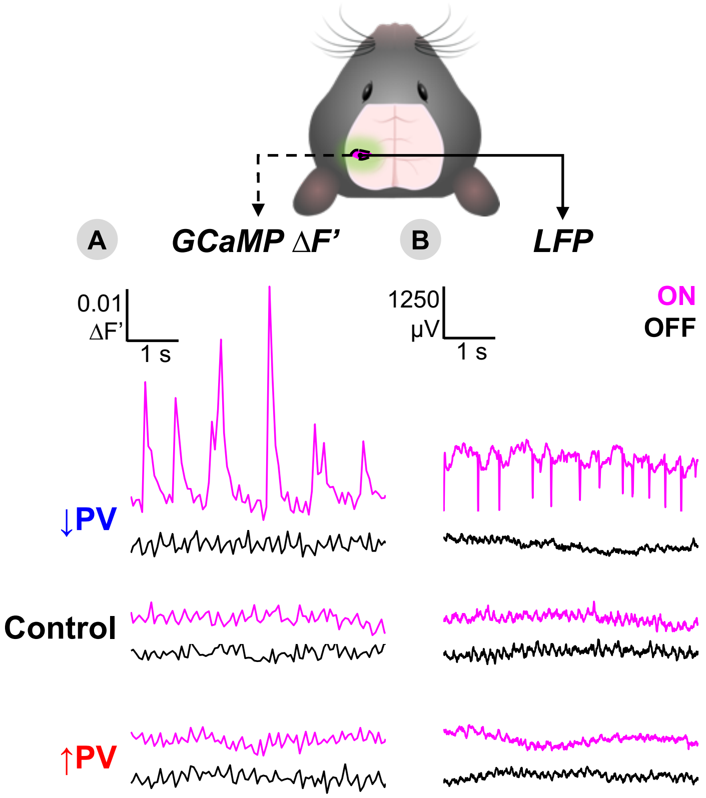

Figure 3.2. Activating S1$_W$ PV-DREADDs induces local changes in activity and excitability. (**A,B**) Representative time-series of GCaMP fluorescence (∆F’) within the left S1$_W$ ROI (**A**) and separately recorded local field potential (LFP) within S1$_W$ averaged over all cortical layers (**B**) shown for each of the three experimental groups at baseline (OFF, black) and 30 minutes after delivery of CNO (ON, magenta). See Figures 3.S1 and 3.S2 for quantification of power spectral changes.

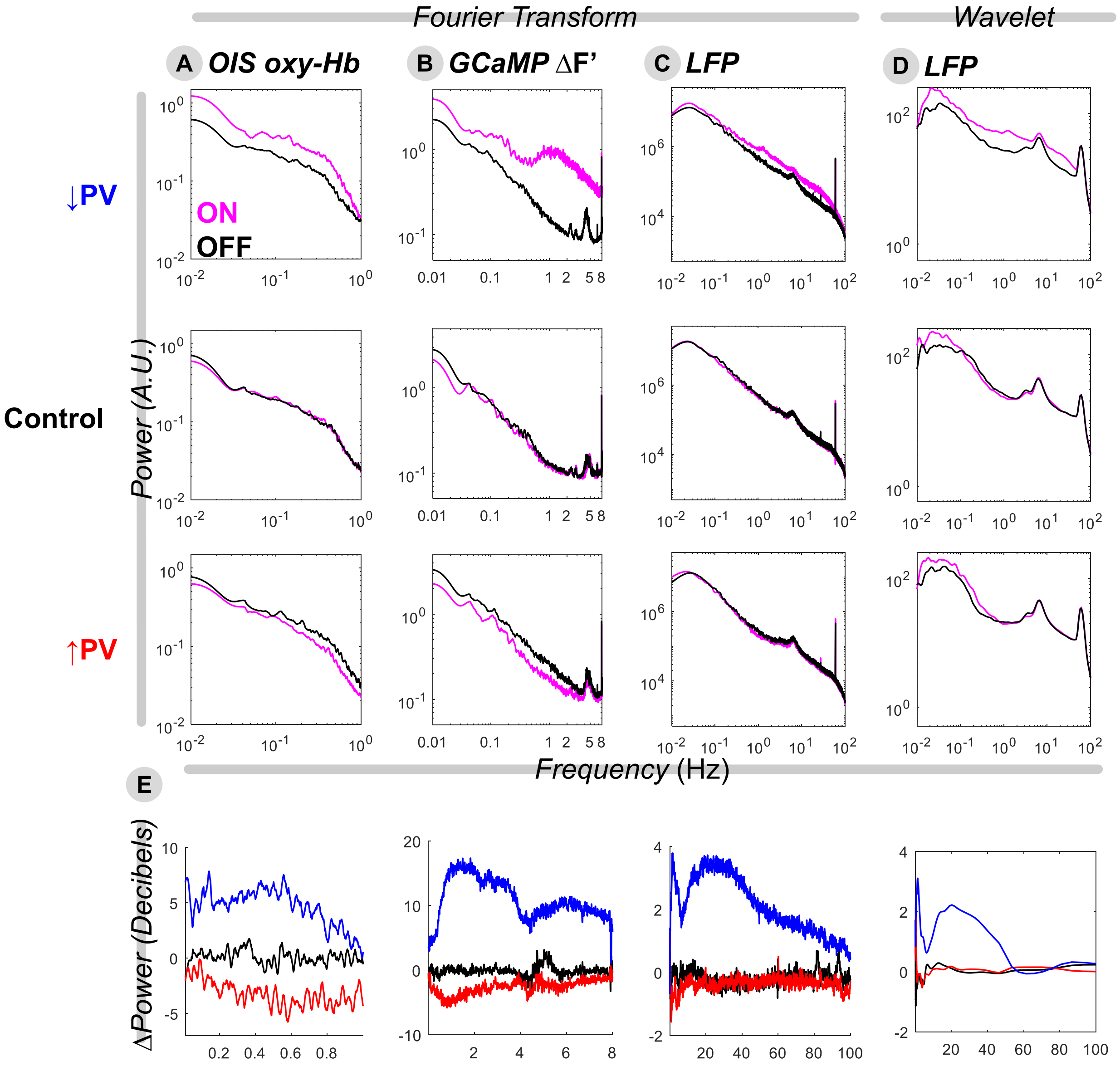

Figure 3.S1. Power spectral density computed with the fast Fourier transform for oxy-Hb optical intrinsic signal (**A**) and GCaMP fluorescence (**B**). LFP power spectra density was computed using both the short time Fourier transform (**C**) and the continuous wavelet transform (Morse wavelet) averaged over time (**D**). Within each column, change in power spectral density (ΔPower, in decibels using equation E1) is shown below (**E**). Data are shown at baseline (OFF, black) and 30 minutes after delivery of CNO (ON, magenta). All data are represented as group averages (↑PV *n*=12, ↓PV *n*=12, Control *n*=11 for neuroimaging; ↑PV *n*=5, ↓PV *n*=6, Control *n*=5 for LFP), which were statistically verified in Figure 3.S2 and Figure 3.3. Spectral peaks at ~5 Hz (GCaMP and LFP) and 60 Hz (LFP) correspond to cardiorespiratory and electrical artifact, respectively.

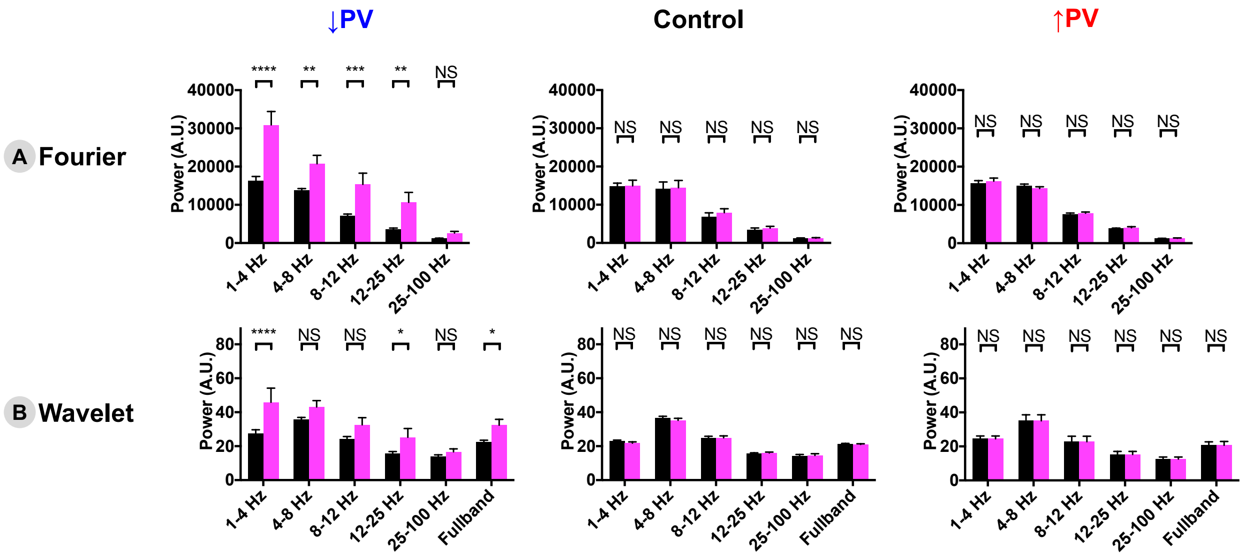

Figure 3.S2. Comparison of Fourier transform and wavelet methods for computing band-limited LFP power. All data are represented as group averages (↑PV n=5, ↓PV n=6, Control n=5), and were statistically verified by 2-way ANOVA with Sidak's multiple comparison test ($^{*}P < 0.05$, $^{**}P < 0.01$, $^{***}P < 0.001$, and $^{****}P < 0.0001$). Band-limited power changes were observed to be qualitatively similar for both methods, and the Fourier transform was used for subsequent analyses.

Locally disrupted S1$_{W}$ E/I balance bidirectionally modulates spectral power locally and in remote sensorimotor areas

We next explored the spatial extent and temporal evolution of activity changes over a 40-minute period after CNO delivery. To measure spatial extent, we scored the mean ON-OFF power change in decibels (delta band, 1-4 Hz, GCaMP) for each pixel in the cortex over successive 10-minute windows (**Figure 3.3A**). To further characterize temporal evolution over a broader frequency range, we computed group-averaged spectrograms of the 40-minute rolling change in 0.02-100 Hz S1$_{W}$ LFP power (**Figure 3.3B**, shown in time-averaged cross-section in **3.S1C,E**). For comparison with blood oxygen level-dependent (BOLD) functional MRI, we also computed the corresponding infraslow band (0.02-0.1 Hz) power change for the oxy-HB optical intrinsic signal (**Figure 3.S3**). GCaMP fluorescence has been shown to offer improved signal-to-noise and spatial specificity compared to the optical intrinsic signal(Murphy et al., 2018), though the two signals are strongly coupled to one another with a temporal offset attributable to neurovascular coupling (Ma et al., 2016b, Wright et al., 2017b, Vazquez et al., 2014). ON-OFF changes at 30 minutes post-CNO were statistically verified by 2-way ANOVA with Tukey's multiple comparison test, comparing spatially averaged spectral power within functional ROIs (**Figure 3.3C-E;** see Methods for ROI definitions) as well as average full-band LFP power (**3.3F**).

In ↓PV-ON mice (**Figure 3.3A,B**), bursting events were associated with gradually increased delta band GCaMP power over a large swath of cortex encompassing S1$_W$ (averaging 3.1 mm in medial-lateral width, top row **Figure 3.3A**). In addition, a small increase in delta power was observed in the left whisker motor cortex (M1$_W$), a region functionally and structurally connected to S1$_W$. While this remote increase did not achieve significance compared to ↓PV-OFF (^{NS}P=0.31), it was significant compared to Control-ON ($^{*}P$=0.01). Importantly, these changes are qualitatively mirrored in the infraslow oxy-Hb signal. While we did not observe paroxysmal hyperexcitability in oxy-Hb dynamics as in the GCaMP signal (**Figure 3.S3A**), we did observe a significant increase in infraslow oxy-Hb power in left S1$_W$ ($^{*}P$=0.001), but no other within- or between-group changes were statistically significant in any ROI (**Figure 3.S3B-F**). Lastly, LFP recordings corroborated that spectral power increases ensue within minutes after CNO injection in ↓PV mice and plateau at 20-30 minutes. In addition to band limited changes shown in **3.S2A**, full-band

LFP spectral power in $S1_W$ was significantly increased on average (**Figure 3.3F**, $^{****}P<0.0001$).

Conversely, we anticipated that DREADDs in the ↑PV group would decrease local $S1_W$ power. While a slight local decrease in 1-4 Hz activity was observed (**Figure 3.S1**), it was not statistically significant in GCaMP ($^{NS}P=0.14$, **Figure 3.3C**), full-band LFP ($^{NS}P=0.99$, **3.3E**), or band-limited LFP ($^{NS}P=0.99$, **3.S2**). Unexpectedly, significant ON-OFF GCaMP power reductions were even more prominent in remote connected regions: ipsilateral/left $M1_W$ ($^{****}P<0.0001$) as well as contralateral/right $M1_W$ ($^{****}P<0.0001$) (**Figure 3.3A**, quantified in **3.3C-E**). No significant infraslow hemodynamic power changes were detected in left or right $S1_W$ or $M1_W$ (**Figure 3.S3**).

In addition, we were surprised to discover that, in every ↑PV mouse, motor cortex activity was elevated at baseline in the OFF-state, before the mice had ever been exposed to CNO. ↑PV-OFF mice exhibited elevated delta power in both left $M1_W$ ($^{****}P<0.0001$) and right $M1_W$ ($^{****}P<0.0001$) compared to littermates in Control-OFF or ↓PV-OFF. This pattern was consistent across data pooled over two independent cohorts of ↑PV mice. Curiously, we found that OFF-state GCaMP time-series from individual ↑PV mice exhibited paroxysmal hyperexcitability in the motor cortex (**Figure 3.S4**), similar to that observed in $S1_W$ in the disinhibited ↓PV-ON mice in **Figure 3.2**. No baseline differences between ↑PV-OFF and Control-OFF were found in the area of viral transduction, left $S1_W$, for either GCaMP ($^{NS}P=0.27$) or full-band LFP ($^{NS}P=0.99$) power. Importantly, Control mice were transduced with an analogous viral construct that expresses the mCherry tag alone, and no DREADD channel. Control mice exhibited no change in power after administration of CNO, as demonstrated in both GCaMP and LFP in **Figures 3.2,3**. These baseline differences in motor activity, while unplanned, provide valuable information about how local E/I changes propagate through functional networks. In **Figures 3.4-7**, we focus on relative changes in each group from the OFF to ON state (e.g., the acute effect of enhanced inhibition, for the ↑PV group), while also noting informative consequences of the ↑PV group's baseline motor cortex hyperexcitability. The emergence of these baseline differences in CNO-naïve mice over 8 weeks after viral injection as confirmed in a separate cohort in **Figure 3.S8**. Mechanistic origins of these unexpected findings are considered in the Discussion.

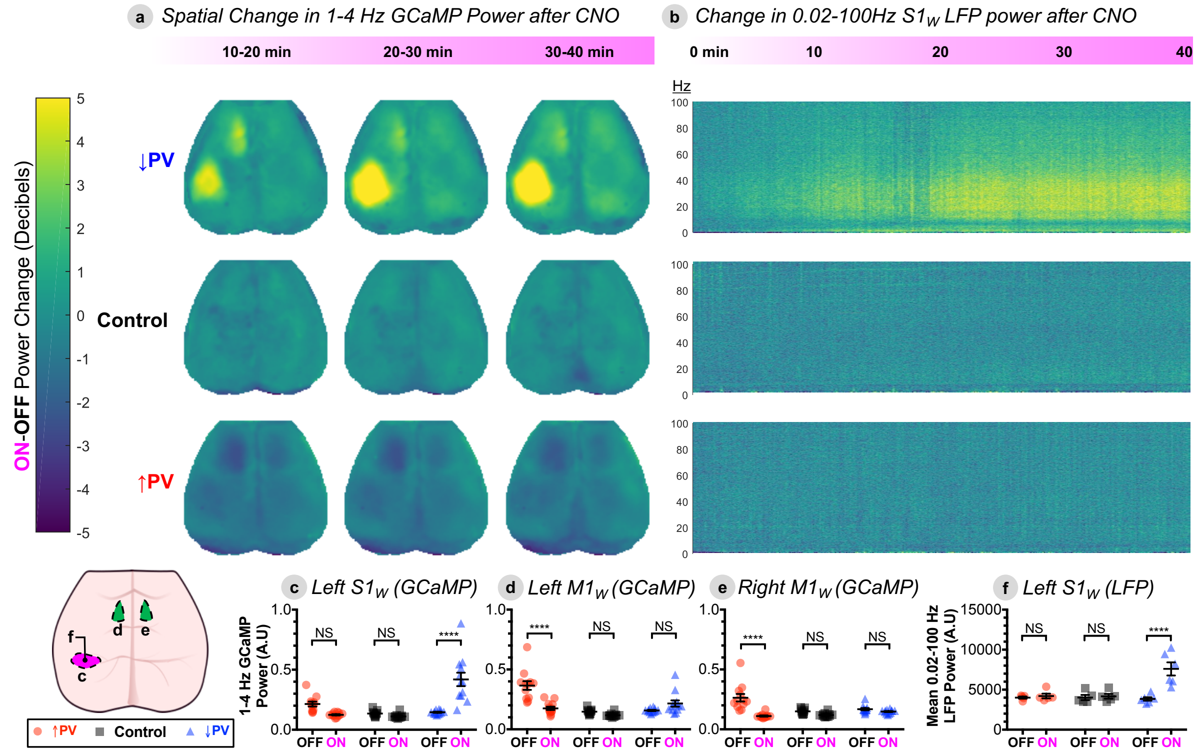

Figure 3.3. Locally disrupted $S1_W$ E/I balance bidirectionally modulates spectral power locally and in remote sensorimotor areas. (**A**), Change in power spectral density (ΔPower, in decibels) for 1-4 Hz (delta band) GCaMP activity for each pixel in the brain space for each experimental group, comparing three successive 10-minute imaging windows after

CNO delivery (ON) to a preceding 10-minute baseline OFF epoch using equation E1. Data represent group averages (↑PV n=12, ↓PV n=12, Control n=11), quantified within three different ROIs below in **C-E**. (**B**), ΔPower spectrogram in S1$_W$ LFP, on same decibel scale as **A**, with frequency on the y-axis (Hz) and time (in minutes) on the x-axis. ΔPower is computed over a continuous 40-minute ON epoch after CNO injection, compared to a preceding 10-minute OFF epoch. Data represent group averages (↑PV n=5, ↓PV n=6, Control n=5), quantified in **F.** (**C,D,E,F**) Statistical verification of trends in three ROIs from the GCaMP data – left S1$_W$ (**C**), left M1$_W$ (**D**), and right M1$_W$ (**E**) – as well as LFP data from left S1$_W$ (**F**). Power spectral density is shown in arbitrary units (A.U.). Individual data points represent individual mice, black bars designate mean ± SEM. Significance was calculated by 2-way ANOVA with Tukey's multiple comparison test for each figure panel, comparing both within and between groups. ON-OFF statistical comparisons within group are depicted within each panel, while comparisons between groups are reported in the main text. ($^{*}P < 0.05$, $^{**}P < 0.01$, $^{***}P < 0.001$, and $^{****}P < 0.0001$). See also Figure **3.S3** for ΔPower maps for infraslow (0.02-0.1 Hz) GCaMP and oxy-Hb.

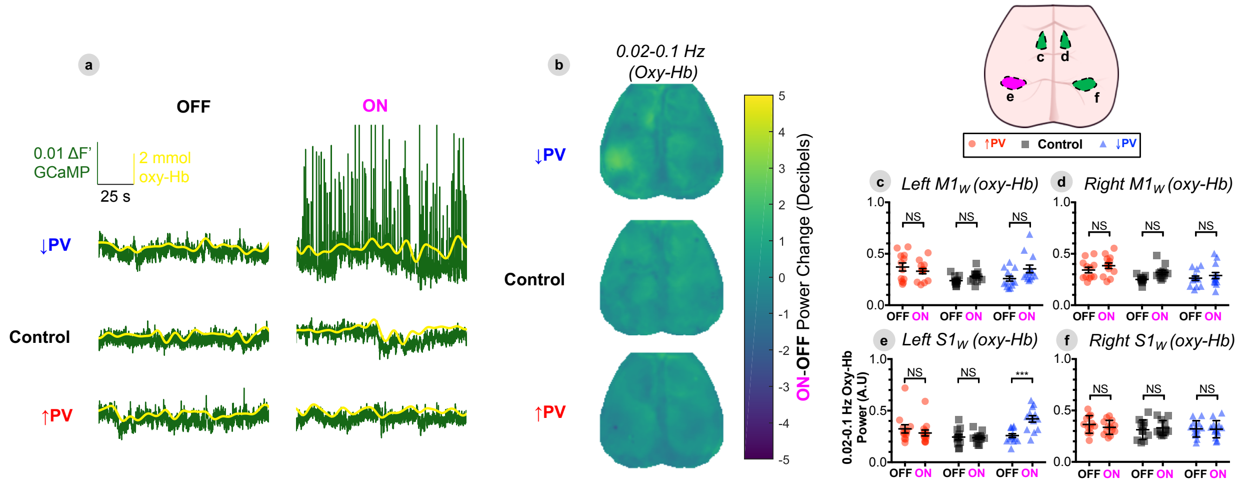

Figure 3.S3. Changes in infraslow oxy-Hemoglobin dynamics during DREADD activation. (**A**) Representative time series of GCaMP (green) and oxy-Hb (yellow) from within S1$_W$ for each virus group in the ON and OFF states. (**B**) ΔPower maps for infraslow oxy-Hb, for comparison to delta band (1-4 Hz) ΔPower shown in Figure 3.3. Changes are represented as group averages (↑PV n=12, ↓PV n=12, Control n=11). (**C-F**) Average changes in infraslow oxy-Hb power quantified for 4 different ROIs – Left M1$_W$ (**C**), Right M1$_W$ (**D**), Left S1$_W$ (**E**), Right S1$_W$ (**F**). Significance was calculated by 2-way ANOVA with Tukey's multiple comparison test for each figure panel, comparing both within and between groups. ON-OFF statistical comparisons within group are depicted within each panel, while comparisons between groups are reported in the main text. ($^{*}P < 0.05$, $^{**}P < 0.01$, $^{***}P < 0.001$, and $^{****}P < 0.0001$).

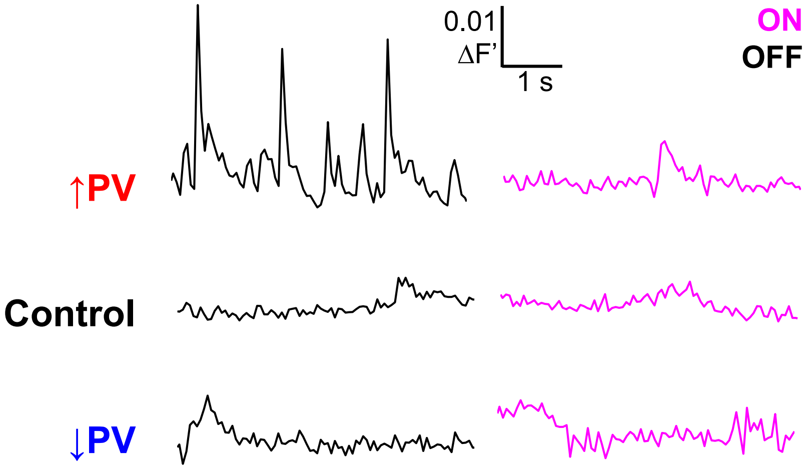

Figure 3.S4. Representative time-series of GCaMP fluorescence (ΔF') within the left $M1_W$ ROI shown for each of the three experimental groups at baseline (OFF, black) and 30 minutes after delivery of CNO (ON, magenta). ↑PV mice consistently exhibit paroxysmal bursts of activity in $M1_W$ in the OFF state, similar to those observed in $S1_W$ in ↓PV- ON mice in Figure 3.2.

Propagation of local E/I imbalance disrupts patterns of cortical resting-state functional connectivity

In order to characterize how these focal changes in excitability spread within cortical networks, we performed two complementary analyses of resting state neuroimaging data: first, mapping the zero-lag correlation structure (functional connectivity, FC) of cortical dynamics across whole time-series, and second, assessing effective connectivity by computing event-triggered average (ETA) responses to high amplitude events in $S1_W$. For stationary, normally-distributed activity, these two approaches converge on typical correlation patterns for mouse connectivity: strong homotopic connectivity between left and right cortices (Wright et al., 2017b). However, these approaches offer complementary perspectives in the setting of paroxysmal bursting events in the ↑PV-OFF and ↓PV-ON conditions.

In order to identify regions undergoing FC changes, we first computed the Fisher z-transformed Pearson correlation, z(r), between time-series of every pair of pixels in the cortex and constructed group-averaged FC matrices in the ON and OFF conditions; ON-OFF ΔFC matrices were computed by subtraction (**Figure 3.S5A**). OFF-state FC matrices for Control and ↓PV mice were qualitatively similar, while ↑PV mice exhibited baseline differences from the other two groups, with foci of altered connectivity particularly in S1 and M1 cortices. ON-OFF ΔFC matrices demonstrated no change in Control mice, while ↓PV and ↑PV mice exhibited ON-OFF connectivity changes primarily in somatosensory and motor regions. The localization of FC changes to this network of regions was verified by principal component analysis (**Figure 3.S5B**) performed on ΔFC matrices: ~80% of the variance for both ↓PV and ↑PV ON-OFF ΔFC matrices was captured by the first component, which prominently features $S1_W$ and $M1_W$. In contrast, the first component of ON-OFF ΔFC matrices in Control mice explained less than 40% of the variance and did not have a distinctive topography. To visualize FC changes from the perspective of seed regions within the whisker sensorimotor network, we computed FC maps, comparing each pixel's time-series to the average time-series within empirically derived seed ROIs (see Methods) for whisker sensory and motor cortices (**Figure 3.S7**). We then computed ON-OFF ΔFC maps for GCaMP by subtraction of data in Figure 3.S7 (**Figure 3.4A-D**) and statistically verified key FC changes (**Figure 3.4E-G**) by 2-way ANOVA with Tukey's multiple comparison test, focusing on homotopic (interhemispheric) FC for $S1_W$ and $M1_W$, as well as intrahemispheric $S1_W$:$M1_W$ sensorimotor FC. To facilitate comparison with BOLD FC data, we conducted parallel FC analyses of the infraslow oxy-Hb optical intrinsic signal (ON-OFF ∆FC maps in **Figure 3.S6** mirror Figure 3.4, original ON and OFF maps shown in **Figure 3.S7**).

At baseline, ↑PV-OFF mice exhibited heightened three-node synchrony between left $S1_W$ and right/left $M1_W$ (**Figure 3.S7A,C,D**). Specifically, ↑PV-OFF mice had stronger baseline intrahemispheric $S1_W$:$M1_W$ correlation than littermates in other groups ($^{****}P<0.0001$ vs. ↓PV-OFF or Control-OFF, **Figure 3.4F**), as well as stronger $M1_W$ homotopic synchrony ($^{****}P<0.0001$ vs. either group, **Figure 3.4G**). These differences reversed upon chemogenetic activation of $S1_W$ PV-INs (**Figure 3.4A,C,D**): we observed significant ON-OFF reductions in $S1_W$:$M1_W$ correlation ($^{**}P<0.0014$) down to Control levels ($^{NS}P=0.17$ vs. Control-ON, **3.4F**). Likewise, ON-state motor homotopic FC was significantly reduced (ON-OFF $^{*}P=0.02$, **3.4G**), though still elevated compared to Control-ON $M1_W$ homotopic FC ($^{***}P<0.0002$). Interestingly, while baseline hyperexcitability propagated to left and right motor cortices, it was not transmitted interhemispherically from $S1_W$ (**Figure 3.4E**), the area of viral transduction. Indeed, we observed lower baseline ↑PV-OFF $S1_W$ homotopic connectivity ($^{**}P<0.006$ vs. Control-OFF, $^{****}P<0.0001$ vs. ↓PV-OFF). Activating DREADDs normalized these differences, increasing ↑PV-ON $S1_W$ homotopic FC to Control levels ($^{NS}P=0.82$ vs. Control-ON). Indeed, baseline hyper-connectivity between left $S1_W$ and right/left $M1_W$ came at the expense of weakened connectivity with all of the rest of the cortex, forming conspicuous regions of negative correlation for seeds placed outside of these three nodes (e.g. weakened OFF-state FC with right $S1_W$, **Figure 3.S7B**).

Activating S1$_{W}$ PV-INs reversed these baseline differences. Thus, seeds in these three regions exhibited qualitatively increased FC with the rest of the cortex (orange on ∆FC maps, **Figure 3.4**).

To confirm that differences in ↑PV mice were caused by expression of chemogenetic constructs injected into S1$_{W}$ 8 weeks prior, we injected DREADDs in a new cohort (↑PV *n*=5, ↓PV *n*=6, Control *n*=6) and installed cranial windows immediately afterwards so that we could monitor FC during the 8-week recovery period after viral injection (**Figure 3.S8**). Mice were naïve to CNO throughout this experiment. All three groups exhibited similar patterns of connectivity at week 0 (immediately after injection) that were consistently maintained over 4 weeks of imaging. However, the ↑PV mice diverged after week 6, exhibiting weaker whisker homotopic FC and stronger intrahemispheric S1$_{W}$:M1$_{W}$ connectivity. FC changes were concurrent with the emergence of high amplitude bursting activity in M1$_{W}$ of ↑PV mice (example in **Figure 3.S4**), visible as a rightward-shift in histograms of GCaMP intensity in M1$_{W}$ beginning at week 6 (**Figure 3.S8D**). Owing to limited sample size, this experiment was not sufficiently powered to match the statistically significant baseline FC differences shown with *n*=12 beyond the 8-week time point in **Figure 3.4F** and **3.4G**.

↓PV-OFF mice did not exhibit baseline FC differences and were indistinguishable from Control-OFF mice on S1$_{W}$ homotopic FC (^{NS}P=0.74), M1$_{W}$ homotopic FC (^{NS}P=0.97) and S1$_{W}$:M1$_{W}$ FC (^{NS}P=0.998). However, chemogenetic inhibition of PV-INs dramatically increased $S1_W$:$M1_W$ FC (ON-OFF $^{****}P<0.0001$) while simultaneously weakening $S1_W$ homotopic FC (ON-OFF $^{****}P<0.0001$) and $M1_W$ homotopic FC (ON-OFF $^{**}P=0.0013$).

Control mice did not exhibit any significant changes in FC after delivery of CNO (ΔFC matrices in **Figure 3.S5** and ΔFC maps in **Figure 3.4**). In addition, effects in delta-band GCaMP FC (**Figure 3.4**) for all three groups were qualitatively mirrored in oxy-Hb FC (**Figure 3.S6**). We have previously shown that connectivity of the hemoglobin optical intrinsic signal exhibits strong spatial similarity to GCaMP FC (Wright et al., 2017b). Indeed hemoglobin FC changes in Figure 3.S6 exhibit similar topography to delta band GCaMP maps, although with more spatial noise (and weakened statistical strength), as expected for infraslow hemodynamics.

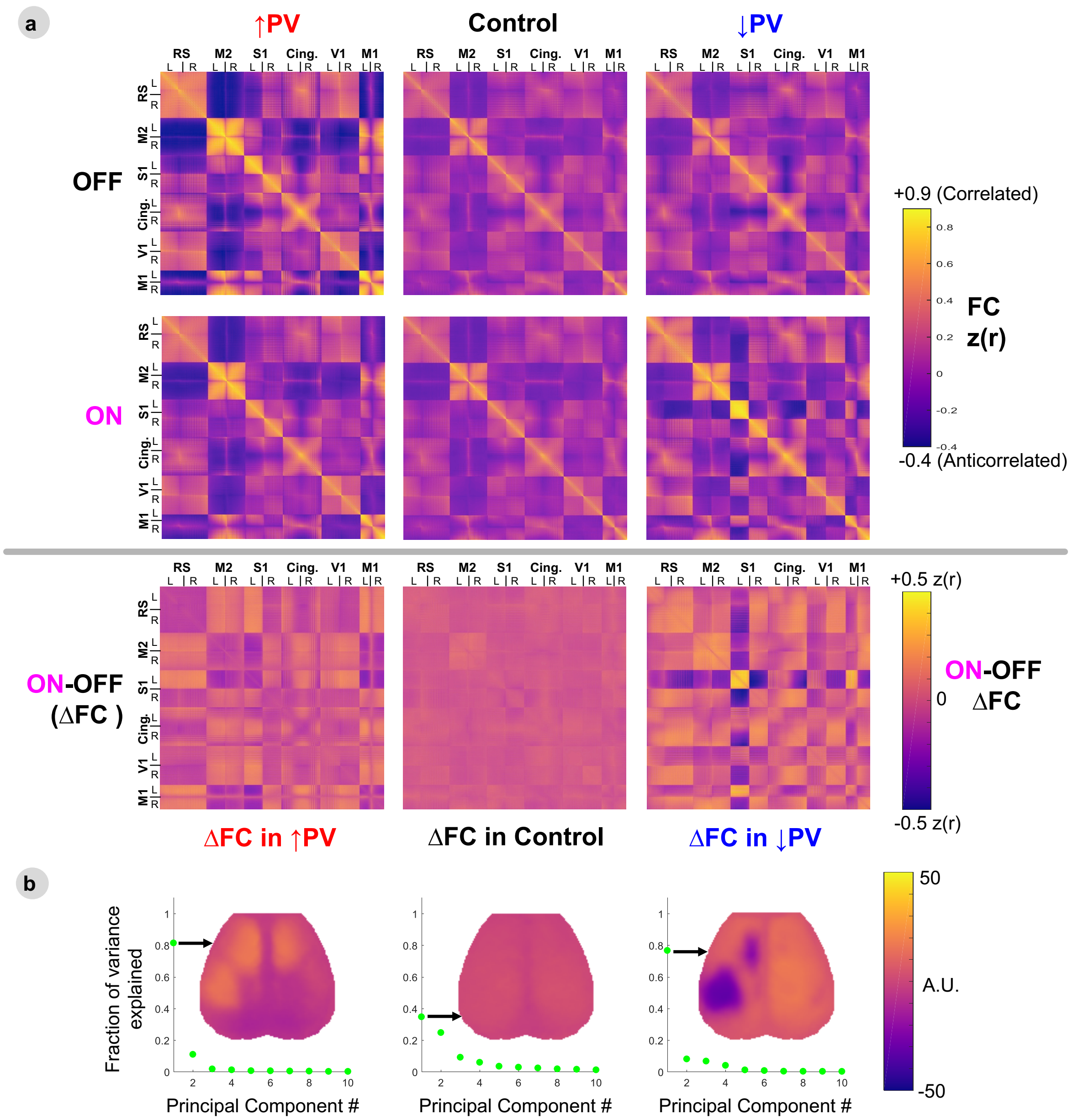

Figure 3.S5. Correlation changes are specific to the whisker sensorimotor network. (**A**) Delta band GCaMP FC and ON-OFF ΔFC matrices. Matrices were constructed by comparing the Fisher z-transformed Pearson correlation *r* between each pair of pixels in the brain space at baseline (OFF, black) and 30 minutes after delivery of CNO (ON). Pixels in ΔFC matrices were sorted into large functional clusters (RS = retrosplenial, M2 = secondary motor, S1 = primary somatosensory, Cing.= cingulate, V1= visual, M1 = primary motor). Matrices were calculated from 10 minutes of ON and 10 minutes of OFF data for each mouse, and then averaged within group (↑PV *n*=12, *n*=12, Control *n*=11). Note baseline differences in sensory and motor connectivity in the ↑PV group compared to ↓PV and Control. ON-OFF changes were observed to be especially prominent in sensory and motor pixels in both ↑PV and ↓PV mice, while Control mice exhibited no

change. (**B**) Principal component analysis of ΔFC matrices. The first principal component (PC) of each matrix is plotted as an inset map. For both ↑PV and ↓PV, the first PC explained ~80% of the variance in the ΔFC matrix and exhibited a topography similar to right $S1_W$ seeded ΔFC maps in Figure 3.4B. For Control mice, the first PC explains less than 40% of the ON-OFF ΔFC matrix and lacks distinctive topography.

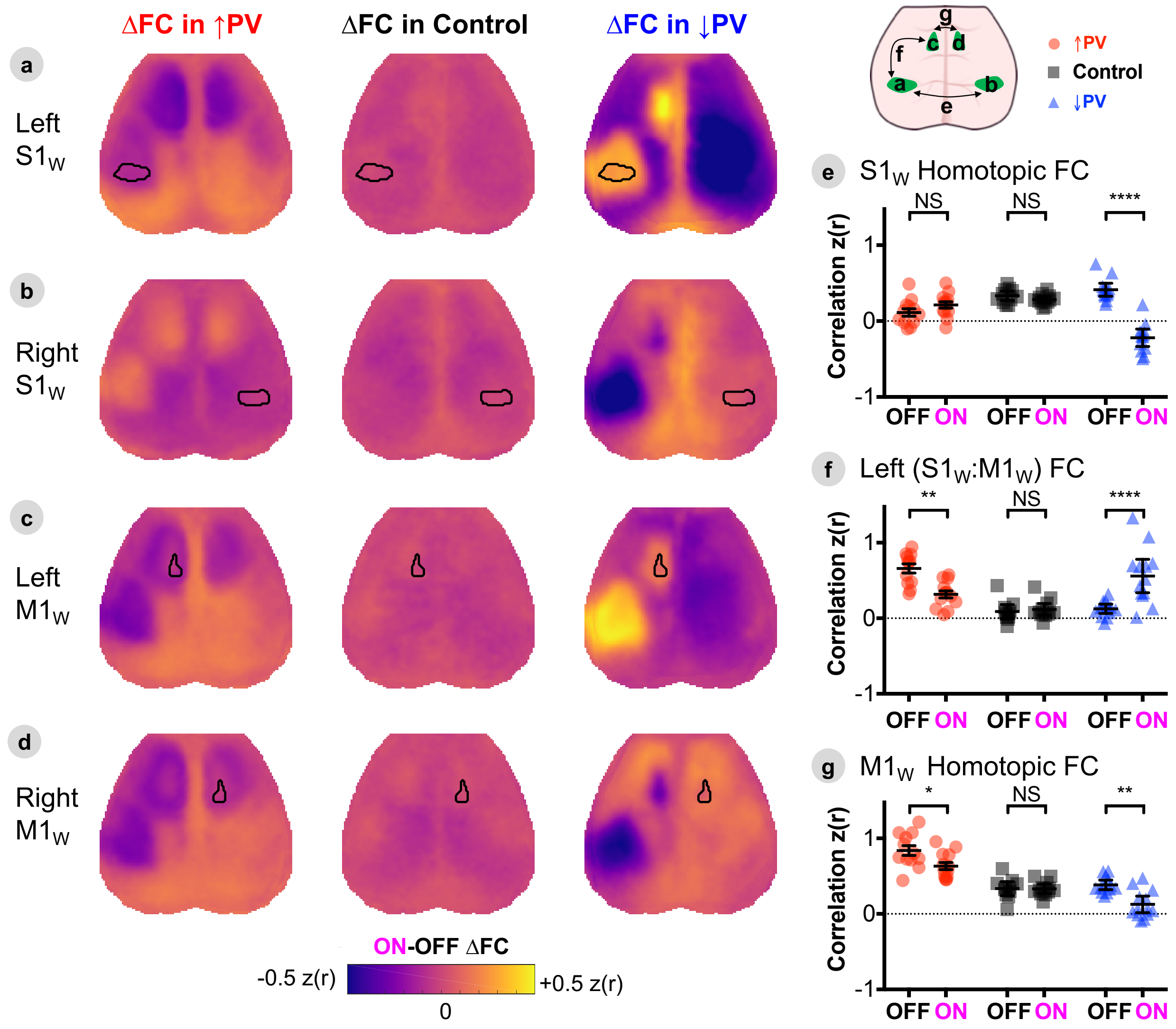

Figure 3.4. Propagation of local E/I imbalance disrupts patterns of cortical resting-state functional connectivity. **A-D,** ON-OFF ΔFC maps computed by array subtraction of ON and OFF maps shown in Figure 3.S7, for seeds placed in left $S1_W$ (**A**), right $S1_W$ (**B**), left $M1_W$ (**C**), and right $M1_W$ (**D**). Maps are represented as group averages (↑PV *n*=12, ↓PV *n*=12, Control *n*=11). (**E-G**), Statistical verification of changes in homotopic $S1_W$ connectivity (**E**), left $S1_W$:$M1_W$ sensorimotor connectivity (**F**), and homotopic $M1_W$ connectivity (**G**). Individual data points represent individual mice, black bars designate

mean ± SEM, with significance calculated by 2-way ANOVA with Tukey's multiple comparison test ($^{*}P < 0.05$, $^{**}P < 0.01$, $^{***}P < 0.001$, and $^{****}P < 0.0001$). See also companion Supplemental Figures 3.S5-7.

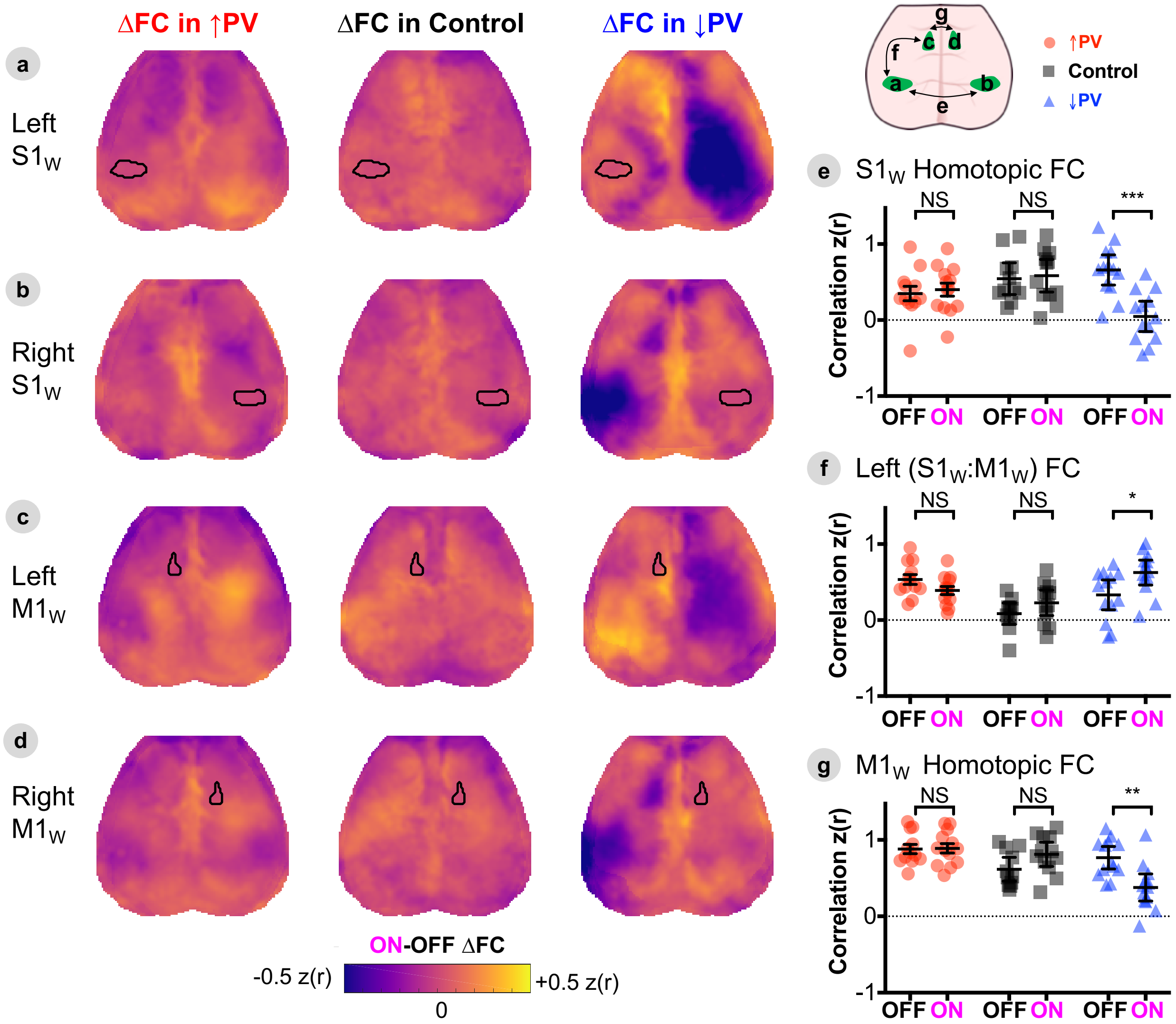

Figure 3.S6. ON-OFF FC changes for infraslow oxy-Hb optical intrinsic signal. ON-OFF maps are shown for multiple seed ROIs: left S1$_{W}$ (**A**), right S1$_{W}$ (**B**), left M1$_{W}$ (**C**), and right M1$_{W}$ (**D**). Maps are based on 10 minutes of ON and 10 minutes of OFF data from each mouse, averaged within group (↑PV n=12, ↓PV n=12, Control n=11). Data were statistically verified (**E-G**) by 2-way ANOVA with Tukey's multiple comparison test. Changes qualitatively mirror those found in delta band GCaMP activity in Figure 3.4.

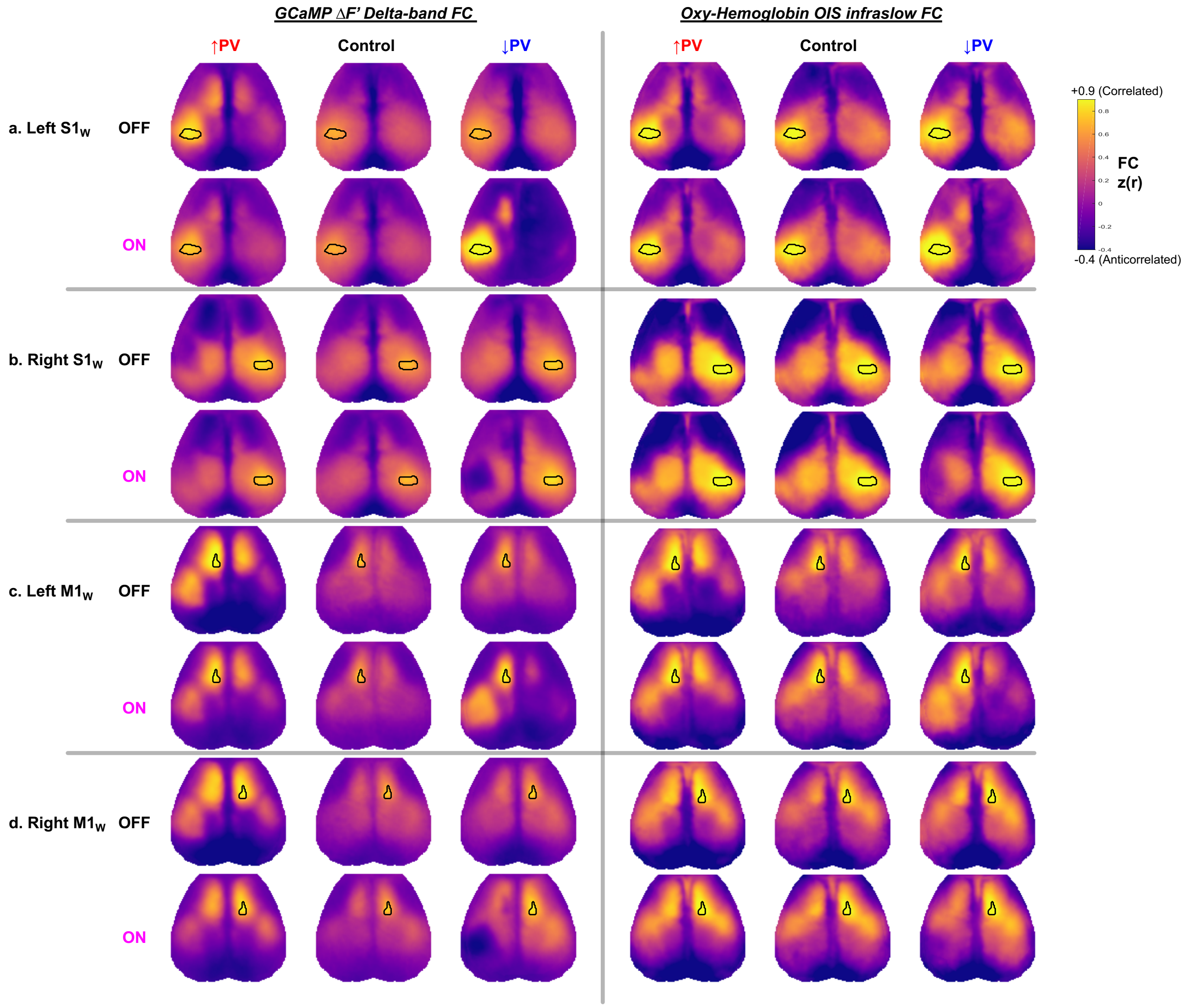
GCaMP ΔF' Delta-band FC
Oxy-Hemoglobin OIS infraslow FC
↑PV
Control
↓PV
↑PV
Control
↓PV
a. Left S1$_W$
OFF
ON
b. Right S1$_W$
OFF
ON
c. Left M1$_W$
OFF
ON
d. Right M1$_W$
OFF
ON
+0.9 (Correlated)
0.8
0.6
0.4
0.2
0
-0.2
-0.4
FC
z(r)
-0.4 (Anticorrelated)

Figure 3.S7. ON and OFF FC maps used to calculate ΔFC maps in Figure 3.4 (delta band GCaMP ΔFC maps) and Figure 3.S5 (Infraslow hemoglobin OIS ΔFC maps), comparing correlation of dynamics in each pixel in the brain with that of a seed ROI. (**A-D**), ON and OFF maps from seeds corresponding to A-D in Figures 3.4 and 3.S5: left S1$_W$ (**A**), right S1$_W$ (**B**), left M1$_W$ (**C**), and right M1$_W$ (**D**). Maps are based on 10 minutes of ON and 10 minutes of OFF data from each mouse, averaged within group (↑PV *n*=12, ↓PV *n*=12, Control *n*=11). Note baseline (OFF-state) FC topography differences in sensorimotor connectivity in the ↑PV group compared to ↓PV and Control.

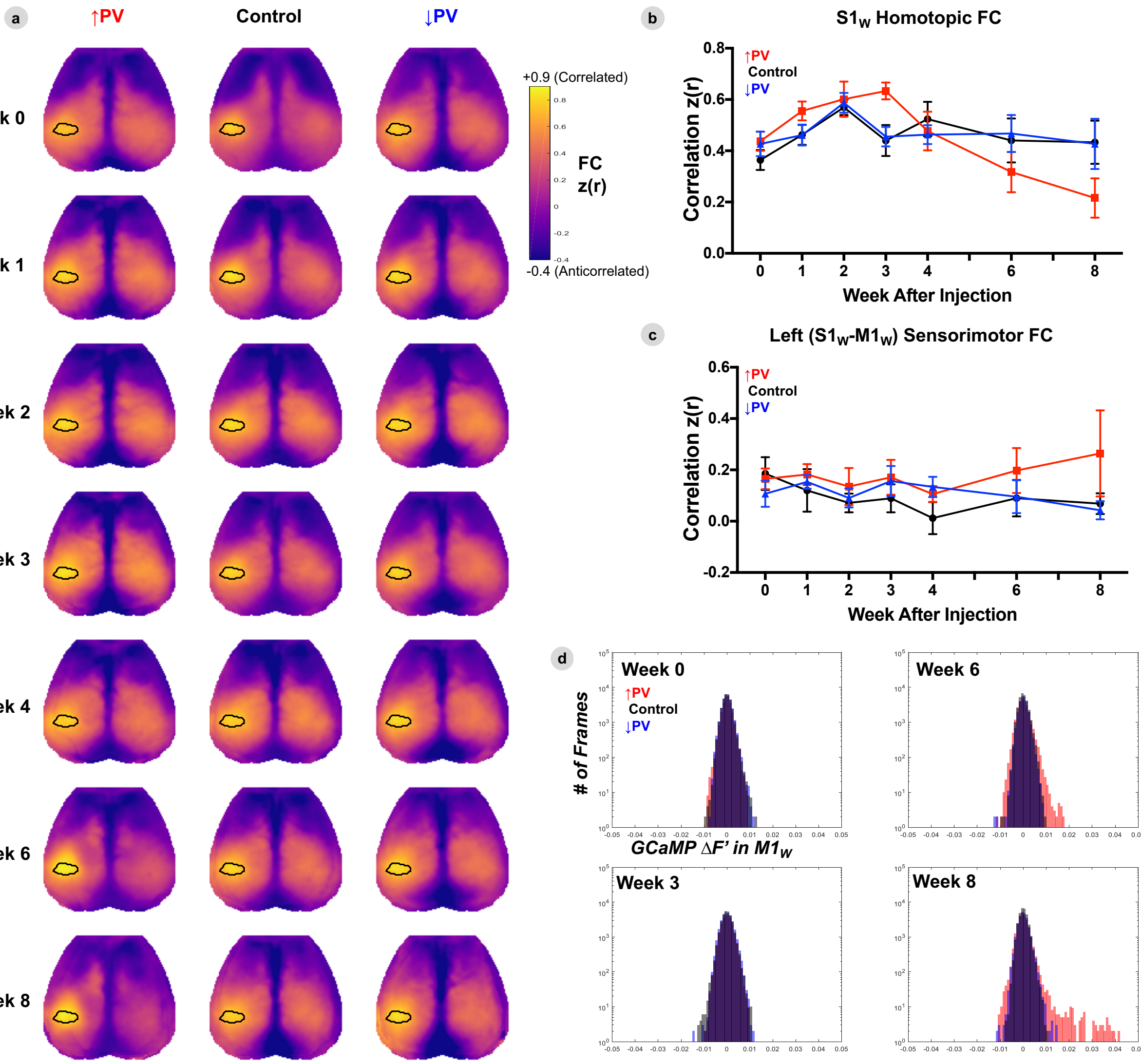

Figure 3.S8. FC patterns change in response to local chemogenetic constructs. A separate cohort of mice were windowed immediately after injection to permit longitudinal imaging during the 8-week induction period. Week 0 data was collected the day after surgery. Progressive changes in group average FC maps are shown for a seed placed in left $S1_W$ (**A**). Changes in whisker homotopic FC (**B**) and left $S1_W$:$M1_W$ sensorimotor FC (**C**) are shown to the right. Data represent group mean ± SEM (↑PV *n*=5, ↓PV *n*=6, Control *n*=6). Weakened whisker homotopic FC and strengthened sensorimotor FC can be qualitative appreciated in the ↑PV group by week 6, however data was not sufficiently powered for statistical testing due to limited sample sizes. (**D**) Histograms of GCaMP intensity within $M1_W$ pooling GCaMP imaging frames between mice within each group. Changes in FC emerged as a consequence of increased incidence of high amplitude bursting events in $M1_W$ in ↑PV mice beginning at week 6.

ON-OFF Changes in $S1_w$ event-triggered average activity spread intrahemispherically to $M1_W$ but not to the contralateral hemisphere

In order to disambiguate how the additive signal of hyperexcitability bursts impacts functional connectivity (Duff et al., 2018), we examined effective connectivity at the event level. All local maxima in $S1_W$ GCaMP time-series for each individual mouse were sorted by amplitude (**Figure 3.S9**). Event-triggered averages (ETAs, as shown in **Figure 3.5A**) were computed within mouse by averaging local maxima (thresholded at >90th percentile peaks) at baseline (OFF) and 30 minutes after delivery of CNO (ON). Group averaged cortical dynamics surrounding $S1_W$ maxima are shown for each condition in **Figure 3.5B** (as maps) and **3.S9A** (as average time series) with $S1_W$ peaks centered at 0 seconds. Differences in regional GCaMP peak amplitudes, centered on $S1_W$ peaks, were statistically compared between ipsi- and contralateral $S1_W$ and $M1_W$ within group in **Figure 3.5C-E**, with significance determined by 2-way ANOVA with Tukey's multiple comparison test. To determine whether the additive signal of high amplitude $S1_W$ activity explains FC changes (**Figure 3.S9C**), we compared time series correlation values with all $S1_W$ peaks included (100%), and after removing peaks (and surrounding time points) above a progressively decreasing percentile value before re-computing correlation.

ETA in Control mice revealed that local maxima in $S1_W$ occur synchronously with activation of contralateral $S1_W$ and bilateral motor cortices (with no difference between ON and OFF states, **Figure 3.5B,D**), consistent with the normal correlation structure of the barrel cortex (**Figure 3.S7A,B**). The distribution of amplitudes of local maxima in the

ON and OFF state were very similar (**Figure 3.S9B**). Removing high amplitude peaks from the time series did not introduce ON-OFF correlation differences (**Figure 3.S9C**).

As in Control mice, ↓PV-OFF mice exhibited bilaterally symmetric cortical activation patterns surrounding S1$_{W}$ maxima (**Figure 3.5C**). However, in the ON state, local peaks in S1$_{W}$ were significantly higher in amplitude ($^{****}P<0.0001$ vs. ↓PV-OFF, **Figures 3.5B,C**; **3.S9A**), reflecting the high amplitude bursts seen in **Figure 3.2**. Closer examination of the distribution of S1$_{W}$ peaks in **Figure 3.S9B** demonstrates that nearly all ON maxima were higher in amplitude than OFF maxima. ON-OFF changes in S1$_{W}$ simultaneously increased ipsilateral M1$_{W}$ activation ($^{**}P=0.010$, **5C**) while non-significantly reducing contralateral activity in S1$_{W}$ ($^{NS}P=0.14$) and M1$_{W}$ ($^{NS}P=0.63$). This unilateral high amplitude activity directly caused ON-OFF differences in motor homotopic and sensorimotor correlation (**Figure 3.S9C**), with differences returning to non-significant levels after the top deciles of peak activity were removed from time series. Whisker homotopic FC, however, remained significantly different between ON and OFF at all scales of activity, even after excising time points associated with the top 90% amplitude local peaks from time series (data not shown). We also note that high amplitude bursts in S1$_{W}$ were, on average, temporally flanked by local decreases in S1$_{W}$ activity (**Figure 3.5B, 3.S9A**).

In ↑PV mice, ETA highlighted important baseline (OFF) differences (**Figures 3.5B,E**; **3.S9A**): local peaks in left S1$_{W}$ were significantly higher in amplitude than those on the right side ($^{**}P<0.0022$), and coincided with high amplitude activity bilaterally in the motor cortices. When PV-INs were chemogenetically activated (ON state), peak amplitude was non-significantly reduced in $\mathrm{S1_W}$ (^{NS}P=0.1756, **Figure 3.5E**), although the distribution of $\mathrm{S1_W}$ activity shifted to lower amplitudes (**Figure 3.S9B**). However, chemogenetic activation of $\mathrm{S1_W}$ PV-INs significantly reduced activity in ipsilateral $\mathrm{M1_W}$ during $\mathrm{S1_W}$ peaks ($^{**}P$=0.0088, **Figure 3.5E**). ETA amplitude was not significantly different in contralateral $\mathrm{S1_W}$ (^{NS}P=0.91) or $\mathrm{M1_W}$ (^{NS}P=0.069). $\mathrm{S1_W}$ homotopic correlation was similar between ON-OFF at all scales of activity (**Figure 3.S9C**). ON-OFF motor homotopic FC was reduced and straddled significance at all scales of activity, suggesting that correlation changes were not driven solely by high amplitude bursts in $\mathrm{S1_W}$. Likewise, sensorimotor FC remained significantly weaker even after removing the top 50% high amplitude bursts, indicating that correlation strength was altered during both high and low amplitude activity in $\mathrm{S1_W}$.

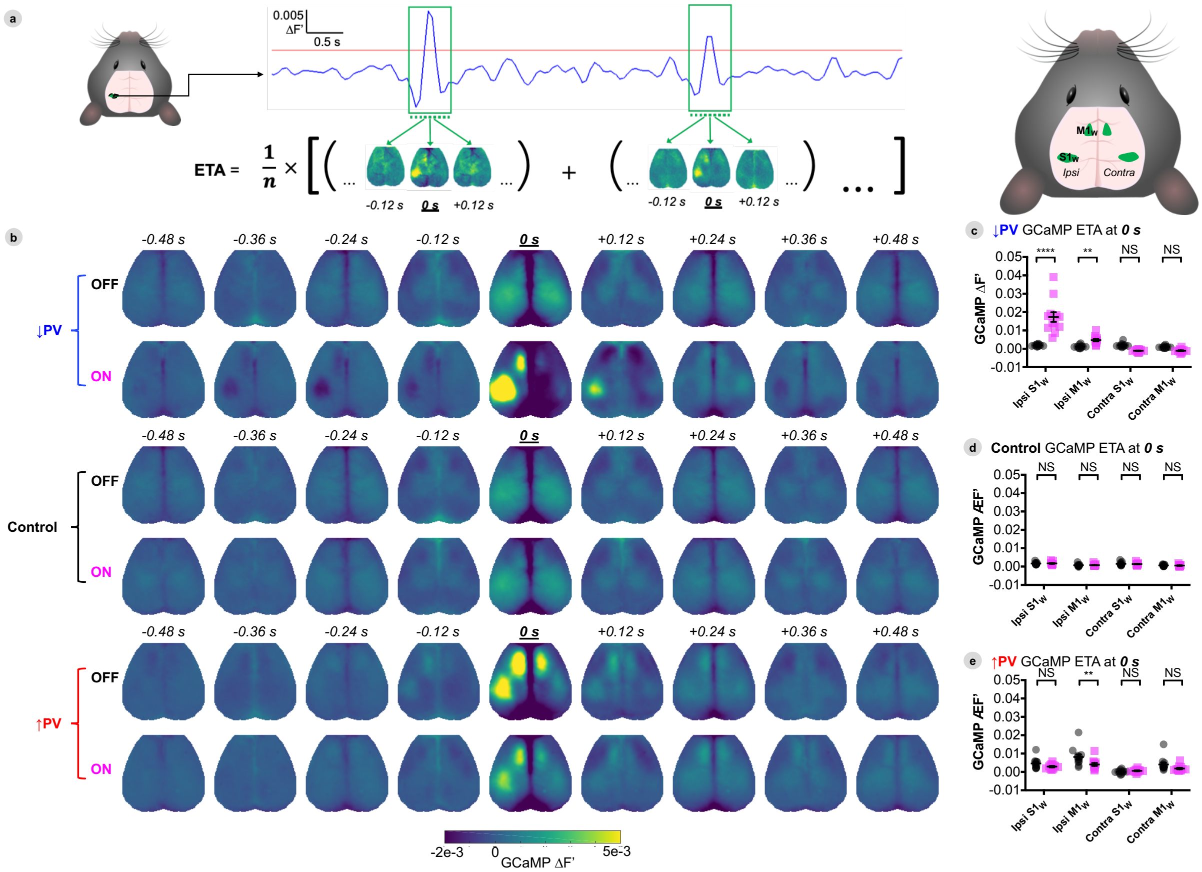

Figure 3.5. ON-OFF Changes in S1$_W$ event-triggered average activity spread intrahemispherically to M1$_W$ but not to the contralateral hemisphere. (**A**) Illustration of event-triggered average (ETA) computation. Frames surrounding local peaks above a given threshold (depicted as red line) in the 1-4 Hz GCaMP time series taken from the S1$_W$ region were flagged for averaging (run-specific, percentile-based thresholds were computed as described in Methods). Cortex-wide maps corresponding to the flagged frames were averaged to generate a movie of cortical dynamics preceding and succeeding high-amplitude bursts in S1$_W$. (**B**) Group-averaged GCaMP dynamics surrounding the top 10% of local up-peaks in S1$_W$ (centered at 0 s), with DREADDs ON or OFF. (**C-E**) Average GCaMP fluorescence (ΔF') within four different ROIs at t=0 s during S1$_W$ peaks for each group. Individual data points represent individual mice, black bars designate mean ± SEM, with significance calculated by 2-way ANOVA with Tukey's multiple comparison test ($^{*}P < 0.05$, $^{**}P < 0.01$, $^{***}P < 0.001$, and $^{****}P < 0.0001$). Data are shown at baseline (OFF, black) and 30 minutes after delivery of CNO (ON, magenta). See also Figure 3.S9 to see amplitude distribution of peaks and how they impact FC.

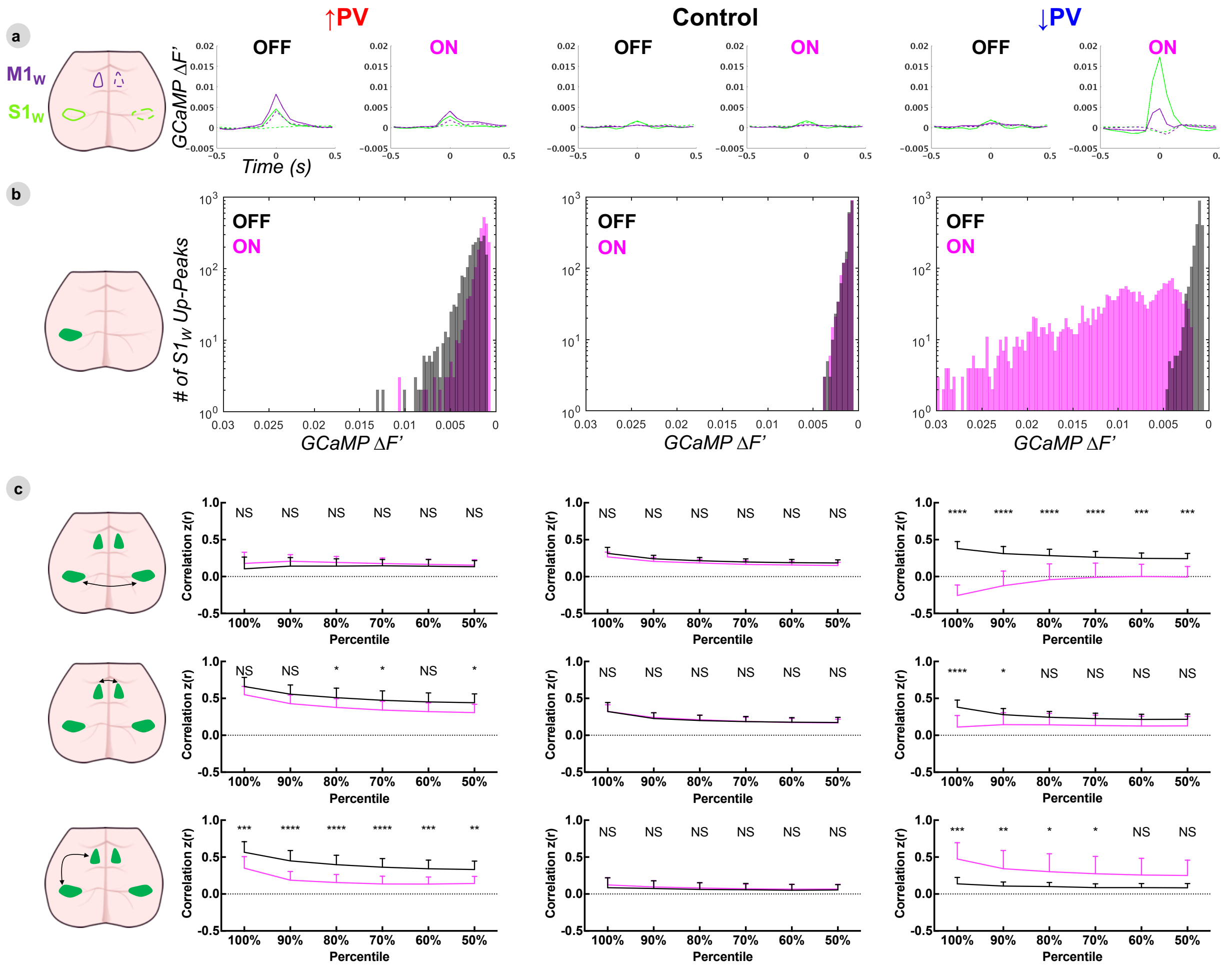

Figure 3.S9. Dependence of delta band GCaMP FC changes on amplitude of S1$_W$ activity. (**A**) Event-triggered average time series during top 10% of S1$_W$ peaks shown in Figure 3.5A. (**B**) Histograms plotting the amplitude distribution of all local peaks in S1$_W$ GCaMP time series, pooled between all mice in each group. Note x-axis is inverted with high amplitude activity on the left to match the orientation of **C**. (**C**) Pearson correlation values between different ROIs, as a function of decreasing proportion of local peaks retained. Percentiles indicate the proportion of peak amplitudes (shown in **B**) retained for FC computation (see Methods). In all conditions, trends plateaued after 50% of local peaks were excluded, plateaued data beyond the 50th percentile are not shown. All data are represented as group mean ± SD (↑PV *n*=12, ↓PV *n*=12, Control *n*=11), and differences were statistically verified by 2-way ANOVA with Sidak's multiple comparison test.

PV-INs modulate S1$_W$ excitability to ascending contralateral sensory inputs, but not ipsilateral inputs

To assess how local changes in E/I balance affect cortical responses to ascending thalamocortical sensory input, we recorded GCaMP activity in awake mice during unilateral stimulation of their mystacial whiskers using computer-triggered air-puffs (**Figure 3.6**). Stimulation was presented in 20 second blocks (5 s rest, 5 air-puffs at 1 Hz, 10 s rest). To assess the pharmacokinetics of CNO, right whisker stimulation was performed at baseline, 10 minutes, 30 minutes, 1 hour, 2 hours, 4 hours, and 12 hours after CNO injection. Left whisker stimulation was collected in a separate session at baseline and 30 minutes after CNO injection. OFF refers to the baseline condition before CNO; ON refers to the time point 30 minutes after injection for both groups. Cortical dynamics were averaged to produce maps of peak evoked response (**Figure 3.6A**) as well as histograms of peak response magnitude within left and right S1$_W$ ROIs (**Figure 3.6C,E**). Differences in response magnitude within and between groups were compared by 2-way ANOVA with Tukey's multiple comparison test (↑PV *n*=6, ↓PV *n*=6, Control *n*=5). Differences within group over time (**3.6D**) were compared by 2-way ANOVA with Dunnett's multiple comparison test.

Right whisker stimulation elicited responses primarily in left S1$_W$, and to a lesser extent, left M1$_W$ and the right cortex. OFF-state evoked responses in left S1$_W$ were similar between all groups ($^{NS}P>0.99$ for all comparisons). In the ON state, evoked responses were unchanged in ↑PV (Left $^{NS}P=0.28$, Right $^{NS}P=0.71$) and Control mice (Left $^{NS}P=0.98$, Right $^{NS}P>0.99$). ↓PV mice exhibited ON-OFF differences only in left S1$_W$ (Left

$^{****}P<0.0001$, Right $^{NS}P>0.99$), which peaked between 30-60 minutes and returned to baseline levels by 4 hours after injection. Interestingly, ↓PV mice did not exhibit increased activity in ipsilateral M1$_{W}$ during whisker stimulation (data not shown, $^{NS}P=0.49$), though they did during the resting state (**Figure 3.5B,C**). Evoked responses to left whisker stimulation were primarily found in right S1$_{W}$, and were unchanged between the OFF and ON states for all three groups in both left and right S1$_{W}$.

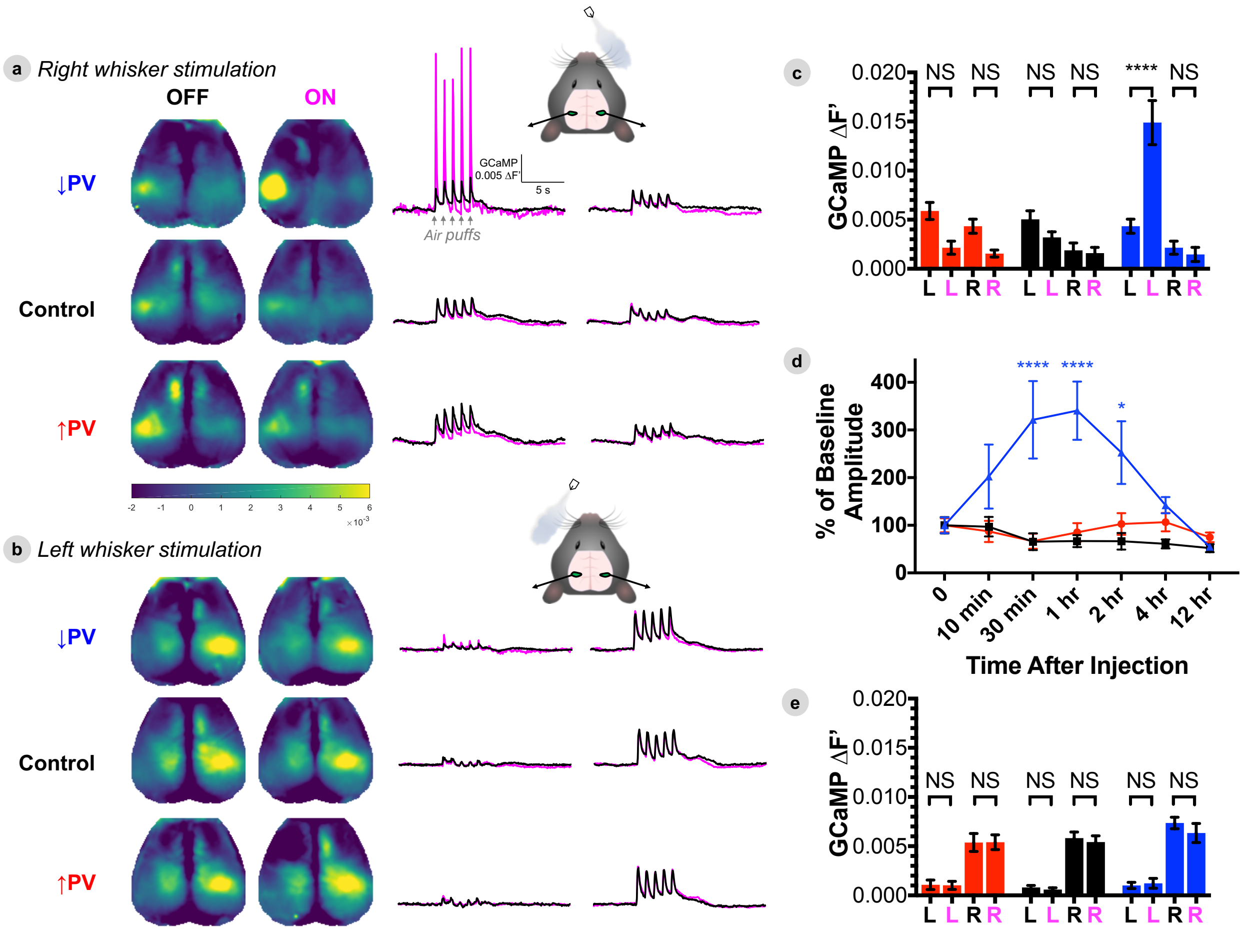

Figure 3.6. PV-INs modulate S1$_{W}$ excitability to ascending contralateral sensory inputs, but not ipsilateral inputs. (**A-B**) Group averaged evoked responses to stimulation of the right whiskers (**A**) and left whiskers (**B**) (↑PV *n*=6, ↓PV *n*=6, Control *n*=5). Responses are presented as maps of peak GCaMP fluorescence (ΔF') during stimulation, and average stimulation block time series for left and right S1$_{W}$ ROIs. (**C,E**) Average GCaMP fluorescence within left (L) and right (R) S1$_{W}$ ROIs during right (**C**) and left (**E**) whisker stimulation, with data represented as mean ± SEM, and comparisons by 2-way ANOVA

with Tukey's multiple comparison test. (**D**) Time course of CNO effect on right whisker stimulation evoked response, normalized against baseline amplitude, with comparison by 2-way ANOVA with Dunnett's multiple comparison test. Data are shown at baseline (OFF, black) and 30 minutes after delivery of CNO (ON, magenta).

3.4 Discussion

We investigated whether focal perturbation of inhibition/excitability can causally disrupt large-scale cortical network dynamics. To this end, we delivered AAV8 viral DREADD constructs to the left whisker barrel somatosensory cortex ($S1_W$) in three groups of clonal *PV-Cre;Thy1-GCaMP6f* mice. With this approach, we achieved spatial, temporal, and cell-type specific control over parvalbumin inhibitory interneurons in $S1_W$, while also enabling wide-field optical imaging of pyramidal neuron calcium dynamics. Our principal observations may be summarized as follows: (1) Focal chemogenetic manipulation of PV-INs induced both local changes in activity patterns and excitability as well as remote effects along intra- and interhemispheric connections; (2) Disturbances in activity in somatosensory and motor cortices differed in their tendency to spread interhemispherically; (3) FC networks exhibited plasticity in response to chronic expression of hM3Dq (↑PV) chemogenetic constructs in PV-INs. To the best of our knowledge, this represents the first study to mechanistically examine how focal changes in inhibition causally influence brain-wide network dynamics and FC. These results offer important insights that build on prior work described below.

Local spread of E/I imbalance

GABAergic interneurons are known to regulate local E/I balance, maintaining brain dynamics in a metastable equilibrium in which inhibition rapidly scales to counterbalance fluctuating excitatory activity (Moore et al., 2018). Optogenetic inhibition of PV-INs has been shown to disrupt E/I balance, leading to hyperexcitability, prolonged cortical up-states, and increased amplitude and spatial spread of stimulus-evoked activity (Yang et al., 2017). It has been suggested that this highly synchronized activity resembles a mild focal seizure (Chen et al., 2017), similar to the paroxysmal hyperexcitability we observed in $S1_W$ (**Figure 3.2**). These effects exhibit surprising lateral spread: the medial-lateral diameter of $S1_W$ power changes (3.1 mm, depicted in **Figure 3.3A**) was nearly twice as wide as the average cross-sectional area expressing DREADDs on histology (**Figure 3.1B**), extending into adjacent regions of S1 without DREADD expression. Although dimensional comparisons between *in vivo* neuroimaging and fixed-tissue histology are challenging, this observation is corroborated by a prior report that focal activation of PV-INs in a 200 μm area affects activity in pyramidal neurons 2 mm away (Zucca et al., 2017). Similarly, a recent report has shown that a focal seizure in a 2-3 mm region can cause hemisphere-wide changes in PV-IN activity, and that pharmacologic $GABA_A$ receptor blockade can contiguously widen the seizure focus or extend it remotely to secondary foci (Liou et al., 2018). In addition, local seizures in V1 have been shown to propagate to distal portions of V1 that share the same retinotopic preference (Rossi et al., 2017). Contiguous spread of E/I disturbances may be mediated by dense connectivity of PV-INs with nearby pyramidal neurons, as well as spatial buffering between PV-INs that are laterally coupled by gap junctions. While these properties may explain why activity changes spread locally, different neural circuits may convey long distance propagation beyond the immediate reach of local inhibition.

Structural circuits underlying remote spread of activity

We have previously reported that optogenetic stimulation of excitatory neurons elicits effective connectivity along whisker sensorimotor connections as well as homotopic spread between motor cortices, but weak homotopic spread between whisker sensory cortices, in line with cortical structural connectivity (Bauer et al., 2018). Here, we extend those findings by demonstrating that disrupting inhibitory circuits can elicit similar patterns of activity spread, but in the context of intrinsic resting state dynamics, rather than being externally driven (as with optogenetics). Thus, the effective connectivity rules we have previously reported may govern how local E/I disturbances spread through brain networks, both in experimental and clinical settings.

In particular, the present investigation reveals that E/I imbalance in $S1_W$ can spread remotely along intrahemispheric sensorimotor connections (**Figure 3.3, 3.S4**). Underlying structural connectivity appears to be a key determinant of this path of spread. Tracers injected into $S1_W$ reveal strong monosynaptic projections to ipsilateral $M1_W$, compared to a low density of callosal projections terminating in contralateral $S1_W$ (Ferezou et al., 2007). Accordingly, whisker stimulation in $S1_W$ propagates forward to strongly activate $M1_W$, followed by weaker, longer-latency activation of the contralateral hemisphere (Ferezou et al., 2007). Intrahemispheric connectivity between $S1_W$ and $M1_W$ is highly reciprocal (Mao et al., 2011, Bauer et al., 2018). This direct corticocortical circuit mediates movement initiation, such that optogenetic stimulation/inhibition of $S1_W$ directly actives/inactivates $M1_W$ to increase/decrease whisking (Sreenivasan et al., 2016). Some prior evidence suggests that PV-INs in $S1_W$ gate this connection. $S1_W$ PV-INs reduce their firing rates during whisking (Pala and Petersen, 2018), and optogenetic suppression of PV-INs enhances performance on a whisker sensorimotor transformation task (Sachidhanandam et al., 2016). We find that, indeed, bidirectional manipulation of PV-INs in $S1_W$ is sufficient to modulate ipsilateral $M1_W$ activity in the resting state. Curiously, in the setting of whisker stimulation, ipsilateral $M1_W$ did not exhibit significant changes in activity in ↓PV-ON mice (**Figure 3.6**) as it did during the resting state (**Figure 3.5B,C**), indicating that ascending thalamocortical inputs to $S1_W$ may modulate how local E/I balance is routed intracortically. It has previously been shown that while whisker sensorimotor dynamics can function independently of the thalamus (Zagha et al., 2013), they are subject to thalamic modulation. Thalamocortical inputs to $S1_W$ form stronger synaptic connections with inhibitory interneurons than excitatory neurons, positioning the cortical interneuron population to titrate local excitability via fast feedforward inhibition (Cruikshank et al., 2007). In addition, higher order thalamic inputs have been shown to play a key role in regulating $S1_W$ interneuron dynamics and local synaptic plasticity (Williams and Holtmaat, 2019). In the context of our own data, these reports would indicate that whisker stimulation may enhance thalamocortically-driven feed-forward inhibition and mitigate the effects of disinhibition of sensorimotor connectivity seen in the resting state. Thus the spread of local E/I balance is likely simultaneously modulated by both local interneurons as well as ascending thalamocortical inputs.

In addition, our results demonstrate that focal cortical E/I imbalance can disrupt interhemispheric synchrony. Chronic expression of ↑PV DREADDs in left S1$_W$ caused baseline reduction of interhemispheric correlation in S1, while strengthening interhemispheric correlation in M1, effects that were reversed after activating ↑PV DREADDs in left S1$_W$ (**Figure 3.4**). Interestingly, inhibiting left PV-INs in S1$_W$ (↓PV-ON) caused intrahemispheric hyperexcitability in left S1$_W$ and M1$_W$ (**Figure 3.5B,C**), but these activity changes did not propagate interhemispherically; rather, homotopic synchrony for both S1$_W$ and M1$_W$ became weaker (**Figure 3.4)**. Why did interhemispheric connections relay activity changes in ↑PV mice but not ↓PV mice? One possibility is that these connections might acutely buffer against interhemispheric spread of hyperexcitability (i.e., ↓PV-ON), potentially as an endogenous protective mechanism against generalization of seizures. The notion of a ceiling on interhemispheric transmission of activity changes is in line with the recent discovery that unilateral whisker sensory deprivation potentiates transcallosal projections from the intact cortex to layer V neurons in the deprived cortex (a central hub for intracortical and subcortical connectivity), such that these synapses are maximally potentiated and LTP is occluded (Petrus et al., 2019). Furthermore, we found that dramatic ON-OFF changes in stimulation-evoked excitability remained confined within the disinhibited hemisphere, with minimal interhemispheric spread of hyperexcitability (**Figure 3.6**). Conversely, 8 weeks of progressive E/I disturbance (↑PV-OFF) may engage homeostatic plasticity mechanisms that allow activity changes to spread interhemispherically (**Figure 3.S8**). It is noteworthy that activity changes spread interhemispherically between M1$_W$ cortices, but not S1$_W$ (**Figure 3.4**). This points to the importance of regional variation in structural connectivity that might impact how activity changes propagate through networks. In humans, it has previously been shown that therapeutic callosotomy in epilepsy patients eliminates most interhemispheric correlation, with a notable exception: homotopic somatomotor FC is partially preserved (Johnston et al., 2008, Roland et al., 2017). Thus, interhemispheric synchrony is mediated by distinct subcortical connections depending on region, and these circuits may differentially shunt local activity changes.

Intriguingly, a recent study revealed the existence of transcallosally-projecting PV-INs in M1, A1 and V1 (Rock et al., 2017). It has been proposed that long-range inhibitory connections mediate interhemispheric synchrony (Buzsáki and Wang, 2012), and histological evidence seems to indicate that transcallosal PV-INs are a general feature of the cortex (Rock et al., 2017). However, transcallosal PV-INs have not yet been reported in S1 to our knowledge; after careful review, we could not detect any mCherry-labeled intracortical projections in the corpus callosum or the contralateral hemisphere in any of our mice. Future studies may determine the specific cellular conduits of interhemispheric spread of activity changes, and how they vary regionally.

Disambiguating changes in functional connectivity

Using ETA effective connectivity analysis, we are able to show that changes in correlation (FC) are largely driven by high amplitude bursts of hyperexcitability. We show that bursts lead to enhanced correlation when they propagate between nodes of a network (e.g., intrahemispheric sensorimotor FC), and weakened correlation when they do not transmit between nodes (e.g., $S1_W$ homotopic FC), and that differences in correlation largely return to non-significant levels after bursts are removed from time series (**Figure 3.S9**). These findings carry important implications for interpreting pathological hypo- and hyperconnectivity in BOLD fMRI data. The effects we observed in delta band GCaMP FC (**Figure 3.4**) are also present in infraslow hemodynamics (**Figure 3.S6,7**), despite the fact that bursting dynamics are not present in the oxy-hemoglobin signal (**Figure 3.S3)**. This result indicates that BOLD fMRI may capture FC changes induced by paroxysmal hyperactivity in neural dynamics, even though the associated activity change is not represented in BOLD dynamics, which are relatively slow.

In addition, it is possible that correlation differences are also driven by disruptions in gamma oscillations. PV-INs are pacemakers that drive high frequency gamma activity (Cardin et al., 2009, Sohal et al., 2009, Chen et al., 2017). These fast oscillations have been observed to modulate slower activity, and may interact with low frequency oscillations in a manner that supports efficient long-range temporal coordination (Buzsáki and Wang, 2012, Uhlhaas and Singer, 2012). In support of this hypothesis, slow fluctuations (<0.1 Hz) in gamma LFP power exhibit long-range synchrony (Nir et al., 2008), which exhibits a similar correlation structure to infraslow BOLD FC networks (He et al., 2008).

In our own data, chemogenetic inhibition of PV-INs manifested in broadband increases in LFP power (**3.S2**), consistent with a prior report (Nguyen et al., 2014), though only increases in <25Hz activity were statistically significant in our data. This stands in contrast to a seminal investigation by Sohal et al., who optogenetically inhibited PV-INs and observed significantly reduced 30-80 Hz gamma power but increased 10-30 Hz oscillations (Sohal et al., 2009). These opposite effects in the gamma band may be due to our use of DREADDs (GPCR-based signaling, tonic change in membrane excitability) versus optogenetic inhibition (ionotropic signaling, phasic patterned firing). Another possibility, elegantly demonstrated with optogenetics by Moore et al., is that inhibition of PV-INs can paradoxically increase gamma band activity in downstream PV-INs as they counterbalance increased excitatory activity (Moore et al., 2018). In contrast, we found that activation of local PV-INs with hM3Dq DREADDs did not significantly alter local $S1_W$ activity (even while activity significantly decreased remotely in $M1_W$), which may reflect the limited sensitivity of our recording techniques or the inherent capacity of $S1_W$ ensemble dynamics to buffer against increased PV-IN inhibition. In addition, the relatively weak effect of hM3Dq DREADDs versus the strong effect of hM4Di DREADDs may reflect differences between excitatory Gq signaling (hM3Dq) via the IP3/DAG pathway versus inhibitory Gi signaling (hM4Di) through cAMP-dependent pathways, which may not produce symmetrical effects on PV-IN activity. Further investigation with single unit recordings and slice electrophysiology may better define contributions of PV-IN activity to FC changes.

Plasticity in FC induced by chemogenetic constructs in CNO-naïve mice

Notably, propagation of local E/I balance induced changes remotely along sensorimotor connections. We found that $M1_W$ excitability (**Figure 3.3, 3.3S4**) and sensorimotor synchrony (**Figure 3.4**) were consistently elevated in ↑PV-OFF mice at baseline. These differences developed progressively with 8 weeks of hM3Dq expression in CNO-naïve mice (**Figure 3.S8**). Importantly, these baseline changes are *opposite* of the acute effects of activating hM3Dq, which dampened $\mathrm{M1_W}$ excitability (**Figure 3.3**) and sensorimotor synchrony (**Figure 3.4**). In light of these findings, we hypothesize that hM3Dq DREADDs exhibit leak signaling, and that chronic low-level activation of PV-INs in $\mathrm{S1_W}$ induces compensatory plasticity that disinhibits sensorimotor connectivity and causes sustained hyperexcitability in $\mathrm{M1_W}$. These findings have important implications for the study of neural circuits *in vivo*. First, our study demonstrates that DREADDs, a tool that has exploded in popularity in recent years, can perturb brain activity in the absence of activating ligand, CNO. Second, our data suggest that local chemo- and optogenetic manipulations commonly used in local neural recordings can produce long-range effects on brain activity outside the manipulated area, which may in turn disrupt inputs feeding back in on local activity.

How might chronic leak in hM3Dq DREADDs lead to compensatory baseline changes that are opposite to the effects of acute hM3Dq activation? One such mechanism may be paradoxical inhibition of PV-INs downstream of leak-activated PV-INs, the reverse of the effect reported by Moore et al. (Moore et al., 2018). In addition, leaky chemogenetic activation of PV-INs might dysregulate the NRG1/ErbB4 axis, which positively regulates the strength of excitatory synaptic inputs onto PV-INs that drive feed-forward inhibition, and exhibits compensatory plasticity in response to chemogenetic manipulation (Sun et al., 2016). Lastly, chemogenetic activation of PV-INs may alter their myelination and axonal morphology in a manner that impacts connectivity (Stedehouder et al., 2018). Further investigation of the effects of chemogenetic constructs on cortical networks is ongoing in our laboratory.

Methodologic Limitations

This study is limited in its ability to define a specific role for PV-INs in influencing network dynamics, primarily because PV-INs are exceedingly heterogeneous in their connectivity within neural circuits. Within $S1_W$, it has been shown that different groups of PV-INs are linked by gap-junctions to form distinct components of a patterned inhibitory scaffold around cortical whisker barrel circuits (Shigematsu et al., 2019). Thus different classes of PV-expressing neurons may differently contribute to brain dynamics (locally and globally), which will require further investigation as techniques are developed for differentiating subtypes in neural recordings. In addition, PV-INs work in concert with other GABAergic subtypes (e.g., somatostatin, VIP), whose contributions to network dynamics warrant additional investigation.

Implications for translation to neurologic injury

Focal E/I imbalance may be a therapeutic target for rectifying widespread brain network dysfunction after focal neurologic injury. In addition, the present findings may provide mechanistic context for understanding FC patterns as a tool to localize injury, predict and track recovery outcomes, and identify potential therapeutic interventions. For example, traumatic brain injury (TBI) leads to progressive failure of inhibitory circuits, associated with loss of PV immunoreactivity and dissolution of perineuronal nets supporting PV-INs (Hsieh et al., 2017). Our findings suggest that such a loss of inhibition may explain hyperconnectivity in brain FC networks after TBI (Caeyenberghs et al., 2017). Likewise, many mechanistic studies have specifically implicated local PV-IN dysfunction in seizure onset (Jiang et al., 2016), which our results suggest may mediate anomalous functional connectivity between epileptogenic zones and the rest of the brain (Englot et al., 2016, Xiao et al., 2017, Centeno and Carmichael, 2014, Farrell et al., 2019). Furthermore, animal and human studies of stroke have shown that excess inhibition hampers large-scale brain networks and functional recovery after ischemia, and that therapies targeting inhibitory circuits improve network synchrony and functional recovery (Clarkson et al., 2010, Zeiler et al., 2013, Liepert et al., 2000, Kim et al., 2014, Blicher et al., 2015, Alia et al., 2016, Quattromani et al., 2018). Thus, specific molecular and cellular processes underlying imbalance in excitability may serve as potential therapeutic targets for restoring large-scale brain network connectivity after injury.

3.5 Materials and Methods

Animal models

All procedures described below were approved by the Washington University Animal Studies Committee in compliance with AAALAC guidelines. Mice were raised in standard cages in a double barrier mouse facility with a 12hr-12hr light/dark cycle and *ad libitum* access to food and water. All mice used in this study were generated as a cross between the *Thy1-GCaMP6f* strain (JAX 024276) and the *PV-Cre* strain (JAX 017320), both on a C57BL/6J background. Offspring from this cross express GCaMP6f in pyramidal neurons, and Cre recombinase in parvalbumin-expressing interneurons. Prior to experiments, pups were genotyped by PCR to confirm presence of the *Thy1-GCaMP6f* transgene, using the forward primer 5'-CATCAGTGCAGCAGAGCTTC-3' and reverse primer 5'-CAGCGTATCCACATAGCGTA-3'. Male and female mice from each litter were sorted into experimental groups using a random number generator in MATLAB, so that each litter and sex had balanced representation in each experimental group. No sex specific differences were identified in group-level analyses. Mice were 5-7 weeks of age at the time of viral injection (weights ranging 15-25g), and were 13-15 weeks of age at the start of imaging or electrophysiology experiments. Data were acquired and pooled over three independent cohorts of mice, with a total of 53 mice used in this study. Staff performing surgical procedures, neuroimaging experiments, and histology were blinded to experimental group.

Viral injections

Mice received buprenorphine analgesia (SQ, 0.03 mg/kg) and then were anesthetized with isoflurane (3% induction, 1.5% maintenance). Body temperature was maintained via thermostatic heating pad. Mice were secured in a stereotactic frame and then received 200μL of 20% mannitol per 30g bodyweight, to prevent brain swelling during surgery. The scalp was shaved, sterilized with isopropyl alcohol and betadine scrub, locally anesthetized with lidocaine, and then incised at midline and retracted. A 0.5 mm burr-hole was drilled out at coordinates for the left whisker barrel cortex from the Paxinos atlas (-1.5 mm posterior, -3.0 mm left of bregma), with intermittent application of chilled saline to the skull. Virus was loaded into a minimally invasive pulled glass pipette (tip OD 20 μm, 40° bevel). To achieve transduction of PV-INs in all cortical layers, virus was delivered in three 100 nL injections (1 nL/s, Nanoject III, Drummond Scientific, Broomhall PA), spaced at 300, 600, and 900 nm depths, pausing for 5 minutes between injections. Post-hoc histology confirmed focal targeting to $S1_W$ (Figure 3.1), with no virus expression found in the rest of the cortex. The scalp was then sutured closed and the mice recovered from anesthesia in a heated incubator. Mice were used in experiments 8 weeks later, in order to facilitate strong viral transduction and complete healing of the burr hole and injection tract prior to windowing and widefield imaging.

Chemogenetic constructs

All chemogenetic viral vectors were prepared by the Washington University School of Medicine Hope Center Viral Vectors Core: AAV8-hSyn-DIO-hM4D (Gi)-mCherry, AAV8-hSyn-DIO-hM3D (Gq)-mCherry, AAV8-hSyn-DIO-mCherry (titers adjusted to ~$7*10^{12}$ vg/mL). hM3Dq and hM4Di DREADDs consist of G-protein coupled receptors derived from the M3 or M4 muscarinic acetylcholine channels, mutated by directed evolution such that they are activated by clozapine-N-oxide (CNO) and not by endogenous ligands, leading to net depolarization or hyperpolarization of the resting membrane potential respectively for several hours (Roth, 2016). OFF recordings were collected in the absence of CNO, while ON recordings were conducted after intraperitoneal injection of CNO (1 mg/kg, AKSci). This system thus allows for two layers of comparison – between groups (↑/↓PV DREADD versus mCherry-only Control), and within group between OFF and ON states.

Histology preparation

Mice were deeply anesthetized with FatalPlus™ (Vortech Pharmaceuticals, Dearborn, MI, USA) and transcardially perfused with heparinized PBS. The brains were removed and fixed in 4% paraformaldehyde for 24 h and transferred to 30% sucrose in PBS. After brains were saturated, they were snap-frozen on dry ice and coronally sectioned (50 µm) on a sliding microtome. Sections were stored in 0.2 M PBS, 30% sucrose, and 30% ethylene glycol at −20°C. GCaMP fluorescence was confirmed in each individual using epifluorescence microscopy (Nikon Eclipse 80i, Nikon Instruments Inc., Melville, NY, USA). As described below, mCherry spatial targeting was subsequently confirmed using DAB immunohistochemistry, while colocalization with parvalbumin was confirmed using fluorescence IHC.

DAB immunohistochemistry

Sections were rinsed with PBS and then permeabilized with 0.3% PBS-T for 10 minutes. Sections were then treated with 0.3% H_2O_2 solution in PBS for 10 minutes to quench endogenous peroxidase activity. Tissue was washed with PBS and blocked with 3% dry milk in PBS-T for 60 minutes at 25°C. Sections were incubated overnight at 4°C in 1% dry milk in PBS-T solution containing polyclonal rabbit anti-mCherry antibody (1:500, NBP2-25157 Novus Biologicals, Centennial, CO). Sections were washed with PBS, and then incubated for 1 hour in blocking solution containing biotinylated anti-rabbit IgG antibody (1:400, Vector Laboratories, Burlingame, CA, USA). All sections were then incubated with avidin biotinylated enzyme complex (ABC) (1:400, Vector Laboratories) for 1 hour. Signal was visualized with 0.025% 3,3’diaminobenzidine tetrachloride (DAB), 0.25% NiCl, and 0.003% H_2O_2 in 0.05 M tris-HCl (pH 7.6) for 5-15 minutes. The sections were dried overnight on glass slides, dehydrated, and coverslipped using Permount Mounting Medium (Fisher Scientific) and then viewed with bright-field microscopy. Spatial spread of transduction was manually quantified in ImageJ (NIH, Bethesda, MD) in 5-7 slices per mouse, measuring the medial-lateral width (in mm) and cross-sectional area (in mm^2). DAB staining labels axons and dendritic arbors with better contrast than intrinsic mCherry fluorescence, allowing us to more accurately estimate the spatial extent of DREADD expression. Statistical significance was computed using a one-way ANOVA with Tukey's multiple comparison test, with significance set at an adjusted *P*-value < α=0.05.

Fluorescence immunohistochemistry

Sections were pretreated with PBS-T and blocked with 3% dry milk in PBS-T for 1 hour at 25°C. Sections were incubated overnight at 4°C in 1% dry milk in PBS-T solution containing polyclonal rabbit anti-parvalbumin antibody (1:1000, ab11427, Abcam, Cambridge, UK). After three PBS washes, sections were incubated for 1 hour at 37°C in Cy5 AffiniPure Goat Anti-Rabbit IgG (H+L) (1:800; Jackson ImmunoResearch, West Grove, PA). Sections were washed, mounted, and coverslipped with VECTASHIELD® Antifade Mounting Medium with DAPI (Vector Laboratories).

Fluorescence microscopy and cell counting

mCherry and anti-PV fluorescence were examined on an inverted confocal microscope using a 20x objective (Nikon A1-Rsi). The colocalization of mCherry fluorescence and PV-immunoreactive cells was quantified with Imaris colocalization software (Bitplane, Belfast, UK), using 6 sections per mouse, 3 images per section, centered on the mCherry labeled injection site. Statistical significance was computed using a one-way ANOVA with Tukey's multiple comparison test, with significance set at an adjusted *P*-value < α=0.05.

Cranial windowing

Mice received buprenorphine analgesia (SQ, 0.03 mg/kg) and were anesthetized with isoflurane (3% induction, 1.5% maintenance). Body temperature was maintained via thermostatic heating pad. Mice were secured in a stereotactic frame. The scalp was shaved, sterilized with isopropyl alcohol and betadine scrub, locally anesthetized with lidocaine, and then incised at midline and retracted. A custom Plexiglas window with pre-tapped screw holes for head fixation was attached to the skull using dental cement (C&B-Metabond, Parkell Inc., Edgewood, NY), completely containing the surgical opening. Mice were then placed in an incubator to rouse from anesthesia, and were allowed at least 1 week to recover from surgery before experimentation. Windows facilitate head fixation and serial non-invasive imaging in awake animals (Silasi et al., 2016, Kraft et al., 2018, Mitra et al., 2018, Wright et al., 2017b). Mice promptly resume normal behavior in their home cages (whisking, grooming, eating) and do not exhibit any signs of pain or distress from their windows.

Surgical preparation for electrophysiology

Mice received dexamethasone (20μL 4mg/mL, S.C.) 4 hours prior to surgery, and 20% mannitol (200 μL/30g bodyweight, I.P.) immediately prior to surgery. Body temperature was maintained via thermostatic heating pad. Mice were anesthetized using isoflurane anesthesia (3% induction, 1.5% maintenance) and then secured in a stereotactic frame. The scalp was shaved, sterilized with isopropyl alcohol and betadine scrub, locally anesthetized with lidocaine, and then incised at midline and retracted. A circular craniectomy (1mm in diameter) was drilled out centered over the same left barrel cortex stereotactic coordinates used for viral injection, cooling the brain intermittently with chilled saline. A second (0.5mm) burrhole was drilled at midline over the cerebellum (3 mm posterior to lambda), and a tungsten ground wire was secured in place using light-cure dental cement. A custom Plexiglas head fixation plate was attached to the skull using C&B-Metabond, completely containing the surgical opening and cerebellar ground electrode. The exposed dura in the barrel cortex craniectomy was protected with an optically-clear self-healing polymer gel that allows microelectrode probes to pass into the brain (Dow DOWSIL 3-4680, Ellsworth, Germantown WI). Mice were given buprenorphine (SQ, 0.03 mg/kg) at the end of the procedure for analgesia, and then were given 1 week of recovery time prior to recordings.

Optical imaging system

Widefield imaging of cortical calcium dynamics and hemodynamics was performed as previously described (Wright et al., 2017b). Sequential illumination was provided by four LEDs: 470nm (measured peak λ=454nm, LCS-0470-15-22, Mightex Systems, Pleasanton, CA), 530nm (measured peak λ=523nm, LCS-0530-15-22), 590nm (measured peak λ=595nm, LCS-0590-10-22), and 625nm (measured peak λ=640nm, LCS-0625-03-22). The 454nm LED was used for GCaMP excitation, and the 523nm, 595nm, and 640nm LEDs were used for multispectral oximetric imaging. The 523nm LED was also used as an emission reference for GCaMP6 fluorescence in order to remove any confound of hemodynamics in the fluorescence signal, described below. Both the 454nm and 523nm LED light paths were made collinear by using a multi-wavelength beam combiner dichroic mirror (LCS-BC25-0505, Mightex Systems). For image detection, we used a cooled, frame-transfer EMCCD camera (iXon 897, Andor Technologies, Belfast, UK) in combination with an 85mm f/1.4 camera lens (Rokinon, New York, NY). The acquisition framerate was 16.8 Hz per channel, with an overall framerate of ~67 Hz. This framerate is well above the temporal resolution necessary to characterize GCaMP6 dynamics. To maintain a high frame rate and increase SNR, the CCD was binned at 4 x 4 pixels; this reduced the resolution of the output images from full-frame 512 x 512 pixels to 128 x 128 pixels. Both the LEDs and the exposure of the CCD were synchronized and triggered via a DAQ (PCI-6733, National Instruments, Austin, TX) using MATLAB (MathWorks, Natick, MA). The field-of-view was adjusted to be approximately 1 cm^2. The resulting pixels were approximately 78μm x 78μm. To minimize specular reflection from the skull, we used a series of linear polarizers in front of the LED sources and the CCD lens. Head-fixed mice were placed at the focal plane of the camera. The combined, collimated LED unit was placed approximately 8 cm from the mouse skull, with a working distance of approximately 14cm as determined by the acquisition lens. A 515nm longpass filter (Semrock, Rochester, NY) was placed in front of the CCD to filter out 470nm fluorescence excitation light and a 460/60nm bandpass filter (Semrock, Rochester, NY) was used in front of the excitation source to further minimize leakage of fluorescence excitation light through the 515nm longpass filter. The pulse durations for the LEDs were 20ms, 5ms, 3ms, 1ms for 454nm, 523nm, 595nm, and 640nm, respectively.

Optical Imaging recordings

All imaging sessions were performed in awake, unanesthetized mice. Mice were acclimated to head-fixation while secured in comfortable black felt hammock until they resumed normal resting behavior (whisking, grooming, relaxed posture). Mice habituated in this manner are qualitatively observed to be still and relaxed during recordings, and show robust individual FC patterns that we have observed to be highly consistent over consecutive days of repeat recordings. Resting state imaging was collected in 10-minute epochs for each mouse at baseline and at 10-minute intervals after delivery of CNO (IP injection, 1 mg/kg, AKSci, Union City, CA), leaving the mouse fixed in place to preserve an identical field of view between conditions and time points. Whisker stimulation recordings were performed in a separate session, using 5-minute epochs per condition (right vs. left side, pre- and post-CNO). Stimulus was delivered using computer-triggered 40 PSI air puffs (Picospritzer, Parker Hannifin, Cleveland, OH) in a block design (5s rest; 5s of 1 Hz, 0.1s puffs; 10s rest; 15 blocks/5 min. total).

Electrophysiology recordings

All electrophysiology recordings were performed in awake, unanesthetized mice. As in the imaging experiments, mice were acclimated to head-fixation in a black felt hammock until they resumed normal resting behavior. A 1.5mm 16-channel linear array electrode (NeuroNexus, A1x16-5mm-100-703-A16, Ann Arbor, MI) was attached with a custom adaptor to a micromanipulator (David Kopf Instruments, Los Angeles, CA). The electrode was stereotactically inserted into the brain through the transparent self-healing silicone polymer overlying the dura, enabling direct visualization via surgical stereoscope (Olympus, Tokyo, Japan). The probe was inserted to a consistent depth of 1.5 mm using the stereotactic manipulator, with secondary confirmation by 1) visually guiding the most superficial contact to just under the cortical surface, and 2) observing the noise to signal transition as the most superficial electrode moved from noise/air into brain parenchyma. Local field potentials were recorded using an amplifier with a high-pass filter cutoff of 0.02Hz (Intan RDH2132, Los Angeles, CA) connected to the recording computer through an acquisition board (OpenEphys), with a tungsten reference wire positioned in the cerebellum. All recordings were made inside of a Faraday cage in a completely dark room. For each mouse, baseline recordings were collected in 10-minute epochs, followed by CNO injection (IP injection, 1 mg/kg), followed by a 40-minute continuous recording, without moving the mouse or the electrode in the brain between baseline and CNO recordings.

Optical imaging signal processing

A binary brain mask was manually drawn in MATLAB for each recording session in each mouse. All subsequent analyses were performed on pixels labeled as brain. Image sequences from each mouse (as well as the brain mask for each mouse) were affine-transformed to Paxinos atlas space using the positions of bregma and lambda (Franklin and Paxinos, 2012). A representative frame of baseline light levels in a dark environment, calculated from a mean of dark images collected over 1 minute, was subtracted from the raw data. All pixel time traces were then spatially and temporally detrended to correct for any variations in light levels due to photobleaching, LED current drift, and nonuniformity across the skull (Kubota et al., 2008). Reflectance changes in the 523nm, 595nm, and 640nm LED channels were used in combination to provide hemoglobin oximetric data using the modified Beer-Lambert Law, as described previously (White et al., 2011). The GCaMP6 fluorescence signal (ΔF’) was corrected for varying concentrations of absorptive hemoglobin using 523nm LED reflectance, adapting a previously described method.(Ma et al., 2016b) Images in each contrast were smoothed with a Gaussian filter (5x5 pixel box with a 1.3-pixel standard deviation). Global signal from within the mask-defined brain space was regressed from all data to highlight the underlying sub-architecture of regional connectivity, as done in fMRI preprocessing algorithms.(Fox et al., 2009) Parallel analysis without global signal regression revealed similar correlation changes but with decreased spatial specificity (data not shown). Each imaging session was analyzed for light level fluctuations to identify any epochs exhibiting motion artifact (typically due to displacement of the felt blanket used to tuck mice into their hammock). We subsequently excluded three 5-minute epochs of stimulation data (out of 900 minutes total across all mice) and two 10-minute epochs of resting state data (out of 1380 minutes total).

Electrophysiology signal processing

16-channel recordings were referenced to a tungsten ground wire positioned on the cerebellum. To further verify which channels were within the somatosensory cortex, we analyzed the spectral content of all channels, and found similar power in channels 1-12 and then lower power in channels 13-16, indicating that channels 1-12 were in the cortex while channels 13-16 were in subcortical white matter (hence, excluded from analysis). Signal in each channel was decimated (4th order Chebyshev filter) and then bandpass filtered to 0.01-100 Hz (2nd order Butterworth filter) to extract local field potentials. LFP oscillations in each of the 12 cortical channels were observed to be qualitatively similar, and were averaged within each individual mouse to improve SNR. After manually reviewing individual mouse LFP traces for non-stationarities due to suspected motion, 2.5 minutes of data (in 2 epochs) were excluded (out of 800 minutes total).

Optical imaging ROIs

$S1_W$, $S1_{FP}$, and $M1_W$ ROIs are based on functional stimulus mapping from an independent cohort of 21 twelve-week-old *Thy1-GCaMP6f* mice. Whisker stimulation evoked maps were measured in awake mice using air puffs as described above, 5 minutes/mouse. Forepaw maps were elicited with mild electrical shocks under anesthesia (86.9mg/kg ketamine, 13.4mg/kg xylazine, IP) with a heating pad to maintain body temperature. Transcutaneous electrical stimulation of the forepaw was applied with microvascular clips (Roboz) in a block design (5 s rest; 10s 3Hz, 1.0 mA, 0.3ms electrical pulses; 10s rest; 15 blocks/5 minutes total per mouse). 15 x 20s stimulus blocks were averaged within each mouse and then the peak frames for each of 5 air puffs/20 s block or 30 shocks/20 s block were averaged into one mean maximal amplitude frame per mouse. Mean maximal amplitude frames were averaged across mice, and then an evoked response ROI was defined by any pixels whose mean maximal amplitude during stimulus was within >75% of the maximum pixel intensity within the brain. ROIs generated from this approach are depicted in Figure 3.1A and were used in subsequent analyses for averaging within functional territories. ROI locations were co-registered to experimental data using affine-transformation to Paxinos atlas space as described in the “Optical imaging signal processing” section above.

Computation of power spectral density:

Power spectra for oxy-Hb, GCaMP (Figure 3.S1A,B) were computed using the fast Fourier Transform (FFT) while power spectra for LFP (Figure 3.S1C) were computed by averaging all windows of a short time Fourier transform (STFT). Spectra were computed over a 10-minute OFF epoch and a 10-minute ON epoch beginning 30 minutes after CNO injection. Spectra were averaged between mice and then smoothed with a 4th order Savitzky-Golay filter. Power spectra for LFP in Figure 3.S1D were re-computed using the continuous wavelet transform function in MATLAB (Morse wavelet), and then averaging scalograms across time. Band-limited power differences were quantified for both Fourier and wavelet methods in Figure 3.S2 and statistically verified by two-way ANOVA with Sidak's multiple comparison test, with significance set at an adjusted *P*-value < α=0.05. In addition, power change (in decibels) was computed using the equation:

$$\Delta Power = 10\log_{10}\left(\frac{Power_{ON}}{Power_{OFF}}\right) \tag{E1}$$

Within each mouse, power changes for optical imaging signals (oxy-Hb and GCaMP) were computed by FFT on a pixel-wise basis (shown as maps in Figures 3.3a and 3.S3) which subsequently averaged within a given ROI (Figures 3.3C-E and 3.S1E). Power changes for LFP in Figure 3.3 were computed with the short-time Fourier transform over continuous time series, using the spectrogram function in MATLAB (Hamming window of 6000 samples, 75% overlap), comparing power in each window in the 40-minute ON epoch to the time-averaged STFT of the 10-minute OFF epoch using equation E1. Statistical significance for power changes (Figure 3.3c-f) was computed using a two-way ANOVA with Tukey's multiple comparison test, with significance set at an adjusted *P*-value < α=0.05. In subsequent analyses of optical imaging data, we focus on the classic

BOLD infraslow band (<0.1 Hz) and the delta band (1-4 Hz). These bounds on the delta band were chosen to improve signal to noise, by avoiding a 0.1-1 Hz transition point in global wave propagation that we have previously reported (Mitra et al., 2018), as well as cardiorespiratory peaks at >5 Hz (observable in Figure 3.S1).

Computation of correlation (FC):

For all analyses, FC was computed over specific frequency bands by applying zero-phase filtering (fifth order Butterworth) directly to GCaMP6 and hemoglobin signals, using 0.02-0.1 Hz for infraslow and 1-4 Hz for the delta band as described above. Pearson correlation, , was computed in two ways. In order to broadly survey FC changes, we computed correlation matrices in Figure 3.S5 by comparing the time series between every pair of pixels in the brain space, and . Thus,

$$r_{x_1 x_2} = \frac{1}{\sigma_{x_1}\sigma_{x_2}}\frac{1}{T}\int x_1\,(t)\cdot x_2(t)dt \tag{E2}$$

where σ_{x_1} and σ_{x_2} are the temporal standard deviations of signals x_1 and x_2, and T is the interval of integration. We noted that FC changes were most prominent in the sensory and motor cortices. To enhance signal-to-noise and better visualize these changes, we re-computed correlation maps comparing the average time series within empirically determined whisker S1 and M1 ROIs versus the time series of every pixel in the brain space (Figure S7). FC for all figures is reported following Fisher z-transformation:

$$z\,(r) = \tanh^{-1}\,(r) \tag{E3}$$

Pixel-wise FC matrices shown in Figure 3.S5 were sorted into large functional territories using a previously described parcellation (Kraft et al., 2017). Difference matrices (Figure

3.S5) and maps (Figure 3.4 for GCaMP, 3.S6 for oxy-hemoglobin) were computed by array subtraction of FC matrices/maps for a 10-minute OFF epoch and a 10-minute ON epoch beginning 30 minutes after CNO injection. Group averaged and individual mouse FC patterns were qualitatively observed to be robust to varying size and shape of seed ROIs centered on $S1_W$ and $M1_W$. Spatial principal component analysis (PCA) was performed on difference matrices by singular value decomposition in MATLAB, generating a topographic map of the first PC weighted by its eigenvalue. Statistical significance for average differences in FC (Figure 3.4E-G) between seeds and other ROIs was computed using a two-way ANOVA with Tukey's multiple comparison test, with significance set at an adjusted P-value $< \alpha=0.05$.

Computation of event-triggered averaging

Event-triggered averaging was used to describe cortical dynamics during local peaks in $S1_W$ GCaMP time-series. For each mouse session, GCaMP time series were averaged within $S1_W$ ROI pixels and then filtered into the delta band (1-4 Hz, fifth order Butterworth). All local maxima in the delta band were sorted by amplitude; those exceeding the 90th percentile were averaged together within individual mouse sessions (shown in Figure 3.5). Differences in group-level averages were statistically verified by two-way ANOVA with Tukey's multiple comparison test, with significance set at an adjusted P-value $< \alpha=0.05$. In order to determine the impact of paroxysmal bursts on delta-band FC (Figure 3.S9), five frames preceding and succeeding (± ~.3 s) each peak were excised from the time series prior to re-computing ROI seed-based FC as described above. The threshold for removing peaks was varied from the 90th (as above) to the 50th percentile value of all local delta peaks in order to assess FC as a function of increasingly stringent exclusion criteria (i.e., how local activity at different scales contributes to long-range correlations). FC changes following removal of peaks below the 50th percentile value remained stable and are not shown. Differences in FC were statistically verified by two-way ANOVA with Sidak's multiple comparison test, with significance set at an adjusted *P*-value < α=0.05

Computation of whisker evoked sensory maps

Mean 20-second stimulus blocks were averaged within each mouse and then across mice. Mean response maps shown in Figure 3.6A,B depict peak frames averaged across 5 air puffs/block. Mean time series in Figure 3.6A,B were generated by averaging the GCaMP signal for all pixels within right and left $S1_W$ ROIs. GCaMP fluorescence intensity during stimulation was monitored over a 12-hour period. Differences between ROIs and groups were verified in Figure 3.6C,E using a two-way ANOVA with Tukey's multiple comparison test, significance set at an adjusted *P*-value < α=0.05. Changes over time were statistically verified in Figure 3.6D using a two-way ANOVA with Dunnett's multiple comparison test, significance set at an adjusted *P*-value < α=0.05.

Data presentation and statistical analysis

Histograms and scatter plots are presented as group mean ± standard error of the group mean for all experiments, with data points representing individual mice within each group. Color-map data are plotted using the open source Viridis family of color-maps, which are perceptually uniform and robust to colorblindness. Sample sizes were estimated based on prior GCaMP imaging experiments performed by our group. Randomization and blinding were performed as described above in Animal Models. Prism 8 software was used to perform statistical testing. Statistical significance was computed via one-way ANOVA for histology data in Figure 3.1, and two-way ANOVA for all other figures. Tukey’s multiple comparison test was used for Figures 3.1, 3.3, 3.4, 3.5, 3.6c, 3.6e, 3.S3, and 3.S6; Sidak’s test was used in Figures 3.S2 and 3.S9; Dunnett’s test was used in Figure 3.6d. Statistical significance for all figures is reported as not significant ($^{NS}P > 0.05$) or significant ($^{*}P < 0.05$, $^{**}P < 0.01$, $^{***}P < 0.001$, and $^{****}P < 0.001$). Data were verified to be normally distributed prior to statistical testing using the Shapiro-Wilk normality test. Multiple comparison testing was done at the level of individual figure panel plots, including all possible comparisons within each plot within and between groups and ON-OFF states. For the sake of visual clarity, only ON-OFF differences within group are depicted within figures, while significant between-group effects are described in the main text.

Chapter 4: Conclusions and Future Directions

In this dissertation, I have provided evidence that local activity changes in cortical circuits have far-reaching effects on macroscale network dynamics. I demonstrate that homotopically paired somatosensory cortices play a key role in initiating global slow waves in response to sensory stimulation, and that ischemic stroke in S1 of either hemisphere can disrupt global slow wave initiation. In addition, I show that chemogenetic manipulation of parvalbumin interneurons models focal epileptiform activity, that imbalances in excitability propagate differentially through cortical network connections, and that chronic focal hyperexcitability induces plasticity in macroscale dynamics. Importantly, we show that while epileptiform discharges do not grossly manifest in infraslow hemodynamic signals, they nevertheless induce changes in hemodynamic measures of FC. These studies thus add to a growing body of mechanistic optical neuroimaging literature in mouse models that provides important clues for how to interpret disruptions in macroscale networks observed in human fMRI/EEG. The future of this field has enormous potential to translate macroscopic brain recording into a clinically useful tool for diagnosis, prognosis, and guiding therapeutic intervention.

The translational potential of mouse optical neuroimaging will be greatly enhanced by resolving cellular level resolution over large territories. The necessary technology has advanced considerably in the last decade. 2 photon GCaMP imaging with cellular resolution has advanced to imaging whole zebra fish brains (Ahrens et al., 2013), thousands of CA1 pyramidal neurons (Ziv et al., 2013), multiple fields of view (Lecoq et al., 2014), and the whole cortex (Kim et al., 2016, Sofroniew et al., 2016, Stirman et al., 2016). Current technology remains limited by scanning speeds, loss of resolution due to light scattering, tissue heating by intense illumination, and fabrication of large enough photon multiplier tubes (PMTs) for large fields of view. Recent advances in macroscope design (Kauvar et al., 2020), and soma targeting of GCaMP (Shemesh et al., 2020, Chen et al., 2020b) may help to overcome these barriers. In addition, the computational demands of processing and analyzing massive volumes of cellular resolution data also pose a significant obstacle.

The next generations of chemosensors may facilitate faster detection of neural oscillations with higher signal-to-noise and fewer off target effects. For example, newly designed GCaMP sensors may resolve current issues with some GCaMP models in which over-expression leads to nuclear accumulation, aberrant calcium dynamics, and hyperexcitability (Steinmetz et al., 2017). This can be resolved by incorporating an extra apoCaM-binding motif to prevent disruption of L-type calcium channels (Yang et al., 2018), or by using fungal derived proteins that reduce interaction with the intracellular environment of neurons (Barykina et al., 2020). In addition, red-shifted calcium sensors like jRGECO1a are now available in transgenic mice, which produce less light scattering and thus reduced photodamage, allowing for deeper imaging of cortex than GFP based sensors (Dana et al., 2016, Dana et al., 2018). Red-shifted fluorescence indicators also allow for experiments combining optical imaging with optogenetic stimulation using green light-sensitive channels like channelrhodopsin, as well as simultaneous imaging of distinct populations labeled with two colors of calcium indicators (Sun et al., 2017). New photoconvertible calcium sensors like CaMPARI further enable labeling of active neural populations in parallel with calcium imaging, which may prove a valuable tool for dissecting the effects of local circuits on macroscale dynamics, especially if combined with post hoc histology and slice electrophysiology of marked neurons (Moeyaert et al., 2018, Ebner et al., 2019). While calcium sensors have been the dominant optical imaging tool to date, recent advances in genetically encoded voltage sensors may facilitate increased usage for *in vivo* imaging (Abdelfattah et al., 2020, Monakhov et al., 2019). For all genetically encoded sensors, new techniques for designer viral transgene delivery will likely enable more flexible targeting of sensors to characterize macroscale dynamics of specific cell types without the constraints of working in transgenic animals (Hrvatin et al., 2019, Vormstein-Schneider et al., 2020).

Lastly, it is worth noting that while fMRI has very limited spatiotemporal resolution, and typically requires anesthesia in rodents to reduce motion artifact, it remains the gold standard for capturing macroscale dynamics of subcortical structures. Significant strides have been made towards optimizing rodent fMRI for awake recordings (Zhang et al., 2010, Gao et al., 2017), though these methods have yet to be widely adopted by the field. In addition, the translational utility of fMRI in rodent models can be broadened by combining it with other recording techniques like local calcium imaging (He et al., 2018, Ma et al., 2020) and LFP measurement (Pan et al., 2013, Liu et al., 2018, Jaime et al., 2018), as well as manipulation with optogenetics (Chan et al., 2017, Wang et al., 2019, Chen et al., 2020c) and chemogenetics (Roelofs et al., 2017, Giorgi et al., 2017, Zerbi et al., 2019, Nakamura et al., 2020, Peeters et al., 2020). Furthermore, oxygen polarography can serve as a local, high temporal resolution surrogate of the BOLD fMRI signal, and in combination with electrophysiology this technique has proven valuable for probing origins of functional connectivity (Bentley et al., 2016, Li et al., 2015).

The development of this broad array of tools is a tremendous technologic feat. However, it must be emphasized how much we still do not know about the basic physiology of the brain, and the questions our tools have not yet adequately answered:

- What is the function of spontaneous activity in the resting brain?
- What role do specific cortical and subcortical structures play in synchronizing macroscale network dynamics, and how do these contributions vary with brain state?
- What are the relative contributions of the diverse array of excitatory, inhibitory, and neuromodulatory cellular actuators in shaping network dynamics?
- How are sensory, motor, and cognitive functions represented in multiscale brain dynamics?
- Why does infraslow activity take on a unique spatiotemporal structural versus faster activity, and why do infraslow and faster activity reverse directions between wake and sleep?
- To what extent does infraslow activity shape higher frequency dynamics, and vice versa?
- What is the function of correlation and anticorrelation in brain networks?

- What role does interhemispheric synchrony play in brain computational function?
- To what extent can therapeutic manipulation restore healthy network function, either by targeting local circuits or broadly distributed networks?

Indeed, understanding how the human brain encodes multi-scale dynamics remains perhaps the greatest challenge of all modern biology. Here we have shown how optical imaging in mice has advanced the frontiers of experimental access to the extraordinary complexity of brain dynamics, permitting broader, higher resolution cross-sections of activity than have ever been seen before. This technology holds the potential to translate macroscopic brain recordings in humans into a valuable clinical biomarker, such that changes in connectivity can be mechanistically attributed to well-defined physiology. A deeper understanding of the underpinnings of macroscale brain dynamics will revolutionize our ability to diagnose and treat neurologic and psychiatric disease.

References

ABDELFATTAH, A. S., VALENTI, R., ZHENG, J., WONG, A., TEAM, G. P., PODGORSKI, K., KOYAMA, M., KIM, D. S. & SCHREITER, E. R. 2020. A general approach to engineer positive-going eFRET voltage indicators. *Nat Commun,* 11**,** 3444.

AHRENS, M. B., ORGER, M. B., ROBSON, D. N., LI, J. M. & KELLER, P. J. 2013. Whole-brain functional imaging at cellular resolution using light-sheet microscopy. *Nat Methods,* 10**,** 413-20.

AKEMANN, W., MUTOH, H., PERRON, A., PARK, Y. K., IWAMOTO, Y. & KNOPFEL, T. 2012. Imaging neural circuit dynamics with a voltage-sensitive fluorescent protein. *J Neurophysiol,* 108**,** 2323-37.

ALIA, C., SPALLETTI, C., LAI, S., PANARESE, A., MICERA, S. & CALEO, M. 2016. Reducing GABAA-mediated inhibition improves forelimb motor function after focal cortical stroke in mice. *Sci Rep,* 6**,** 37823.

AMZICA, F. & STERIADE, M. 1995. Disconnection of intracortical synaptic linkages disrupts synchronization of a slow oscillation. *J Neurosci,* 15**,** 4658-4677.

ANACLET, C., FERRARI, L., ARRIGONI, E., BASS, C. E., SAPER, C. B., LU, J. & FULLER, P. M. 2014. The GABAergic parafacial zone is a medullary slow wave sleep-promoting center. *Nat Neurosci,* 17**,** 1217-24.

ASHBY, D. M., LEDUE, J., MURPHY, T. H. & MCGIRR, A. 2019. Peripheral Nerve Ligation Elicits Widespread Alterations in Cortical Sensory Evoked and Spontaneous Activity. *Sci Rep,* 9**,** 15341.

ASWENDT, M., PALLAST, N., WIETERS, F., BAUES, M., HOEHN, M. & FINK, G. R. 2020. Lesion Size- and Location-Dependent Recruitment of Contralesional Thalamus and Motor Cortex Facilitates Recovery after Stroke in Mice. *Transl Stroke Res*.

AVVENUTI, G., HANDJARAS, G., BETTA, M., CATALDI, J., IMPERATORI, L. S., LATTANZI, S., RIEDNER, B. A., PIETRINI, P., RICCIARDI, E., TONONI, G., SICLARI, F., POLONARA, G., FABRI, M., SILVESTRINI, M., BELLESI, M. & BERNARDI, G. 2020. Integrity of corpus callosum is essential for the cross-hemispheric propagation of sleep slow waves: a high-density EEG study in split-brain patients. *J Neurosci*.

BALDASSARRE, A., RAMSEY, L. E., SIEGEL, J. S., SHULMAN, G. L. & CORBETTA, M. 2016. Brain connectivity and neurological disorders after stroke. *Curr Opin Neurol,* 29**,** 706-713.

BARRAL, J. & REYES, A. D. 2016. Synaptic scaling rule preserves excitatory-inhibitory balance and salient neuronal network dynamics. *Nat Neurosci,* 19**,** 1690-1696.

BARYKINA, N. V., SOTSKOV, V. P., GRUZDEVA, A. M., WU, Y. K., PORTUGUES, R., SUBACH, O. M., CHEFANOVA, E. S., PLUSNIN, V. V., IVASHKINA, O. I., ANOKHIN, K. V., VLASKINA, A. V., KORZHENEVSKIY, D. A., NIKOLAEVA, A. Y., BOYKO, K. M., RAKITINA, T. V., VARIZHUK, A. M., POZMOGOVA, G. E. & SUBACH, F. V. 2020. FGCaMP7, an Improved Version of Fungi-Based Ratiometric Calcium Indicator for In Vivo Visualization of Neuronal Activity. *Int J Mol Sci,* 21.

BAUER, A. Q., KRAFT, A. W., BAXTER, G. A., WRIGHT, P. W., REISMAN, M. D., BICE, A. R., PARK, J. J., BRUCHAS, M. R., SNYDER, A. Z., LEE, J. M. & CULVER, J. P. 2018. Effective Connectivity Measured Using Optogenetically Evoked Hemodynamic Signals Exhibits Topography Distinct from Resting State Functional Connectivity in the Mouse. *Cereb Cortex,* 28**,** 370-386.

BAUER, A. Q., KRAFT, A. W., WRIGHT, P. W., SNYDER, A. Z., LEE, J. M. & CULVER, J. P. 2014. Optical imaging of disrupted functional connectivity following ischemic stroke in mice. *Neuroimage,* 99**,** 388-401.

BAYER, L., CONSTANTINESCU, I., PERRIG, S., VIENNE, J., VIDAL, P. P., MUHLETHALER, M. & SCHWARTZ, S. 2011. Rocking synchronizes brain waves during a short nap. *Curr Biol,* 21**,** R461-2.

BELLESI, M., RIEDNER, B. A., GARCIA-MOLINA, G. N., CIRELLI, C. & TONONI, G. 2014. Enhancement of sleep slow waves: underlying mechanisms and practical consequences. *Front Syst Neurosci,* 8**,** 208.

BELTRAMO, R., D'URSO, G., DAL MASCHIO, M., FARISELLO, P., BOVETTI, S., CLOVIS, Y., LASSI, G., TUCCI, V., DE PIETRI TONELLI, D. & FELLIN, T. 2013. Layer-specific excitatory circuits differentially control recurrent network dynamics in the neocortex. *Nat Neurosci,* 16**,** 227-34.

BENTLEY, W. J., LI, J. M., SNYDER, A. Z., RAICHLE, M. E. & SNYDER, L. H. 2016. Oxygen Level and LFP in Task-Positive and Task-Negative Areas: Bridging BOLD fMRI and Electrophysiology. *Cereb Cortex,* 26**,** 346-57.

BHATIA, A., MOZA, S. & BHALLA, U. S. 2019. Precise excitation-inhibition balance controls gain and timing in the hippocampus. *Elife,* 8.

BINDER, S., BERG, K., GASCA, F., LAFON, B., PARRA, L. C., BORN, J. & MARSHALL, L. 2014. Transcranial slow oscillation stimulation during sleep enhances memory consolidation in rats. *Brain Stimul,* 7**,** 508-15.

BLICHER, J. U., NEAR, J., NAESS-SCHMIDT, E., STAGG, C. J., JOHANSEN-BERG, H., NIELSEN, J. F., OSTERGAARD, L. & HO, Y. C. 2015. GABA levels are decreased after stroke and GABA changes during rehabilitation correlate with motor improvement. *Neurorehabil Neural Repair,* 29**,** 278-86.

BOKIL, H., ANDREWS, P., KULKARNI, J. E., MEHTA, S. & MITRA, P. P. 2010. Chronux: a platform for analyzing neural signals. *J Neurosci Methods,* 192**,** 146-51.

BONHOEFFER, T. & GRINVALD, A. 1991. Iso-orientation domains in cat visual cortex are arranged in pinwheel-like patterns. *Nature,* 353**,** 429-31.

BOUCHARD, M. B., CHEN, B. R., BURGESS, S. A. & HILLMAN, E. M. 2009. Ultra-fast multispectral optical imaging of cortical oxygenation, blood flow, and intracellular calcium dynamics. *Opt Express,* 17**,** 15670-8.

BRIER, L. M., LANDSNESS, E. C., SNYDER, A. Z., WRIGHT, P. W., BAXTER, G. A., BAUER, A. Q., LEE, J. M. & CULVER, J. P. 2019. Separability of calcium slow waves and functional connectivity during wake, sleep, and anesthesia. *Neurophotonics,* 6**,** 035002.

BUKHARI, Q., SCHROETER, A. & RUDIN, M. 2018. Increasing isoflurane dose reduces homotopic correlation and functional segregation of brain networks in mice as revealed by resting-state fMRI. *Sci Rep,* 8**,** 10591.

BUZSAKI, G. & DRAGUHN, A. 2004. Neuronal oscillations in cortical networks. *Science,* 304**,** 1926-9.

BUZSÁKI, G. & WANG, X. J. 2012. Mechanisms of gamma oscillations. *Annu Rev Neurosci,* 35**,** 203-25.

CAEYENBERGHS, K., VERHELST, H., CLEMENTE, A. & WILSON, P. H. 2017. Mapping the functional connectome in traumatic brain injury: What can graph metrics tell us? *Neuroimage,* 160**,** 113-123.

CALIN, A., STANCU, M., ZAGREAN, A. M., JEFFERYS, J. G. R., ILIE, A. S. & AKERMAN, C. J. 2018. Chemogenetic Recruitment of Specific Interneurons Suppresses Seizure Activity. *Front Cell Neurosci,* 12**,** 293.

CARANDINI, M., SHIMAOKA, D., ROSSI, L. F., SATO, T. K., BENUCCI, A. & KNOPFEL, T. 2015. Imaging the awake visual cortex with a genetically encoded voltage indicator. *J Neurosci,* 35**,** 53-63.

CARDIN, J. A., CARLEN, M., MELETIS, K., KNOBLICH, U., ZHANG, F., DEISSEROTH, K., TSAI, L. H. & MOORE, C. I. 2009. Driving fast-spiking cells induces gamma rhythm and controls sensory responses. *Nature,* 459**,** 663-7.

CARMICHAEL, S. T. 2012. Brain excitability in stroke: the yin and yang of stroke progression. *Arch Neurol,* 69**,** 161-7.

CARTER, A. R., SHULMAN, G. L. & CORBETTA, M. 2012. Why use a connectivity-based approach to study stroke and recovery of function? *Neuroimage,* 62**,** 2271-80.

CENTENO, M. & CARMICHAEL, D. W. 2014. Network Connectivity in Epilepsy: Resting State fMRI and EEG-fMRI Contributions. *Front Neurol,* 5**,** 93.

CHAN, R. W., LEONG, A. T. L., HO, L. C., GAO, P. P., WONG, E. C., DONG, C. M., WANG, X., HE, J., CHAN, Y. S., LIM, L. W. & WU, E. X. 2017. Low-frequency hippocampal-cortical activity drives brain-wide resting-state functional MRI connectivity. *Proc Natl Acad Sci U S A,* 114**,** E6972-E6981.

CHANDRASEKAR, A., HEUVEL, F. O., TAR, L., HAGENSTON, A. M., PALMER, A., LINKUS, B., LUDOLPH, A. C., HUBER-LANG, M., BOECKERS, T., BADING, H. & ROSELLI, F. 2019. Parvalbumin Interneurons Shape Neuronal Vulnerability in Blunt TBI. *Cereb Cortex,* 29**,** 2701-2715.

CHEN, G., ZHANG, Y., LI, X., ZHAO, X., YE, Q., LIN, Y., TAO, H. W., RASCH, M. J. & ZHANG, X. 2017. Distinct Inhibitory Circuits Orchestrate Cortical beta and gamma Band Oscillations. *Neuron,* 96**,** 1403-1418 e6.

CHEN, Q., CICHON, J., WANG, W., QIU, L., LEE, S. J., CAMPBELL, N. R., DESTEFINO, N., GOARD, M. J., FU, Z., YASUDA, R., LOOGER, L. L., ARENKIEL, B. R., GAN, W. B. & FENG, G. 2012. Imaging neural activity using Thy1-GCaMP transgenic mice. *Neuron,* 76**,** 297-308.

CHEN, T. W., WARDILL, T. J., SUN, Y., PULVER, S. R., RENNINGER, S. L., BAOHAN, A., SCHREITER, E. R., KERR, R. A., ORGER, M. B., JAYARAMAN, V., LOOGER, L. L., SVOBODA, K. & KIM, D. S. 2013. Ultrasensitive fluorescent proteins for imaging neuronal activity. *Nature,* 499**,** 295-300.

CHEN, W., PARK, K., PAN, Y., KORETSKY, A. P. & DU, C. 2020a. Interactions between stimuli-evoked cortical activity and spontaneous low frequency oscillations measured with neuronal calcium. *Neuroimage,* 210**,** 116554.

CHEN, Y., JANG, H., SPRATT, P. W. E., KOSAR, S., TAYLOR, D. E., ESSNER, R. A., BAI, L., LEIB, D. E., KUO, T. W., LIN, Y. C., PATEL, M., SUBKHANGULOVA, A., KATO, S., FEINBERG, E. H., BENDER, K. J., KNIGHT, Z. A. & GARRISON, J. L. 2020b. Soma-Targeted Imaging of Neural Circuits by Ribosome Tethering. *Neuron*.

CHEN, Y., SOBCZAK, F., PAIS-ROLDAN, P., SCHWARZ, C., KORETSKY, A. P. & YU, X. 2020c. Mapping the Brain-Wide Network Effects by Optogenetic Activation of the Corpus Callosum. *Cereb Cortex*.

CIVILLICO, E. F. & CONTRERAS, D. 2012. Spatiotemporal properties of sensory responses in vivo are strongly dependent on network context. *Front Syst Neurosci,* 6**,** 25.

CLARKSON, A. N., HUANG, B. S., MACISAAC, S. E., MODY, I. & CARMICHAEL, S. T. 2010. Reducing excessive GABA-mediated tonic inhibition promotes functional recovery after stroke. *Nature,* 468**,** 305-9.

CONNOR, S. A., AMMENDRUP-JOHNSEN, I., CHAN, A. W., KISHIMOTO, Y., MURAYAMA, C., KURIHARA, N., TADA, A., GE, Y., LU, H., YAN, R., LEDUE, J. M., MATSUMOTO, H., KIYONARI, H., KIRINO, Y., MATSUZAKI, F., SUZUKI, T., MURPHY, T. H., WANG, Y. T., YAMAMOTO, T. & CRAIG, A. M. 2016. Altered Cortical Dynamics and Cognitive Function upon Haploinsufficiency of the Autism-Linked Excitatory Synaptic Suppressor MDGA2. *Neuron,* 91**,** 1052-1068.

CRUIKSHANK, S. J., LEWIS, T. J. & CONNORS, B. W. 2007. Synaptic basis for intense thalamocortical activation of feedforward inhibitory cells in neocortex. *Nat Neurosci,* 10**,** 462-8.

DANA, H., CHEN, T. W., HU, A., SHIELDS, B. C., GUO, C., LOOGER, L. L., KIM, D. S. & SVOBODA, K. 2014. Thy1-GCaMP6 transgenic mice for neuronal population imaging in vivo. *PLoS One,* 9**,** e108697.

DANA, H., MOHAR, B., SUN, Y., NARAYAN, S., GORDUS, A., HASSEMAN, J. P., TSEGAYE, G., HOLT, G. T., HU, A., WALPITA, D., PATEL, R., MACKLIN, J. J., BARGMANN, C. I., AHRENS, M. B., SCHREITER, E. R., JAYARAMAN, V., LOOGER, L. L., SVOBODA, K. & KIM, D. S. 2016. Sensitive red protein calcium indicators for imaging neural activity. *Elife,* 5.

DANA, H., NOVAK, O., GUARDADO-MONTESINO, M., FRANSEN, J. W., HU, A., BORGHUIS, B. G., GUO, C., KIM, D. S. & SVOBODA, K. 2018. Thy1 transgenic mice expressing the red fluorescent calcium indicator jRGECO1a for neuronal population imaging in vivo. *PLoS One,* 13**,** e0205444.

DAVID, F., SCHMIEDT, J. T., TAYLOR, H. L., ORBAN, G., DI GIOVANNI, G., UEBELE, V. N., RENGER, J. J., LAMBERT, R. C., LERESCHE, N. & CRUNELLI, V. 2013. Essential thalamic contribution to slow waves of natural sleep. *J Neurosci,* 33**,** 19599-610.

DECO, G., PONCE-ALVAREZ, A., HAGMANN, P., ROMANI, G. L., MANTINI, D. & CORBETTA, M. 2014. How local excitation-inhibition ratio impacts the whole brain dynamics. *J Neurosci,* 34**,** 7886-98.

DESTEXHE, A., CONTRERAS, D. & STERIADE, M. 1999. Spatiotemporal Analysis of Local Field Potentials and Unit Discharges in Cat Cerebral Cortex during Natural Wake and Sleep States. *J Neurosci,* 19**,** 4595-4608.

DEVOR, A., DUNN, A. K., ANDERMANN, M. L., ULBERT, I., BOAS, D. A. & DALE, A. M. 2003. Coupling of Total Hemoglobin Concentration, Oxygenation, and Neural Activity in Rat Somatosensory Cortex. *Neuron,* 39**,** 353-359.

DIJKHUIZEN, R. M., ZAHARCHUK, G. & OTTE, W. M. 2014. Assessment and modulation of resting-state neural networks after stroke. *Curr Opin Neurol,* 27**,** 637-43.

DOI, A., MIZUNO, M., KATAFUCHI, T., FURUE, H., KOGA, K. & YOSHIMURA, M. 2007. Slow oscillation of membrane currents mediated by glutamatergic inputs of rat somatosensory cortical neurons: in vivo patch-clamp analysis. *Eur J Neurosci,* 26**,** 2565-75.

DUFF, E. P., MAKIN, T., COTTAAR, M., SMITH, S. M. & WOOLRICH, M. W. 2018. Disambiguating brain functional connectivity. *Neuroimage,* 173**,** 540-550.

EBNER, C., LEDDEROSE, J., ZOLNIK, T. A., DOMINIAK, S. E., TURKO, P., PAPOUTSI, A., POIRAZI, P., EICKHOLT, B. J., VIDA, I., LARKUM, M. E. & SACHDEV, R. N. S. 2019. Optically Induced Calcium-Dependent Gene Activation and Labeling of Active Neurons Using CaMPARI and Cal-Light. *Front Synaptic Neurosci,* 11**,** 16.

ENGLOT, D. J., KONRAD, P. E. & MORGAN, V. L. 2016. Regional and global connectivity disturbances in focal epilepsy, related neurocognitive sequelae, and potential mechanistic underpinnings. *Epilepsia,* 57**,** 1546-1557.

EWERT, T. A., VAHLE-HINZ, C. & ENGEL, A. K. 2008. High-frequency whisker vibration is encoded by phase-locked responses of neurons in the rat's barrel cortex. *J Neurosci,* 28**,** 5359-68.

FARRELL, J. S., NGUYEN, Q.-A. & SOLTESZ, I. 2019. Resolving the Micro-Macro Disconnect to Address Core Features of Seizure Networks. *Neuron,* 101**,** 1016-1028.

FEREZOU, I. & DENEUX, T. 2017. Review: How do spontaneous and sensory-evoked activities interact? *Neurophotonics,* 4**,** 031221.

FEREZOU, I., HAISS, F., GENTET, L. J., ARONOFF, R., WEBER, B. & PETERSEN, C. C. 2007. Spatiotemporal dynamics of cortical sensorimotor integration in behaving mice. *Neuron,* 56**,** 907-23.

FONTANINI, A., SPANO, P. & BOWER, J. M. 2003. Ketamine-Xylazine-Induced Slow (< 1.5 Hz) Oscillations in the Rat Piriform (Olfactory) Cortex Are Functionally Correlated with Respiration. *The Journal of Neuroscience,* 23**,** 7993-8001.

FOX, M. D. & GREICIUS, M. 2010. Clinical applications of resting state functional connectivity. *Front Syst Neurosci,* 4**,** 19.

FOX, M. D. & RAICHLE, M. E. 2007. Spontaneous fluctuations in brain activity observed with functional magnetic resonance imaging. *Nat Rev Neurosci,* 8**,** 700-11.

FOX, M. D., ZHANG, D., SNYDER, A. Z. & RAICHLE, M. E. 2009. The global signal and observed anticorrelated resting state brain networks. *J Neurophysiol,* 101**,** 3270-83.

FRANKLIN, K. B. J. & PAXINOS, G. 2012. *The Mouse Brain in Stereotactic Coordinates,* New York, Academic Press.

FULTZ, N. E., BONMASSAR, G., SETSOMPOP, K., STICKGOLD, R. A., ROSEN, B. R., POLIMENI, J. R. & LEWIS, L. D. 2019. Coupled electrophysiological, hemodynamic, and cerebrospinal fluid oscillations in human sleep. *Science,* 366**,** 628-631.

FUNK, C. M., PEELMAN, K., BELLESI, M., MARSHALL, W., CIRELLI, C. & TONONI, G. 2017. Role of Somatostatin-Positive Cortical Interneurons in the Generation of Sleep Slow Waves. *J Neurosci,* 37**,** 9132-9148.

GAO, L., MENG, X., YE, C., ZHANG, H., LIU, C., DAN, Y., POO, M. M., HE, J. & ZHANG, X. 2009. Entrainment of slow oscillations of auditory thalamic neurons by repetitive sound stimuli. *J Neurosci,* 29**,** 6013-21.

GAO, Y. R., MA, Y., ZHANG, Q., WINDER, A. T., LIANG, Z., ANTINORI, L., DREW, P. J. & ZHANG, N. 2017. Time to wake up: Studying neurovascular coupling and brain-wide circuit function in the un-anesthetized animal. *Neuroimage,* 153**,** 382-398.

GIORGI, A., MIGLIARINI, S., GALBUSERA, A., MADDALONI, G., MEREU, M., MARGIANI, G., GRITTI, M., LANDI, S., TROVATO, F., BERTOZZI, S. M., ARMIROTTI, A., RATTO, G. M., DE LUCA, M. A., TONINI, R., GOZZI, A. & PASQUALETTI, M. 2017. Brain-wide Mapping of Endogenous Serotonergic Transmission via Chemogenetic fMRI. *Cell Rep,* 21**,** 910-918.

GOLLO, L. L., ROBERTS, J. A. & COCCHI, L. 2017. Mapping how local perturbations influence systems-level brain dynamics. *Neuroimage,* 160**,** 97-112.

GREENBERG, A., ABADCHI, J. K., DICKSON, C. T. & MOHAJERANI, M. H. 2018. New waves: Rhythmic electrical field stimulation systematically alters spontaneous slow dynamics across mouse neocortex. *Neuroimage,* 174**,** 328-339.

GREFKES, C. & FINK, G. R. 2011. Reorganization of cerebral networks after stroke: new insights from neuroimaging with connectivity approaches. *Brain,* 134**,** 1264-76.

GRINVALD, A., LIEKE, E., FROSTIG, R. D., GILBERT, C. D. & WIESEL, T. N. 1986. Functional architecture of cortex revealed by optical imaging of intrinsic signals. *Nature,* 324**,** 361-4.

GUEVARA, E., PIERRE, W. C., TESSIER, C., AKAKPO, L., LONDONO, I., LESAGE, F. & LODYGENSKY, G. A. 2017. Altered Functional Connectivity Following an Inflammatory White Matter Injury in the Newborn Rat: A High Spatial and Temporal Resolution Intrinsic Optical Imaging Study. *Front Neurosci,* 11**,** 358.

HABLITZ, L. M., VINITSKY, H. S., SUN, Q., STAEGER, F. F., SIGURDSSON, B., MORTENSEN, K. N., LILIUS, T. O. & NEDERGAARD, M. 2019. Increased glymphatic influx is correlated with high EEG delta power and low heart rate in mice under anesthesia. *Sci Adv,* 5**,** eaav5447.

HAKON, J., QUATTROMANI, M. J., SJOLUND, C., TOMASEVIC, G., CAREY, L., LEE, J. M., RUSCHER, K., WIELOCH, T. & BAUER, A. Q. 2018. Multisensory stimulation improves functional recovery and resting-state functional connectivity in the mouse brain after stroke. *Neuroimage Clin,* 17**,** 717-730.

HAN, F., CAPORALE, N. & DAN, Y. 2008. Reverberation of recent visual experience in spontaneous cortical waves. *Neuron,* 60**,** 321-7.

HARTINGS, J. A., TEMEREANCA, S. & SIMONS, D. J. 2003. Processing of periodic whisker deflections by neurons in the ventroposterior medial and thalamic reticular nuclei. *J Neurophysiol,* 90**,** 3087-94.

HE, B. J., SNYDER, A. Z., ZEMPEL, J. M., SMYTH, M. D. & RAICHLE, M. E. 2008. Electrophysiological correlates of the brain's intrinsic large-scale functional architecture. *Proc Natl Acad Sci U S A,* 105**,** 16039-44.

HE, J. 2003. Slow Oscillation in Non-Lemniscal Auditory Thalamus. *The Journal of Neuroscience,* 23**,** 8281-8290.

HE, Y., WANG, M., CHEN, X., POHMANN, R., POLIMENI, J. R., SCHEFFLER, K., ROSEN, B. R., KLEINFELD, D. & YU, X. 2018. Ultra-Slow Single-Vessel BOLD and CBV-Based fMRI Spatiotemporal Dynamics and Their Correlation with Neuronal Intracellular Calcium Signals. *Neuron,* 97**,** 925-939 e5.

HENSCH, T. K. 2005. Critical period plasticity in local cortical circuits. *Nat Rev Neurosci,* 6**,** 877-88.

HISHINUMA, A. K., GULATI, T., BURISH, M. J. & GANGULY, K. 2019. Large-scale changes in cortical dynamics triggered by repetitive somatosensory electrical stimulation. *J Neuroeng Rehabil,* 16**,** 59.

HOFFMAN, K. L., BATTAGLIA, F. P., HARRIS, K., MACLEAN, J. N., MARSHALL, L. & MEHTA, M. R. 2007. The upshot of up states in the neocortex: from slow oscillations to memory formation. *J Neurosci,* 27**,** 11838-41.

HRVATIN, S., TZENG, C. P., NAGY, M. A., STROUD, H., KOUTSIOUMPA, C., WILCOX, O. F., ASSAD, E. G., GREEN, J., HARVEY, C. D., GRIFFITH, E. C. & GREENBERG, M. E. 2019. wA scalable platform for the development of cell-type-specific viral drivers. *Elife,* 8.

HSIEH, T. H., LEE, H. H. C., HAMEED, M. Q., PASCUAL-LEONE, A., HENSCH, T. K. & ROTENBERG, A. 2017. Trajectory of Parvalbumin Cell Impairment and Loss of Cortical Inhibition in Traumatic Brain Injury. *Cereb Cortex,* 27**,** 5509-5524.

IORDANOVA, B., VAZQUEZ, A., KOZAI, T. D., FUKUDA, M. & KIM, S. G. 2018. Optogenetic investigation of the variable neurovascular coupling along the interhemispheric circuits. *J Cereb Blood Flow Metab,* 38**,** 627-640.

JAIME, S., CAVAZOS, J. E., YANG, Y. & LU, H. 2018. Longitudinal observations using simultaneous fMRI, multiple channel electrophysiology recording, and chemical microiontophoresis in the rat brain. *J Neurosci Methods,* 306**,** 68-76.

JIANG, X., LACHANCE, M. & ROSSIGNOL, E. 2016. Involvement of cortical fast-spiking parvalbumin-positive basket cells in epilepsy. *Prog Brain Res,* 226**,** 81-126.

JOHNSTON, J. M., VAISHNAVI, S. N., SMYTH, M. D., ZHANG, D., HE, B. J., ZEMPEL, J. M., SHIMONY, J. S., SNYDER, A. Z. & RAICHLE, M. E. 2008. Loss of resting interhemispheric functional connectivity after complete section of the corpus callosum. *J Neurosci,* 28**,** 6453-8.

KAUVAR, I. V., MACHADO, T. A., YUEN, E., KOCHALKA, J., CHOI, M., ALLEN, W. E., WETZSTEIN, G. & DEISSEROTH, K. 2020. Cortical Observation by Synchronous Multifocal Optical Sampling Reveals Widespread Population Encoding of Actions. *Neuron*.

KIM, T. H., ZHANG, Y., LECOQ, J., JUNG, J. C., LI, J., ZENG, H., NIELL, C. M. & SCHNITZER, M. J. 2016. Long-Term Optical Access to an Estimated One Million Neurons in the Live Mouse Cortex. *Cell Rep,* 17**,** 3385-3394.

KIM, Y. K., YANG, E. J., CHO, K., LIM, J. Y. & PAIK, N. J. 2014. Functional Recovery After Ischemic Stroke Is Associated With Reduced GABAergic Inhibition in the Cerebral Cortex: A GABA PET Study. *Neurorehabil Neural Repair,* 28**,** 576-83.

KIROV, R., WEISS, C., SIEBNER, H. R., BORN, J. & MARSHALL, L. 2009. Slow oscillation electrical brain stimulation during waking promotes EEG theta activity and memory encoding. *Proc Natl Acad Sci U S A,* 106**,** 15460-5.

KLEINFELD, D., LUAN, L., MITRA, P. P., ROBINSON, J. T., SARPESHKAR, R., SHEPARD, K., XIE, C. & HARRIS, T. D. 2019. Can One Concurrently Record Electrical Spikes from Every Neuron in a Mammalian Brain? *Neuron,* 103**,** 1005-1015.

KOZBERG, M. G., MA, Y., SHAIK, M. A., KIM, S. H. & HILLMAN, E. M. 2016. Rapid Postnatal Expansion of Neural Networks Occurs in an Environment of Altered Neurovascular and Neurometabolic Coupling. *J Neurosci,* 36**,** 6704-17.

KRAFT, A. W., BAUER, A. Q., CULVER, J. P. & LEE, J. M. 2018. Sensory deprivation after focal ischemia in mice accelerates brain remapping and improves functional recovery through Arc-dependent synaptic plasticity. *Sci Transl Med,* 10.

KRAFT, A. W., MITRA, A., BAUER, A. Q., SNYDER, A. Z., RAICHLE, M. E., CULVER, J. P. & LEE, J. M. 2017. Visual experience sculpts whole-cortex spontaneous infraslow activity patterns through an Arc-dependent mechanism. *Proc Natl Acad Sci U S A,* 114**,** E9952-E9961.

KRAFT, A. W., MITRA, A., ROSENTHAL, Z. P., DOSENBACH, N. U. F., BAUER, A. Q., SNYDER, A. Z., RAICHLE, M. E., CULVER, J. P. & LEE, J. M. 2020. Electrically coupled inhibitory interneurons constrain long-range connectivity of cortical networks. *Neuroimage,* 215**,** 116810.

KUBOTA, Y., KAMATANI, D., TSUKANO, H., OHSHIMA, S., TAKAHASHI, K., HISHIDA, R., KUDOH, M., TAKAHASHI, S. & SHIBUKI, K. 2008. Transcranial photo-inactivation of neural activities in the mouse auditory cortex. *Neurosci Res,* 60**,** 422-30.

KUHLMAN, S. J., OLIVAS, N. D., TRING, E., IKRAR, T., XU, X. & TRACHTENBERG, J. T. 2013. A disinhibitory microcircuit initiates critical-period plasticity in the visual cortex. *Nature,* 501**,** 543-6.

KUKI, T., OHSHIRO, T., ITO, S., JI, Z. G., FUKAZAWA, Y., MATSUZAKA, Y., YAWO, H. & MUSHIAKE, H. 2013. Frequency-dependent entrainment of neocortical slow oscillation to repeated optogenetic stimulation in the anesthetized rat. *Neurosci Res,* 75**,** 35-45.

KYRIAKATOS, A., SADASHIVAIAH, V., ZHANG, Y., MOTTA, A., AUFFRET, M. & PETERSEN, C. C. 2017. Voltage-sensitive dye imaging of mouse neocortex during a whisker detection task. *Neurophotonics,* 4**,** 031204.

LADENBAUER, J., KULZOW, N., PASSMANN, S., ANTONENKO, D., GRITTNER, U., TAMM, S. & FLOEL, A. 2016. Brain stimulation during an afternoon nap boosts slow oscillatory activity and memory consolidation in older adults. *Neuroimage,* 142**,** 311-323.

LAKATOS, P., CHEN, C. M., O'CONNELL, M. N., MILLS, A. & SCHROEDER, C. E. 2007. Neuronal oscillations and multisensory interaction in primary auditory cortex. *Neuron,* 53**,** 279-92.

LAKATOS, P., KARMOS, G., MEHTA, A. D., ULBERT, I. & SCHROEDER, C. E. 2008. Entrainment of neuronal oscillations as a mechanism of attentional selection. *Science,* 320**,** 110-3.

LECOQ, J., SAVALL, J., VUCINIC, D., GREWE, B. F., KIM, H., LI, J. Z., KITCH, L. J. & SCHNITZER, M. J. 2014. Visualizing mammalian brain area interactions by dual-axis two-photon calcium imaging. *Nat Neurosci,* 17**,** 1825-9.

LI, J. M., BENTLEY, W. J. & SNYDER, L. H. 2015. Functional connectivity arises from a slow rhythmic mechanism. *Proc Natl Acad Sci U S A,* 112**,** E2527-35.

LIEPERT, J., STORCH, P., FRITSCH, A. & WEILLER, C. 2000. Motor cortex disinhibition in acute stroke. *Clinical Neurophysiology,* 111**,** 671-676.

LIM, D. H., LEDUE, J. M., MOHAJERANI, M. H. & MURPHY, T. H. 2014. Optogenetic mapping after stroke reveals network-wide scaling of functional connections and heterogeneous recovery of the peri-infarct. *J Neurosci,* 34**,** 16455-66.

LIN, M. Z. & SCHNITZER, M. J. 2016. Genetically encoded indicators of neuronal activity. *Nat Neurosci,* 19**,** 1142-53.

LIOU, J. Y., MA, H., WENZEL, M., ZHAO, M., BAIRD-DANIEL, E., SMITH, E. H., DANIEL, A., EMERSON, R., YUSTE, R., SCHWARTZ, T. H. & SCHEVON, C. A. 2018. Role of inhibitory control in modulating focal seizure spread. *Brain,* 141**,** 2083-2097.

LIU, J., ZHANG, M. Q., WU, X., LAZARUS, M., CHERASSE, Y., YUAN, M. Y., HUANG, Z. L. & LI, R. X. 2017. Activation of Parvalbumin Neurons in the Rostro-Dorsal Sector of the Thalamic Reticular Nucleus Promotes Sensitivity to Pain in Mice. *Neuroscience,* 366**,** 113-123.

LIU, X., DE ZWART, J. A., SCHOLVINCK, M. L., CHANG, C., YE, F. Q., LEOPOLD, D. A. & DUYN, J. H. 2018. Subcortical evidence for a contribution of arousal to fMRI studies of brain activity. *Nat Commun,* 9**,** 395.

LUCZAK, A., BARTHO, P. & HARRIS, K. D. 2013. Gating of sensory input by spontaneous cortical activity. *J Neurosci,* 33**,** 1684-95.

LUCZAK, A., BARTHO, P., MARGUET, S. L., BUZSAKI, G. & HARRIS, K. D. 2007. Sequential structure of neocortical spontaneous activity in vivo. *Proc Natl Acad Sci U S A,* 104**,** 347-52.

MA, Y., MA, Z., LIANG, Z., NEUBERGER, T. & ZHANG, N. 2020. Global brain signal in awake rats. *Brain Struct Funct,* 225**,** 227-240.

MA, Y., SHAIK, M. A., KIM, S. H., KOZBERG, M. G., THIBODEAUX, D. N., ZHAO, H. T., YU, H. & HILLMAN, E. M. 2016a. Wide-field optical mapping of neural activity and brain haemodynamics: considerations and novel approaches. *Philos Trans R Soc Lond B Biol Sci,* 371.

MA, Y., SHAIK, M. A., KOZBERG, M. G., KIM, S. H., PORTES, J. P., TIMERMAN, D. & HILLMAN, E. M. 2016b. Resting-state hemodynamics are spatiotemporally coupled to synchronized and symmetric neural activity in excitatory neurons. *Proc Natl Acad Sci U S A,* 113**,** E8463-E8471.

MACLEAN, J. N., WATSON, B. O., AARON, G. B. & YUSTE, R. 2005. Internal dynamics determine the cortical response to thalamic stimulation. *Neuron,* 48**,** 811-23.

MAFFEI, A., NATARAJ, K., NELSON, S. B. & TURRIGIANO, G. G. 2006. Potentiation of cortical inhibition by visual deprivation. *Nature,* 443**,** 81-4.

MAO, T., KUSEFOGLU, D., HOOKS, B. M., HUBER, D., PETREANU, L. & SVOBODA, K. 2011. Long-range neuronal circuits underlying the interaction between sensory and motor cortex. *Neuron,* 72**,** 111-23.

MARSHALL, L., HELGADOTTIR, H., MOLLE, M. & BORN, J. 2006. Boosting slow oscillations during sleep potentiates memory. *Nature,* 444**,** 610-3.

MARVIN, J. S., BORGHUIS, B. G., TIAN, L., CICHON, J., HARNETT, M. T., AKERBOOM, J., GORDUS, A., RENNINGER, S. L., CHEN, T. W., BARGMANN, C. I., ORGER, M. B., SCHREITER, E. R., DEMB, J. B., GAN, W. B., HIRES, S. A. & LOOGER, L. L. 2013. An optimized fluorescent probe for visualizing glutamate neurotransmission. *Nat Methods,* 10**,** 162-70.

MASSIMINI, M., FERRARELLI, F., ESSER, S. K., RIEDNER, B. A., HUBER, R., MURPHY, M., PETERSON, M. J. & TONONI, G. 2007. Triggering sleep slow waves by transcranial magnetic stimulation. *Proc Natl Acad Sci U S A,* 104**,** 8496-501.

MASSIMINI, M., HUBER, R., FERRARELLI, F., HILL, S. & TONONI, G. 2004. The sleep slow oscillation as a traveling wave. *J Neurosci,* 24**,** 6862-70.

MAXWELL, K. A. & DYCK, R. H. 2005. Induction of reproducible focal ischemic lesions in neonatal mice by photothrombosis. *Dev Neurosci,* 27**,** 121-6.

MEGEVAND, P., TRONCOSO, E., QUAIRIAUX, C., MULLER, D., MICHEL, C. M. & KISS, J. Z. 2009. Long-term plasticity in mouse sensorimotor circuits after rhythmic whisker stimulation. *J Neurosci,* 29**,** 5326-35.

MICHELSON, N. J., VANNI, M. P. & MURPHY, T. H. 2019. Comparison between transgenic and AAV-PHP.eB-mediated expression of GCaMP6s using in vivo wide-field functional imaging of brain activity. *Neurophotonics,* 6**,** 025014.

MISHRA, A. M., BAI, X., SANGANAHALLI, B. G., WAXMAN, S. G., SHATILLO, O., GROHN, O., HYDER, F., PITKANEN, A. & BLUMENFELD, H. 2014. Decreased resting functional connectivity after traumatic brain injury in the rat. *PLoS One,* 9**,** e95280.

MITRA, A., KRAFT, A., WRIGHT, P., ACLAND, B., SNYDER, A. Z., ROSENTHAL, Z., CZERNIEWSKI, L., BAUER, A., SNYDER, L., CULVER, J., LEE, J. M. & RAICHLE, M. E. 2018. Spontaneous Infra-slow Brain Activity Has Unique Spatiotemporal Dynamics and Laminar Structure. *Neuron,* 98**,** 297-305 e6.

MITRA, A., SNYDER, A. Z., BLAZEY, T. & RAICHLE, M. E. 2015a. Lag threads organize the brain's intrinsic activity. *Proc Natl Acad Sci U S A,* 112**,** E2235-44.

MITRA, A., SNYDER, A. Z., HACKER, C. D., PAHWA, M., TAGLIAZUCCHI, E., LAUFS, H., LEUTHARDT, E. C. & RAICHLE, M. E. 2016. Human cortical-hippocampal dialogue in wake and slow-wave sleep. *Proc Natl Acad Sci U S A,* 113**,** E6868-E6876.

MITRA, A., SNYDER, A. Z., TAGLIAZUCCHI, E., LAUFS, H. & RAICHLE, M. E. 2015b. Propagated infra-slow intrinsic brain activity reorganizes across wake and slow wave sleep. *Elife,* 4.

MITRA, P. P. & PESARAN, B. 1999a. Analysis of dynamic brain imaging data. *Biophys J,* 76**,** 691-708.

MITRA, P. P. & PESARAN, B. 1999b. Analysis of Dynamic Brain Imaging Data. *Biophysical Journal,* 76**,** 691-708.

MOEYAERT, B., HOLT, G., MADANGOPAL, R., PEREZ-ALVAREZ, A., FEAREY, B. C., TROJANOWSKI, N. F., LEDDEROSE, J., ZOLNIK, T. A., DAS, A., PATEL, D., BROWN, T. A., SACHDEV, R. N. S., EICKHOLT, B. J., LARKUM, M. E., TURRIGIANO, G. G., DANA, H., GEE, C. E., OERTNER, T. G., HOPE, B. T. & SCHREITER, E. R. 2018. Improved methods for marking active neuron populations. *Nat Commun,* 9**,** 4440.

MOHAJERANI, M. H., CHAN, A. W., MOHSENVAND, M., LEDUE, J., LIU, R., MCVEA, D. A., BOYD, J. D., WANG, Y. T., REIMERS, M. & MURPHY, T. H. 2013. Spontaneous cortical activity alternates between motifs defined by regional axonal projections. *Nat Neurosci,* 16**,** 1426-35.

MOHAJERANI, M. H., MCVEA, D. A., FINGAS, M. & MURPHY, T. H. 2010. Mirrored bilateral slow-wave cortical activity within local circuits revealed by fast bihemispheric voltage-sensitive dye imaging in anesthetized and awake mice. *J Neurosci,* 30**,** 3745-51.

MONAKHOV, M. V., MATLASHOV, M. E., COLAVITA, M., SONG, C., SHCHERBAKOVA, D. M., ANTIC, S. D., VERKHUSHA, V. V. & KNÖPFEL, T. 2019.

MOORE, A. K., WEIBLE, A. P., BALMER, T. S., TRUSSELL, L. O. & WEHR, M. 2018. Rapid Rebalancing of Excitation and Inhibition by Cortical Circuitry. *Neuron,* 97**,** 1341-1355 e6.

MOORE, J. J., RAVASSARD, P. M., HO, D., ACHARYA, L., KEES, A. L., VUONG, C. & MEHTA, M. R. 2017. Dynamics of cortical dendritic membrane potential and spikes in freely behaving rats. *Science,* 355.

MURPHY, M., RIEDNER, B. A., HUBER, R., MASSIMINI, M., FERRARELLI, F. & TONONI, G. 2009. Source modeling sleep slow waves. *Proc Natl Acad Sci U S A,* 106**,** 1608-13.

MURPHY, M. C., CHAN, K. C., KIM, S. G. & VAZQUEZ, A. L. 2018. Macroscale variation in resting-state neuronal activity and connectivity assessed by simultaneous calcium imaging, hemodynamic imaging and electrophysiology. *Neuroimage,* 169**,** 352-362.

MUSALL, S., KAUFMAN, M. T., JUAVINETT, A. L., GLUF, S. & CHURCHLAND, A. K. 2019. Single-trial neural dynamics are dominated by richly varied movements. *Nat Neurosci,* 22**,** 1677-1686.

NAKAMURA, Y., NAKAMURA, Y., PELOSI, A., DJEMAI, B., DEBACKER, C., HERVE, D., GIRAULT, J. A. & TSURUGIZAWA, T. 2020. fMRI detects bilateral brain network activation following unilateral chemogenetic activation of direct striatal projection neurons. *Neuroimage,* 220**,** 117079.

NARIKIYO, K., MIZUGUCHI, R., AJIMA, A., SHIOZAKI, M., HAMANAKA, H., JOHANSEN, J. P., MORI, K. & YOSHIHARA, Y. 2020. The claustrum coordinates cortical slow-wave activity. *Nat Neurosci,* 23**,** 741-753.

NESKE, G. T. 2015. The Slow Oscillation in Cortical and Thalamic Networks: Mechanisms and Functions. *Front Neural Circuits,* 9**,** 88.

NGO, H. V., MARTINETZ, T., BORN, J. & MOLLE, M. 2013. Auditory closed-loop stimulation of the sleep slow oscillation enhances memory. *Neuron,* 78**,** 545-53.

NGUYEN, R., MORRISSEY, M. D., MAHADEVAN, V., CAJANDING, J. D., WOODIN, M. A., YEOMANS, J. S., TAKEHARA-NISHIUCHI, K. & KIM, J. C. 2014. Parvalbumin and GAD65 interneuron inhibition in the ventral hippocampus induces distinct behavioral deficits relevant to schizophrenia. *J Neurosci,* 34**,** 14948-60.

NIR, Y., MUKAMEL, R., DINSTEIN, I., PRIVMAN, E., HAREL, M., FISCH, L., GELBARD-SAGIV, H., KIPERVASSER, S., ANDELMAN, F., NEUFELD, M. Y., KRAMER, U., ARIELI, A., FRIED, I. & MALACH, R. 2008. Interhemispheric correlations of slow spontaneous neuronal fluctuations revealed in human sensory cortex. *Nat Neurosci,* 11**,** 1100-8.

NIR, Y., STABA, R. J., ANDRILLON, T., VYAZOVSKIY, V. V., CIRELLI, C., FRIED, I. & TONONI, G. 2011. Regional slow waves and spindles in human sleep. *Neuron,* 70**,** 153-69.

O'HASHI, K., FEKETE, T., DENEUX, T., HILDESHEIM, R., VAN LEEUWEN, C. & GRINVALD, A. 2018. Interhemispheric Synchrony of Spontaneous Cortical States at the Cortical Column Level. *Cereb Cortex,* 28**,** 1794-1807.

OISHI, Y., XU, Q., WANG, L., ZHANG, B. J., TAKAHASHI, K., TAKATA, Y., LUO, Y. J., CHERASSE, Y., SCHIFFMANN, S. N., DE KERCHOVE D'EXAERDE, A., URADE, Y., QU, W. M., HUANG, Z. L. & LAZARUS, M. 2017. Slow-wave sleep is controlled by a subset of nucleus accumbens core neurons in mice. *Nat Commun,* 8**,** 734.

OMER, D. B., FEKETE, T., ULCHIN, Y., HILDESHEIM, R. & GRINVALD, A. 2019. Dynamic Patterns of Spontaneous Ongoing Activity in the Visual Cortex of Anesthetized and Awake Monkeys are Different. *Cereb Cortex,* 29**,** 1291-1304.

ORUKARI, I. E., SIEGEL, J. S., WARRINGTON, N. M., BAXTER, G. A., BAUER, A. Q., SHIMONY, J. S., RUBIN, J. B. & CULVER, J. P. 2020. Altered hemodynamics contribute to local but not remote functional connectivity disruption due to glioma growth. *J Cereb Blood Flow Metab,* 40**,** 100-115.

OYANEDEL, C. N., DURAN, E., NIETHARD, N., INOSTROZA, M. & BORN, J. 2020. Temporal associations between sleep slow oscillations, spindles and ripples. *Eur J Neurosci*.

PALA, A. & PETERSEN, C. C. 2018. State-dependent cell-type-specific membrane potential dynamics and unitary synaptic inputs in awake mice. *Elife,* 7**,** 1-13.

PAN, W. J., THOMPSON, G. J., MAGNUSON, M. E., JAEGER, D. & KEILHOLZ, S. 2013. Infraslow LFP correlates to resting-state fMRI BOLD signals. *Neuroimage,* 74**,** 288-97.

PEETERS, L. M., HINZ, R., DETREZ, J. R., MISSAULT, S., DE VOS, W. H., VERHOYE, M., VAN DER LINDEN, A. & KELIRIS, G. A. 2020. Chemogenetic silencing of neurons in the mouse anterior cingulate area modulates neuronal activity and functional connectivity. *Neuroimage,* 220**,** 117088.

PESARAN, B., VINCK, M., EINEVOLL, G. T., SIROTA, A., FRIES, P., SIEGEL, M., TRUCCOLO, W., SCHROEDER, C. E. & SRINIVASAN, R. 2018. Investigating large-scale brain dynamics using field potential recordings: analysis and interpretation. *Nat Neurosci,* 21**,** 903-919.

PETERSEN, C. C., HAHN, T. T., MEHTA, M., GRINVALD, A. & SAKMANN, B. 2003. Interaction of sensory responses with spontaneous depolarization in layer 2/3 barrel cortex. *Proc Natl Acad Sci U S A,* 100**,** 13638-43.

PETRUS, E., SAAR, G., MA, Z., DODD, S., ISAAC, J. T. R. & KORETSKY, A. P. 2019. Interhemispheric plasticity is mediated by maximal potentiation of callosal inputs. *Proc Natl Acad Sci U S A*.

PORYAZOVA, R., HUBER, R., KHATAMI, R., WERTH, E., BRUGGER, P., BARATH, K., BAUMANN, C. R. & BASSETTI, C. L. 2015. Topographic sleep EEG changes in the acute and chronic stage of hemispheric stroke. *J Sleep Res,* 24**,** 54-65.

PRECHTL, J. C., COHEN, L. B., PESARAN, B., MITRA, P. P. & KLEINFELD, D. 1997. Visual stimuli induce waves of electrical activity in turtle cortex. *Proc Natl Acad Sci U S A,* 94**,** 7621-6.

QUATTROMANI, M. J., HAKON, J., RAUCH, U., BAUER, A. Q. & WIELOCH, T. 2018. Changes in resting-state functional connectivity after stroke in a mouse brain lacking extracellular matrix components. *Neurobiol Dis,* 112**,** 91-105.

RANGANATHAN, G. N., APOSTOLIDES, P. F., HARNETT, M. T., XU, N. L., DRUCKMANN, S. & MAGEE, J. C. 2018. Active dendritic integration and mixed neocortical network representations during an adaptive sensing behavior. *Nat Neurosci,* 21**,** 1583-1590.

RAUT, R. V., MITRA, A., MAREK, S., ORTEGA, M., SNYDER, A. Z., TANENBAUM, A., LAUMANN, T. O., DOSENBACH, N. U. F. & RAICHLE, M. E. 2020. Organization of Propagated Intrinsic Brain Activity in Individual Humans. *Cereb Cortex,* 30**,** 1716-1734.

RIEDNER, B. A., HULSE, B. K., MURPHY, M. J., FERRARELLI, F. & TONONI, G. 2011. Temporal dynamics of cortical sources underlying spontaneous and peripherally evoked slow waves. *Prog Brain Res,* 193**,** 201-18.

ROCK, C., ZURITA, H., LEBBY, S., WILSON, C. J. & APICELLA, A. J. 2017. Cortical Circuits of Callosal GABAergic Neurons. *Cereb Cortex***,** 1-14.

ROELOFS, T. J. M., VERHAREN, J. P. H., VAN TILBORG, G. A. F., BOEKHOUDT, L., VAN DER TOORN, A., DE JONG, J. W., LUIJENDIJK, M. C. M., OTTE, W. M., ADAN, R. A. H. & DIJKHUIZEN, R. M. 2017. A novel approach to map induced activation of neuronal networks using chemogenetics and functional neuroimaging in rats: A proof-of-concept study on the mesocorticolimbic system. *Neuroimage,* 156**,** 109-118.

ROLAND, J. L., SNYDER, A. Z., HACKER, C. D., MITRA, A., SHIMONY, J. S., LIMBRICK, D. D., RAICHLE, M. E., SMYTH, M. D. & LEUTHARDT, E. C. 2017.

On the role of the corpus callosum in interhemispheric functional connectivity in humans. *Proc Natl Acad Sci U S A,* 114**,** 13278-13283.

ROSENTHAL, Z. P. Recovery of Cortical Delta Band Functional Connectivity after Stroke. Society for Neuroscience Meeting, 2017 Washington D.C.

ROSENTHAL, Z. P., RAUT, R. V., YAN, P., KOKO, D., KRAFT, A. W., CZERNIEWSKI, L., ACLAND, B., MITRA, A., SNYDER, L. H., BAUER, A. Q., SNYDER, A. Z., CULVER, J. P., RAICHLE, M. E. & LEE, J. M. 2020. Local Perturbations of Cortical Excitability Propagate Differentially Through Large-Scale Functional Networks. *Cereb Cortex,* 30**,** 3352-3369.

ROSSI, L. F., WYKES, R. C., KULLMANN, D. M. & CARANDINI, M. 2017. Focal cortical seizures start as standing waves and propagate respecting homotopic connectivity. *Nat Commun,* 8**,** 217.

ROTH, B. L. 2016. DREADDs for Neuroscientists. *Neuron,* 89**,** 683-94.

SACHIDHANANDAM, S., SERMET, B. S. & PETERSEN, C. C. H. 2016. Parvalbumin-Expressing GABAergic Neurons in Mouse Barrel Cortex Contribute to Gating a Goal-Directed Sensorimotor Transformation. *Cell Rep,* 15**,** 700-706.

SANCHEZ-VIVES, M. V. & MCCORMICK, D. A. 2000. Cellular and network mechanisms of rhythmic recurrent activity in neocortex. *Nat Neurosci,* 3**,** 1027-34.

SARASSO, S., D’AMBROSIO, S., FECCHIO, M., CASAROTTO, S., VIGANÒ, A., LANDI, C., MATTAVELLI, G., GOSSERIES, O., QUARENGHI, M., LAUREYS, S., DEVALLE, G., ROSANOVA, M. & MASSIMINI, M. 2020. Local sleep-like cortical reactivity in the awake brain after focal injury. *bioRxiv. doi: 10.1101/2019.12.19.882290*.

SARASSO, S., MAATTA, S., FERRARELLI, F., PORYAZOVA, R., TONONI, G. & SMALL, S. L. 2014. Plastic changes following imitation-based speech and language therapy for aphasia: a high-density sleep EEG study. *Neurorehabil Neural Repair,* 28**,** 129-38.

SHEMESH, O. A., LINGHU, C., PIATKEVICH, K. D., GOODWIN, D., CELIKER, O. T., GRITTON, H. J., ROMANO, M. F., GAO, R., YU, C. J., TSENG, H. A., BENSUSSEN, S., NARAYAN, S., YANG, C. T., FREIFELD, L., SICILIANO, C. A., GUPTA, I., WANG, J., PAK, N., YOON, Y. G., ULLMANN, J. F. P., GUNER-ATAMAN, B., NOAMANY, H., SHEINKOPF, Z. R., PARK, W. M., ASANO, S., KEATING, A. E., TRIMMER, J. S., REIMER, J., TOLIAS, A. S., BEAR, M. F., TYE, K. M., HAN, X., AHRENS, M. B. & BOYDEN, E. S. 2020. Precision Calcium Imaging of Dense Neural Populations via a Cell-Body-Targeted Calcium Indicator. *Neuron*.

SHEROZIYA, M. & TIMOFEEV, I. 2014. Global intracellular slow-wave dynamics of the thalamocortical system. *J Neurosci,* 34**,** 8875-93.

SHIGEMATSU, N., NISHI, A. & FUKUDA, T. 2019. Gap Junctions Interconnect Different Subtypes of Parvalbumin-Positive Interneurons in Barrels and Septa with Connectivity Unique to Each Subtype. *Cereb Cortex,* 29**,** 1414-1429.

SHIMAOKA, D., STEINMETZ, N. A., HARRIS, K. D. & CARANDINI, M. 2019. The impact of bilateral ongoing activity on evoked responses in mouse cortex. *Elife,* 8.

SILASI, G. & MURPHY, T. H. 2014. Stroke and the connectome: how connectivity guides therapeutic intervention. *Neuron,* 83**,** 1354-68.

SILASI, G., XIAO, D., VANNI, M. P., CHEN, A. C. & MURPHY, T. H. 2016. Intact skull chronic windows for mesoscopic wide-field imaging in awake mice. *J Neurosci Methods,* 267**,** 141-9.

SNYDER, A. Z. & BAUER, A. Q. 2019. Mapping Structure-Function Relationships in the Brain. *Biol Psychiatry Cogn Neurosci Neuroimaging,* 4**,** 510-521.

SOFRONIEW, N. J., FLICKINGER, D., KING, J. & SVOBODA, K. 2016. A large field of view two-photon mesoscope with subcellular resolution for in vivo imaging. *Elife,* 5.

SOHAL, V. S., ZHANG, F., YIZHAR, O. & DEISSEROTH, K. 2009. Parvalbumin neurons and gamma rhythms enhance cortical circuit performance. *Nature,* 459**,** 698-702.

SREENIVASAN, V., ESMAEILI, V., KIRITANI, T., GALAN, K., CROCHET, S. & PETERSEN, C. C. H. 2016. Movement Initiation Signals in Mouse Whisker Motor Cortex. *Neuron,* 92**,** 1368-1382.

STARESINA, B. P., BERGMANN, T. O., BONNEFOND, M., VAN DER MEIJ, R., JENSEN, O., DEUKER, L., ELGER, C. E., AXMACHER, N. & FELL, J. 2015. Hierarchical nesting of slow oscillations, spindles and ripples in the human hippocampus during sleep. *Nat Neurosci,* 18**,** 1679-1686.

STEDEHOUDER, J., BRIZEE, D., SHPAK, G. & KUSHNER, S. A. 2018. Activity-Dependent Myelination of Parvalbumin Interneurons Mediated by Axonal Morphological Plasticity. *J Neurosci,* 38**,** 3631-3642.

STEINMETZ, N. A., BUETFERING, C., LECOQ, J., LEE, C. R., PETERS, A. J., JACOBS, E. A. K., COEN, P., OLLERENSHAW, D. R., VALLEY, M. T., DE VRIES, S. E. J., GARRETT, M., ZHUANG, J., GROBLEWSKI, P. A., MANAVI, S., MILES, J., WHITE, C., LEE, E., GRIFFIN, F., LARKIN, J. D., ROLL, K., CROSS, S., NGUYEN, T. V., LARSEN, R., PENDERGRAFT, J., DAIGLE, T., TASIC, B., THOMPSON, C. L., WATERS, J., OLSEN, S., MARGOLIS, D. J., ZENG, H., HAUSSER, M., CARANDINI, M. & HARRIS, K. D. 2017. Aberrant Cortical Activity in Multiple GCaMP6-Expressing Transgenic Mouse Lines. *eNeuro,* 4.

STEINMETZ, N. A., ZATKA-HAAS, P., CARANDINI, M. & HARRIS, K. D. 2019. Distributed coding of choice, action and engagement across the mouse brain. *Nature,* 576**,** 266-273.

STERIADE, M., NUNEZ, A. & AMZICA, F. 1993a. Intracellular analysis of relations between the slow (< 1 Hz) neocortical oscillation and other sleep rhythms of the electroencephalogram. *J Neurosci,* 13**,** 3266-3283.

STERIADE, M., NUNEZ, A. & AMZICA, F. 1993b. A novel slow (< 1 Hz) oscillation of neocortical neurons in vivo: depolarizing and hyperpolarizing components. *J Neurosci,* 13**,** 3252-3265.

STIRMAN, J. N., SMITH, I. T., KUDENOV, M. W. & SMITH, S. L. 2016. Wide field-of-view, multi-region, two-photon imaging of neuronal activity in the mammalian brain. *Nat Biotechnol,* 34**,** 857-62.

STRINGER, C., PACHITARIU, M., STEINMETZ, N., REDDY, C. B., CARANDINI, M. & HARRIS, K. D. 2019. Spontaneous behaviors drive multidimensional, brainwide activity. *Science,* 364**,** 255.

STROH, A., ADELSBERGER, H., GROH, A., RUHLMANN, C., FISCHER, S., SCHIERLOH, A., DEISSEROTH, K. & KONNERTH, A. 2013. Making waves: initiation and propagation of corticothalamic Ca2+ waves in vivo. *Neuron,* 77**,** 1136-50.

SUN, Y., IKRAR, T., DAVIS, M. F., GONG, N., ZHENG, X., LUO, Z. D., LAI, C., MEI, L., HOLMES, T. C., GANDHI, S. P. & XU, X. 2016. Neuregulin-1/ErbB4 Signaling Regulates Visual Cortical Plasticity. *Neuron,* 92**,** 160-173.

SUN, Y., NERN, A., FRANCONVILLE, R., DANA, H., SCHREITER, E. R., LOOGER, L. L., SVOBODA, K., KIM, D. S., HERMUNDSTAD, A. M. & JAYARAMAN, V. 2017. Neural signatures of dynamic stimulus selection in Drosophila. *Nat Neurosci,* 20**,** 1104-1113.

TIMOFEEV, I., GRENIER, F., BAZHENOV, M., SEJNOWSKI, T. J. & STERIADE, M. 2000. Origin of slow cortical oscillations in deafferented cortical slabs. *Cereb Cortex,* 10**,** 1185-99.

TONONI, G. & CIRELLI, C. 2014. Sleep and the price of plasticity: from synaptic and cellular homeostasis to memory consolidation and integration. *Neuron,* 81**,** 12-34.

TSODYKS, M., KENET, T., GRINVALD, A. & ARIELI, A. 1999. Linking spontaneous activity of single cortical neurons and the underlying functional architecture. *Science,* 286**,** 1943-6.

UHLHAAS, P. J. & SINGER, W. 2012. Neuronal dynamics and neuropsychiatric disorders: toward a translational paradigm for dysfunctional large-scale networks. *Neuron,* 75**,** 963-80.

VAN MEER, M. P., VAN DER MAREL, K., WANG, K., OTTE, W. M., EL BOUAZATI, S., ROELING, T. A., VIERGEVER, M. A., BERKELBACH VAN DER SPRENKEL, J. W. & DIJKHUIZEN, R. M. 2010. Recovery of sensorimotor function after experimental stroke correlates with restoration of resting-state interhemispheric functional connectivity. *J Neurosci,* 30**,** 3964-72.

VANNI, M. P., CHAN, A. W., BALBI, M., SILASI, G. & MURPHY, T. H. 2017. Mesoscale Mapping of Mouse Cortex Reveals Frequency-Dependent Cycling between Distinct Macroscale Functional Modules. *J Neurosci,* 37**,** 7513-7533.

VANNI, M. P. & MURPHY, T. H. 2014. Mesoscale transcranial spontaneous activity mapping in GCaMP3 transgenic mice reveals extensive reciprocal connections between areas of somatomotor cortex. *J Neurosci,* 34**,** 15931-46.

VAZQUEZ, A. L., FUKUDA, M., CROWLEY, J. C. & KIM, S. G. 2014. Neural and hemodynamic responses elicited by forelimb- and photo-stimulation in channelrhodopsin-2 mice: insights into the hemodynamic point spread function. *Cereb Cortex,* 24**,** 2908-19.

VOLGUSHEV, M., CHAUVETTE, S., MUKOVSKI, M. & TIMOFEEV, I. 2006. Precise long-range synchronization of activity and silence in neocortical neurons during slow-wave oscillations [corrected]. *J Neurosci,* 26**,** 5665-72.

VORMSTEIN-SCHNEIDER, D., LIN, J. D., PELKEY, K. A., CHITTAJALLU, R., GUO, B., ARIAS-GARCIA, M. A., ALLAWAY, K., SAKOPOULOS, S., SCHNEIDER, G., STEVENSON, O., VERGARA, J., SHARMA, J., ZHANG, Q., FRANKEN, T. P., SMITH, J., IBRAHIM, L. A., KJ, M. A., SABRI, E., HUANG, S., FAVUZZI, E., BURBRIDGE, T., XU, Q., GUO, L., VOGEL, I., SANCHEZ, V., SALDI, G. A., GORISSEN, B. L., YUAN, X., ZAGHLOUL, K. A., DEVINSKY, O., SABATINI, B. L., BATISTA-BRITO, R., REYNOLDS, J., FENG, G., FU, Z., MCBAIN, C. J., FISHELL, G. & DIMIDSCHSTEIN, J. 2020. Viral manipulation of functionally distinct interneurons in mice, non-human primates and humans. *Nat Neurosci*.

WANG, X., LEONG, A. T. L., CHAN, R. W., LIU, Y. & WU, E. X. 2019. Thalamic low frequency activity facilitates resting-state cortical interhemispheric MRI functional connectivity. *Neuroimage,* 201**,** 115985.

WHITE, B. R., BAUER, A. Q., SNYDER, A. Z., SCHLAGGAR, B. L., LEE, J. M. & CULVER, J. P. 2011. Imaging of functional connectivity in the mouse brain. *PLoS One,* 6**,** e16322.

WILLIAMS, L. E. & HOLTMAAT, A. 2019. Higher-Order Thalamocortical Inputs Gate Synaptic Long-Term Potentiation via Disinhibition. *Neuron,* 101**,** 91-102 e4.

WRIGHT, P. W., ARCHAMBAULT, A. S., PEEK, S., BAUER, A. Q., CULICAN, S. M., ANCES, B. M., CULVER, J. P. & WU, G. F. 2017a. Functional connectivity alterations in a murine model of optic neuritis. *Exp Neurol,* 295**,** 18-22.

WRIGHT, P. W., BRIER, L. M., BAUER, A. Q., BAXTER, G. A., KRAFT, A. W., REISMAN, M. D., BICE, A. R., SNYDER, A. Z., LEE, J. M. & CULVER, J. P. 2017b. Functional connectivity structure of cortical calcium dynamics in anesthetized and awake mice. *PLoS One,* 12**,** e0185759.

XIAO, D., VANNI, M. P., MITELUT, C. C., CHAN, A. W., LEDUE, J. M., XIE, Y., CHEN, A. C., SWINDALE, N. V. & MURPHY, T. H. 2017. Mapping cortical mesoscopic networks of single spiking cortical or sub-cortical neurons. *Elife,* 6.

XIE, Y., CHAN, A. W., MCGIRR, A., XUE, S., XIAO, D., ZENG, H. & MURPHY, T. H. 2016. Resolution of High-Frequency Mesoscale Intracortical Maps Using the Genetically Encoded Glutamate Sensor iGluSnFR. *J Neurosci,* 36**,** 1261-72.

XU, M., CHUNG, S., ZHANG, S., ZHONG, P., MA, C., CHANG, W. C., WEISSBOURD, B., SAKAI, N., LUO, L., NISHINO, S. & DAN, Y. 2015. Basal forebrain circuit for sleep-wake control. *Nat Neurosci,* 18**,** 1641-7.

YANG, J. W., PROUVOT, P. H., REYES-PUERTA, V., STUTTGEN, M. C., STROH, A. & LUHMANN, H. J. 2017. Optogenetic Modulation of a Minor Fraction of Parvalbumin-Positive Interneurons Specifically Affects Spatiotemporal Dynamics of Spontaneous and Sensory-Evoked Activity in Mouse Somatosensory Cortex in Vivo. *Cereb Cortex,* 27**,** 5784-5803.

YANG, Y., LIU, N., HE, Y., LIU, Y., GE, L., ZOU, L., SONG, S., XIONG, W. & LIU, X. 2018. Improved calcium sensor GCaMP-X overcomes the calcium channel perturbations induced by the calmodulin in GCaMP. *Nat Commun,* 9**,** 1504.

YIZHAR, O., FENNO, L. E., PRIGGE, M., SCHNEIDER, F., DAVIDSON, T. J., O'SHEA, D. J., SOHAL, V. S., GOSHEN, I., FINKELSTEIN, J., PAZ, J. T., STEHFEST, K., FUDIM, R., RAMAKRISHNAN, C., HUGUENARD, J. R., HEGEMANN, P. & DEISSEROTH, K. 2011. Neocortical excitation/inhibition balance in information processing and social dysfunction. *Nature,* 477**,** 171-8.

ZAGHA, E., CASALE, A. E., SACHDEV, R. N., MCGINLEY, M. J. & MCCORMICK, D. A. 2013. Motor cortex feedback influences sensory processing by modulating network state. *Neuron,* 79**,** 567-78.

ZEILER, S. R., GIBSON, E. M., HOESCH, R. E., LI, M. Y., WORLEY, P. F., O'BRIEN, R. J. & KRAKAUER, J. W. 2013. Medial premotor cortex shows a reduction in inhibitory markers and mediates recovery in a mouse model of focal stroke. *Stroke,* 44**,** 483-9.

ZERBI, V., FLORIOU-SERVOU, A., MARKICEVIC, M., VERMEIREN, Y., STURMAN, O., PRIVITERA, M., VON ZIEGLER, L., FERRARI, K. D., WEBER, B., DE DEYN, P. P., WENDEROTH, N. & BOHACEK, J. 2019. Rapid Reconfiguration of the Functional Connectome after Chemogenetic Locus Coeruleus Activation. *Neuron,* 103**,** 702-718 e5.

ZHANG, N., RANE, P., HUANG, W., LIANG, Z., KENNEDY, D., FRAZIER, J. A. & KING, J. 2010. Mapping resting-state brain networks in conscious animals. *J Neurosci Methods,* 189**,** 186-96.

ZHANG, Z., ZHONG, P., HU, F., BARGER, Z., REN, Y., DING, X., LI, S., WEBER, F., CHUNG, S., PALMITER, R. D. & DAN, Y. 2019. An Excitatory Circuit in the Perioculomotor Midbrain for Non-REM Sleep Control. *Cell,* 177**,** 1293-1307 e16.

ZIV, Y., BURNS, L. D., COCKER, E. D., HAMEL, E. O., GHOSH, K. K., KITCH, L. J., EL GAMAL, A. & SCHNITZER, M. J. 2013. Long-term dynamics of CA1 hippocampal place codes. *Nat Neurosci,* 16**,** 264-6.

ZUCCA, S., D'URSO, G., PASQUALE, V., VECCHIA, D., PICA, G., BOVETTI, S., MORETTI, C., VARANI, S., MOLANO-MAZON, M., CHIAPPALONE, M., PANZERI, S. & FELLIN, T. 2017. An inhibitory gate for state transition in cortex. *Elife,* 6**,** 1-31.